The Life Cycle of Stars: Supernovae in Starbursts

by

Jason Kezwer
B.Sc., Queen's University, 2011

A Thesis Submitted in Partial Fulfillment of the
Requirements for the Degree of

MASTER OF SCIENCE

in the Department of Physics and Astronomy

The Life Cycle of Stars: Supernovae in Starbursts

by

Jason Kezwer
B.Sc., Queen's University, 2011

Supervisory Committee

Dr. Chris Pritchet, Supervisor
(Department of Physics and Astronomy)

Dr. Jon Willis, Departmental Member
(Department of Physics and Astronomy)

Dr. Karun Thanjavur, Departmental Member
(Department of Physics and Astronomy)

Supervisory Committee

Dr. Chris Pritchet, Supervisor
(Department of Physics and Astronomy)

Dr. Jon Willis, Departmental Member
(Department of Physics and Astronomy)

Dr. Karun Thanjavur, Departmental Member
(Department of Physics and Astronomy)

ABSTRACT

We have observed the nearest ultraluminous infrared galaxy Arp 220 with a 13 month near-infrared observing program using the Canada France Hawaii Telescope to search for obscured supernovae in this extreme star forming environment. This monitoring program was aimed as a feasibility study to determine the practicality of a large scale near-IR LIRG/ULIRG imaging survey. Establishing the supernova rate in these dusty galaxies is an important step toward confirming theorized star formation rates and settling the debate between the dominant energy source in LIRGs: star formation or AGN activity. Both the deduced high star formation rate and far-IR luminosity of Arp 220 suggest an atypically high supernova rate of 1-4 per year, two orders of magnitude greater than that of the Milky Way. We attempt the first direct observation of this rate which to date has been probed primarily through radio measurements of supernovae and remnants.

Through a point-spread function matching and image subtraction procedure we find no supernovae outside the galactic nucleus, consistent with the paradigm of a strong nuclear-contained starburst. Image subtraction residuals prevent the discovery of supernovae in the central regions of the galaxy. Using differential photometry we find evidence for a statistically significant brightening in the Arp 220 nucleus with a K-band peak of approximately $\Delta m_K = 0.16$ magnitudes. To find the true

peak magnitude we use Hubble Space Telescope archival data to subtract off the nuclear background and find an absolute magnitude of $M_K = -22.19 \pm 0.16$ (non-absorbed). This exceeds the luminosity of a typical core collapse supernova by roughly 3.5 magnitudes; rather, the observed variations in nuclear brightness are most likely the signature of an active galactic nucleus embedded in the dusty nuclei of Arp 220 or the superposition of light from several supernovae. This method is not sensitive to the detection of individual supernovae and we cannot rule out the occurrence of any nuclear SNe during the observing period.

The brightening event is dimmer in the H and J bands, appearing to be affected by extinction. Interpreting this as a supernova-related event we estimate the extinction in the nuclear regions of Arp 220 to lie between $2.01 \leq A_K \leq 3.40$ or $17.95 \leq A_V \leq 30.36$ in the optical, in agreement with several other estimates. Improved resolution is required in order to detect supernovae in the extremely bright nuclear environments of LIRGs. Alternatively, infrared spectroscopy would reveal the telltale spectral features of nuclear supernovae. Spectroscopic observations of the Arp 220 nuclei were conducted using Keck in July 2013 for this very purpose; results are pending.

We also explore the hypothesis that type Ia supernovae are produced primarily from young stellar populations. We model elliptical galaxies as two component stellar systems using PEGASE stellar templates: a fixed older underlying population coupled with a younger, less massive population. Varying the age and mass ratio of the young component, we examine its effect on I) the colours and II) the supernova rate of the single underlying population. We explore the effect with redshift and employ both theoretical and observational forms of the type Ia delay-time distribution. We then apply our models to the MENeaCS supernova survey and find that the number and distribution of red sequence SN Ia hosts agrees with theoretical expectations. The lack of evidence for a type Ia rate cutoff argues for a continuous delay-time distribution in support of the double degenerate model as the primary SN Ia progenitor channel. We conclude that it is not possible for all type Ia events in ellipticals to originate from a young frosting of stars.

Contents

List of Tables

List of Figures

ACKNOWLEDGEMENTS

I would like to thank:

Chris Pritchet, for valuable guidance, mentoring, support, and patience. You have taught me to approach problems from multiple perspectives and ultimately how to be a better scientist.

Karun Thanjavur, for assistance and providing data. Your support throughout my degree has been invaluable.

Chris Bildfell, for providing catalogs and helpful advice.

Jon Willis, for serving on my committee.

David Drutz, for insightful conversations and an excellent suggestion for a section title.

My Parents, for your unwavering support throughout the years.

Mother Nature, for teaching me what is truly important in life.

We ourselves are made of stardust.
Carl Sagan

To Robin, Raymond, Trevor and Vanessa.

Chapter 1

Introduction

1.1 Supernovae in the Universe

Stars are the nuclear reactors of nature. Through their main sequence lifetimes and beyond, these massive luminous spheres of plasma fuse lighter elements into heavier species, from hydrogen to iron for the most massive of stars. The end-result is a supergiant analogous to a stellar onion containing a mass gradient of elements in layers throughout the star (see figure 1.1). Once an iron core is established, further

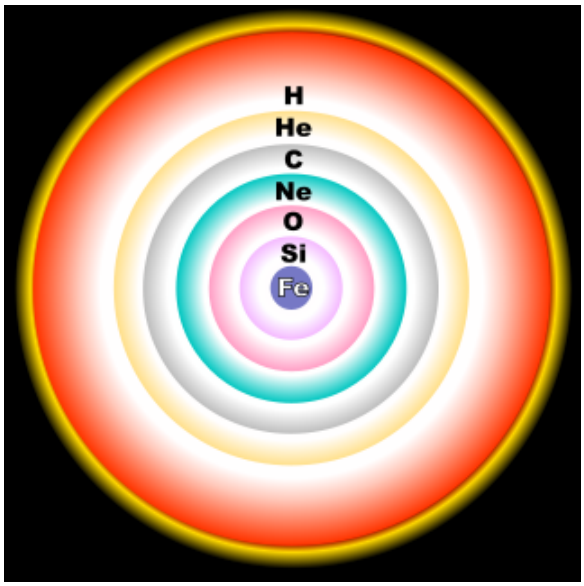

Figure 1.1: *The elemental layers of a massive evolved star ($M > 8M_{\odot}$). Core collapse can result once an iron core is established. (From Wikipedia.)*

nucleosynthesis becomes endothermic and is no longer spontaneously favoured. When the core reaches the Chandrasekhar mass ($M \sim 1.4 M_{\odot}$), it becomes incapable of supporting its own weight. With no further nuclear reactions available to counterbalance the immense gravity of the star and maintain hydrostatic equilibrium, core collapse commences followed by a massive explosion known as a supernova (SN) that releases on the order of 10^{53} ergs of energy, mostly in the form of neutrinos and kinetic energy. Supernovae spread the stellar elements fused over several million years into the interstellar medium, enriching it and setting the stage for a new generation of stars to be born. Nearly all nuclei in the Universe heavier than helium owe their origin to stellar nucleosynthesis, and more specifically are fused in supernovae.

While the cause of core collapse differs depending on the mass of the progenitor star, the physics of the post-collapse mechanism is well understood. As collapse commences, the inner core is compressed into a proto-neutron star roughly 30 km in radius with a density comparable to that of an atomic nucleus (Woosley & Janka, 2005). As the density reaches almost twice that of a typical nucleus, the nuclear force becomes so strong it halts the inner core collapse. The outer core continues to collapse, however, and "bounces" off the neutron-rich inner core resulting in a shock front now propagating outwards. The shock wave begins to stall from photodisintegration, but at the same time, roughly 10% of the stellar rest mass is radiated away in the form of a massive neutrino burst, which revitalizes the shockwave. The neutrino burst is actually the main output of the collapse event.

Core collapse supernovae may be subdivided into three classes: type II, type Ib and type Ic. We defer the discussion of type Ia supernovae for later in this thesis (see chapter 5). Supernova classification is determined based on the spectrum and light curve (brightness as a function of time). If hydrogen is found in the spectrum, it is classified as a type II SN; these stars still retain their hydrogen envelope before explosion. Spectra that do not display any hydrogen characteristics are then relegated to type Ib or Ic. These progenitors, which are typically more massive than type II progenitors, have lost most of their hydrogen envelopes from stellar winds or possibly through interactions with a companion. If the He I line is apparent in the spectrum the supernova is classified as type Ib, whereas a weak or non-existent He feature labels the SN as type Ic.

Observationally, supernova light curves display a brief rise time (on the order of a few weeks) as the shockwave begins to expand, reach peak luminosity, and then decay over a much longer time period (on the order of months). Type II light curves show

a slower decline (between 100-150 days from peak to 10% luminosity) than those of type I events (40-100 days) (Li et al., 2011). The latter light curves are driven by the radioactive decay of nickel-56 to cobalt-56 and finally iron-56 which excites the surrounding material causing it to glow. The visual light output of type II events is instead dominated by kinetic energy for the first several months and then radioactive decay afterwards.

While core collapse supernovae have been extensively studied in the optical, their infrared properties are less well known. Although much can be gleaned from optical bands, certain stellar environments (i.e. starburst galaxies) are shrouded with such large amounts of dust that supernova discovery is nearly impossible in the visible. So-called "extinguished" supernovae are much more readily detectable in the infrared. The first supernova detected in the near-infrared to receive spectroscopic confirmation was found just over a decade ago in 2001 (Maiolino et al., 2001). The peak absolute brightness of core collapse supernovae in the near-infrared according to Matilla & Meikle (2001) based on a sample of 13 supernovae is given in table 1.1 for a variety of filters.

SN Type	J	H	K	L
regular	-18.4	-18.6	-18.6	-19.0
slow-declining	-19.9	-20.0	-20.0	-20.4

Table 1.1: *Average core collapse supernova absolute peak magnitudes from Matilla & Meikle (2001). From the total sample of 13 near-IR SNe light curves, 11 were classified as regular and 2 as slow-decliners. Given the small sample size there is considerable scatter between supernovae; typically a spread of about 3 magnitudes at peak brightness (Mannucci et al., 2003).*

1.2 Luminous and Ultraluminous Infrared Galaxies

Luminous infrared galaxies (LIRGs) are those galaxies characterized by extremely large luminosities in the far-infrared ($L_{FIR} > 10^{11} L_{\odot}$) where the far-infrared is typically defined to span the wavelength range $8 - 1000$ μm. In the local universe out to a redshift of approximately $z \sim 0.3$, LIRGs are the dominant population of objects with bolometric luminosities exceeding $10^{11} L_{\odot}$ (Sanders & Mirabel, 1996). Ultraluminous

infrared galaxies (ULIRGs) are a subset of LIRGs that exhibit infrared luminosities $L_{FIR} > 10^{12} L_{\odot}$. The ULIRG luminosity cutoff is not physically motivated but merely serves as a handy value to adopt. ULIRGs represent an important stage in galaxy evolution. Primarily late-stage major mergers that emit extremely strongly in the infrared, it is thought these interactions result in elliptical galaxies. The progenitors, often gas rich spirals, funnel significant amounts of gas into the merger nucleus fueling massive starbursts. Consequently ULIRGs are extremely dust obscured, hiding much of their inner activity from the eyes of optical telescopes. The enshrouding dust absorbs light from hot young stars and re-emits in the infrared, explaining the characteristically high IR luminosities of LIRGs. It is also believed that AGN activity may play a role in LIRG emission. Due to the high amounts of dust obscuration, it has proven difficult to distinguish between the relative contribution of each of these two potential sources of infrared radiation, though it is believed starburst activity accounts for most of the energetics in LIRGs. For comprehensive reviews on the subject of LIRGs and ULIRGs see Sanders & Mirabel (1996) and Lonsdale et al. (2006).

1.2.1 The Fate of ULIRGs

ULIRGs are thought to be a vital stage of galaxy evolution bridging the phases of merging spirals and full fledged ellipticals. The typically massive star formation rate (SFR) in ULIRGs, high central stellar densities and kinematics imply these galaxies will ultimately land on the fundamental plane as intermediate-mass early-type galaxies (Kormendy & Sanders, 1992; Doyon et al., 1994; Genzel et al., 2001). Developing a greater understanding of these morphologically disturbed, higher redshift starbursting galaxies will lend insight into our understanding of local elliptical galaxies.

1.2.2 Supernovae in LIRGs

LIRGs represent superb laboratories in which to study supernovae. Their characteristically large infrared luminosities, if due primarily to starburst activity, imply greatly enhanced star formation rates (when compared to quiescent galaxies). For a given initial mass function (IMF), a large SFR implies the birth of a greater number of massive core collapse progenitors ($M > 8 M_{\odot}$). Further, significant star formation can only be maintained for so long; the starbursts in LIRGs must be young and continuously producing core collapse SNe. Therefore we expect an enhancement in the supernova rate (SNR) in accordance with the enhancement in SFR.

While there is still an active debate as to whether the IMF is universal or has an environmental dependence, there is evidence suggesting the IMF in starbursts appears to differ from that in less extreme environments. A variety of methods exist for determining the shape of the IMF; among them are measurements of far-IR flux which traces massive stars (Devereux & Young, 1990) and inferring the shape of the IMF through the supernova rate (e.g. Dabringhausen et al., 2012). It is found that the IMF may be top-heavy, biased towards more massive stars in starbursting galaxies such as Arp 220 (Dabringhausen et al., 2012) and Arp 299 (Anderson et al., 2011) as well as in high-redshift starbursts (Loewenstein, 2006; van Dokkum, 2008). The greater number of high mass stars implies a higher occurrence of supernovae in heavily star forming systems relative to quiescent galaxies; another reason to search for SNe in LIRGs.

Why are we interested in detecting supernovae in LIRGs? First and foremost, a direct measurement of the SNR in a LIRG would allow for an estimate of the star-formation rate (coupled with the IMF) and confirm the existence of what have been - until present - only hypothesized massive starbursts in such galaxies. Second, the detection of any type Ia SNe would allow for limits to be placed on the age of the starburst. Third, the extinction toward a SN can be found given measurements in multiple filters, lending insight into the severity of dust obscuration. Fourth, based on the numbers of each subset of core collapse object (e.g. type II's and Ib/Ic's), it is possible to place constraints on the form of the high mass IMF in these starbursts.

The theorized large SNRs in LIRGs have yet to be directly observed. A variety of methods have been employed to indirectly measure this rate, with varying success. In the next section we discuss this puzzle and the various methods that have been used in its study.

1.3 The Case of the Missing Supernovae

Optical surveys aimed at direct SN detection have found no enhancement in supernova rate between quiescent and starburst galaxies (e.g. Richmond et al., 1998). This result is surprising; starburst galaxies, with significantly higher star formation rates (as inferred from their FIR luminosity) when compared to quiescent galaxies, should display rates at least an order of magnitude higher than the latter (for instance see equation (1.2) for the proportionality between SNR and SFR). A potential explanation for the lack of SNe found in LIRGs is that such galaxies are more heavily

plagued by dust extinction, completely obscuring SNe in the optical. A solution is to instead observe in the near-infrared where extinction is significantly lessened. Dust grains have a characteristic size of approximately 0.1 microns; dust will therefore more easily scatter optical photons which have wavelengths nearer this size, resulting in greater extinctions in the optical region of the spectrum. The effect is modelled via Mie scattering and is described in (Irwin, 2008).

A variety of K-band ($\sim 2.2\mu$m) monitoring surveys aimed at directly detecting SNe in the near-IR have been attempted (e.g. van Buren et al., 1994; Grossan et al., 1999; Maiolino et al., 2002) with limiting success. Mannucci et al. (2003) monitored 46 LIRGs using three different telescopes (the Telescopio Nazionale Galileo, European Southern Observatory New Technology Telescope and Kuiper/Steward 61" infrared telescope) and discovered 4 supernovae, one of which (SN2001db) was the first SN discovered in the IR to have spectroscopic confirmation. Reported in Maiolino et al. (2002), based on the relation between B-luminosity and SNR (see equation (1.3)), this study observed a supernova rate an order of magnitude greater than rates estimated by optical surveys. Even so, using relation (2.1) Maiolino et al. (2002) find that their survey only detected roughly one fifth the number of expected supernovae.

Thus not only is there a discrepancy between SNe detected in optical versus infrared searches, but the SNR from the latter still falls short of the expected mark. Such a large SNR is not only expected on theoretical grounds, but also empirically based on radio observations of supernovae and supernova remnants (see subsections 1.3.2 and 1.4.2).

1.3.1 Estimates from star formation rates

Besides directly detecting supernovae there exist a wide range of observational methods with which to indirectly estimate the supernova rate in ULIRGs. Among these are surveys of supernova remnants using radio interferometry, measurements of non-thermal radio luminosities, and spectroscopic measurements of, for instance, near-IR [FeII] or [NiII] luminosity.

Knowledge of the degree of star formation can be used to estimate the frequency of core collapse supernovae. Once the star formation rate is known, with a given

initial mass function, it is possible to estimate the rate of core collapse events via

$$SNR_{cc} = \frac{\int_{m_l}^{m_u} \phi(M)dM}{\int_{m_{min}}^{m_{max}} M\phi(M)dM} \times SFR \tag{1.1}$$

where m_{min} and m_{max} are the minimum and maximum mass of stars formed in the starburst, and m_l and m_u are the lower and upper mass bounds on core collapse SN progenitors (Madau et al., 1998). The denominator represents the total mass formed in the starburst whereas the numerator gives the number of type II progenitors formed in the burst. Multiplying the above ratio by the star formation rate thus gives a measure of how many supernova progenitors are born (and are therefore expected to die) each year. This assumes the age of the burst is such that massive stars have had time to evolve to the supernova stage. This typically takes only a few Myr; see for instance the simulated supernova response curve from Svensmark (2012) (figure 1.2). Supernovae commence after only 3 Myr and for a continuous starburst would continue far past 40 Myr.

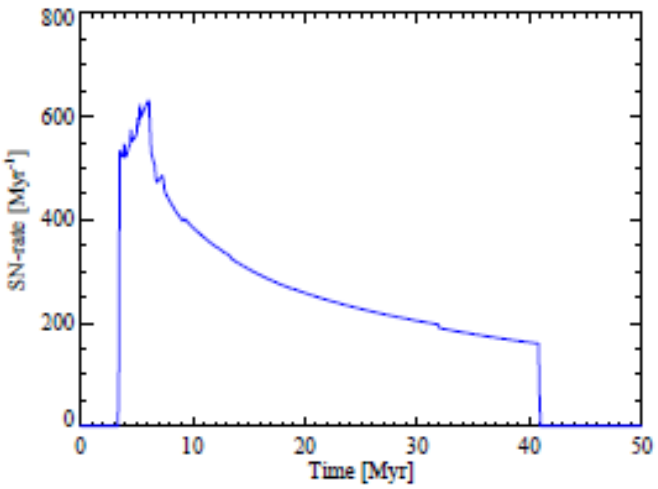

Figure 1.2: *Simulated supernova response function from an initial starburst of mass* $10^6 M_\odot$ *occurring at* $t = 0$ *(Svensmark, 2012).*

Consider the remaining unknown quantities in equation (1.1). The SFR (in $M_\odot$/yr) can be estimated by, for example, a measurement of the $H\alpha$ line strength. Hot, young stars often reside in partially ionized HII regions, and as electrons recom-

bine with Hydrogen nuclei, they cascade down energy levels. The resultant dominant emission line in the optical is the $n = 3$ to $n = 2$ transition, namely H-alpha, representing an effective spectral tracer of star formation.

Using a Salpeter IMF of the form $\phi(M) = CM^{-2.35}$ in which C is a constant and M the stellar mass, assuming the full range of possible stellar masses form in the starburst (0.1 to 125 $M_{\odot}$) and assuming progenitor masses spanning 8 to 50 $M_{\odot}$ (Tsujimoto et al., 1997), relation (1.1) works out to

$$SNR_{cc} = 0.0070\ M_{\odot}^{-1} \times SFR \quad 1/yr. \tag{1.2}$$

The above value corresponds to one SN for approximately every 140 $M_{\odot}$ of star formation (per year). Due to the range in SFR values found in ULIRGs via different observational signatures, the uncertainty in the IMF, and questions about the upper mass of a core collapse progenitor, the above is subject to significant uncertainty. The high rate of type II SNe indirectly observed in the galaxy Arp 220, for instance, suggests a top-heavy IMF in ULIRGs (Dabringhausen et al., 2012) which would elevate the estimate from (1.2) due to the presence of a greater number of type II progenitors when compared to a Salpeter IMF.

The blue luminosity (L_B) of galaxies has been used empirically to trace supernova activity; Cappellaro et al. (1999) find

$$SNR \simeq 10^{-12} \times \frac{L_B}{L_{\odot}} \quad 1/yr. \tag{1.3}$$

It has also been shown that the supernova rate can be linked to the far infrared luminosity (Matilla & Meikle, 2001; Mannucci et al., 2003). Combining the relations given in both of the above studies allows for an estimation of the core collapse SN rate via

$$SNR = (2.4 - 2.7) \times 10^{-12} \times \frac{L_{FIR}}{L_{\odot}} \quad 1/yr. \tag{1.4}$$

Note that since typical starburst ages (10-100 Myr) are comparable with the lifetimes of core-collapse SN progenitors (5-50 Myr), relations of type (2.1) are dependent on the age of the burst and will thus differ from galaxy to galaxy (Genzel et al., 1998). For instance a younger starburst ($\sim$ few Myr) will exhibit a lower rate since many SN progenitors have not had enough time to evolve. In similar fashion an older starburst ($\sim$ several 10s of Myr) will also display a lower SN rate since all SN precursors have already gone supernova.

Both the deduced high star formation rate and far-IR luminosity of LIRGs suggest an atypically high supernova rate in such galaxies. Upper estimates on the SFR in higher redshift ULIRGs reach as high as 1000 $M_{\odot}$/yr (Farrah et al., 2002), thus allowing for a potential SN rate of 7/yr. Estimates for the Galactic supernova rate sit at close to $SNR_{cc} \sim 1/100$yr (Diehl et al., 2006). Considering the star formation rate of our Galaxy (roughly 1 $M_{\odot}$/yr; see Robitaille & Whitney, 2010), this rate is consistent with relation (1.2). One can therefore expect ULIRGs to exhibit a supernova rate two orders of magnitude greater than the Milky Way. Such a high frequency of core collapse events should be readily detectable, however to date this rate has not been directly observed. The best estimates have been derived from surveys of supernova remnants via radio interferometry.

1.3.2 Radio interferometry

Supernovae, with their extremely high expansion velocities (thousands of kilometres per second), drive synchrotron radiation as the optically thick expanding SN shell encounters the dense circumstellar medium which was created by stellar winds from the red giant progenitor (Chevalier, 1982). The forward shock of a supernova remnant continues to expand and accelerate electrons to relativistic velocities, emitting synchrotron radiation which exhibits a power-law decay. The synchrotron mechanism is detectable in the radio regime, thereby providing an excellent wavelength range in which to observe both supernovae and remnants. Due to the excellent milli-arcsecond angular resolutions attainable through radio interferometry, this technique provides an accurate method for probing the nuclei of ULIRGs, where it is thought the majority of supernovae occur. Counting and estimating the age of remnants gives an alternative method to indirectly determine the supernova rate in starburst galaxies (see subsection 1.4.2).

Indirect supernova search methods have hinted that the SNR in LIRGs is significantly higher than rates measured optically. However even direct IR searches have resulted in disappointing results. Where are all of the supernovae in these massive starbursts? In attempt to answer this question we turn to one galaxy in particular.

1.4 Arp 220: 400 Quintillion Leagues Over the Sea

At a distance of 77 Mpc ($z = 0.018$), Arp 220 is the closest ULIRG to Earth and has been extensively studied. Often touted as the prototypical ULIRG with luminosity $\log(L_{FIR}) = 12.12$ (Cresci et al., 2007), Arp 220 is a late-stage merger between a pair of gas-rich galaxies (Norris, 1988) containing beautiful tidal trails clearly visible in the optical. Figure 1.3 shows Arp 220 as captured by the Hubble Space Telescope (HST). Note the extensive dust lane intersecting the centre of the galaxy, completely obscuring the nuclear regions.

The picture becomes substantially more clear when probing longer wavelengths capable of penetrating the dust. Figure 1.4 shows Arp 220 observed in the near-infrared by the HST NICMOS instrument. The nuclear structure of the galaxy becomes readily apparent, revealing two distinct nuclei: the crescent shaped western nucleus and the smaller circular eastern nucleus. Radio interferometry has revealed the two central nuclei to be separated by $0.98''$ (366pc) (Scoville et al., 1998). In addition, large star clusters (possibly ultra-compact dwarf galaxies) permeate the galaxy, visible as bright stellar point sources (Scoville et al., 1998; Wilson et al., 2006; Dabringhausen et al., 2012). At the distance of Arp 220 one second of arc subtends 373 parsecs; see the appendix (A.1) for more detail.

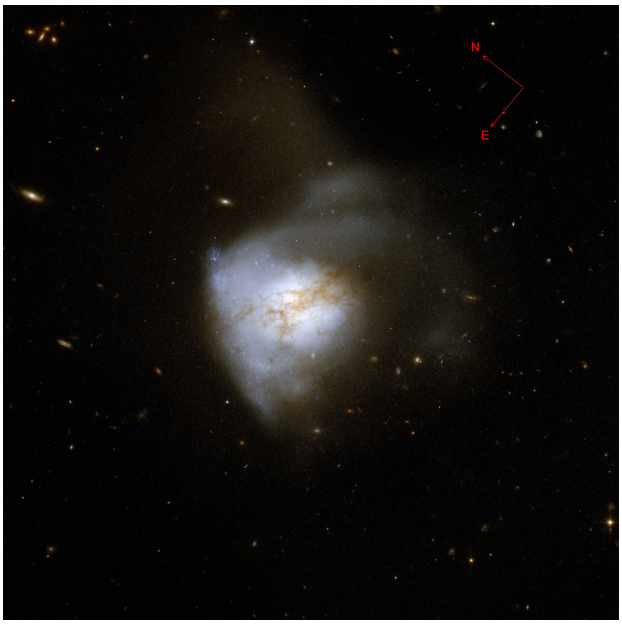

Figure 1.3: *Arp 220 in the optical (B & I filters) captured by the Hubble Space Telescope's Advanced Camera for Surveys. The field of view is approximately 169 square arcsec. North and east are marked on the image. (Image from NASA/ESA.)*

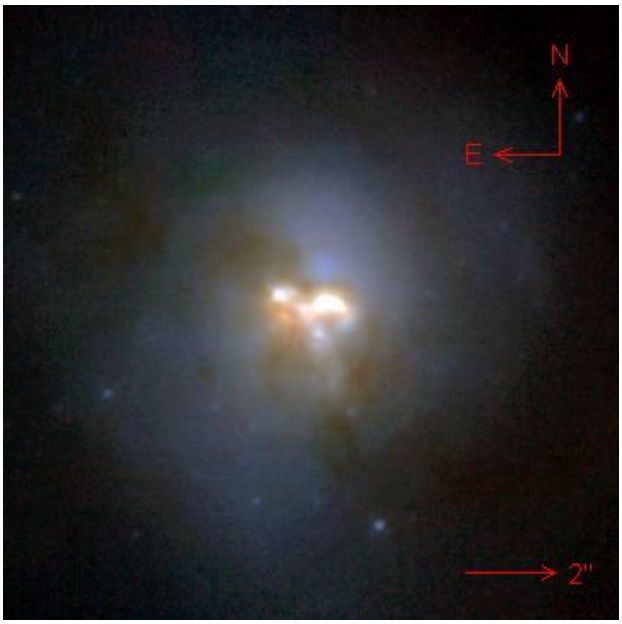

Figure 1.4: *Arp 220 in the near-IR as seen by NICMOS on HST Scoville et al. (1998). North and east are denoted on the image; the field of view is 19 square arcsec.*

1.4.1 Potential AGN/black holes

There is a growing body of evidence for the existence of a supermassive black hole residing in the west nucleus of Arp 220. Measurements from the Chandra X-Ray Telescope have found a strong x-ray point source with a 2-10 keV luminosity that is roughly 10^{-5} times the far-infrared luminosity, along with extended x-ray emission which raises the total nuclear x-ray luminosity by an order of magnitude (Clements et al., 2002). While the x-ray point source can also be explained by frequent radio supernovae exploding in a dense central environment, a powerful AGN hidden behind high H_2 column densities cannot be ruled out. Further, XMM-Newton data found iron $K\alpha$ emission at 6.7 keV with a large equivalent width, a potential indicator to the presence of a hidden AGN (Iwasawa et al., 2005). Several OH masers are found in Arp 220; one in particular shows a high velocity gradient, possibly due to a low-mass ($\sim 1.7 \times 10^7 M_\odot$) AGN (Rovilos et al., 2003).

Downes & Eckart (2007) observed the CO(2-1) and CO(1-0) lines along with the millimeter continuum of the western nucleus of Arp 220 with the IRAM Plateau de Bure interferometer. Analyzing the dust features of the west molecular disk, they fit a brightness temperature to the dust continuum of 90 K - significantly hotter compared to millimeter-detected dust in other starburst galaxies. Based on the size of the W dust source (35 pc $\times$ 20 pc), a gas density of 5000 $M_\odot/\mathrm{pc}^3$ is estimated, roughly 10 times the stellar density in cores of giant ellipticals. Further, a CO-torus which is centered on the 1.3 mm compact dust source shows a steep velocity gradient toward the nucleus, more typical of a black hole. For a starburst to be responsible for this dust source requires 30 times the luminosity of M82 confined to a volume a thousand times smaller, which has never been observed. For these reasons Downes & Eckart (2007) argue a black hole accretion disk must be the culprit explaining the luminosity of Arp 220's western nucleus. If this is the case, why have spectra of Arp 220 not revealed any major signs of an AGN? Downes & Eckart (2007) find extreme optical foreground extinctions of $A_V > 100$, explaining why Arp 220 has a cooler SED than is expected from AGN-powered ULIRGs such as Mrk 231 and nearby quasars.

There is also evidence suggesting smaller accreting black holes may reside inside Arp 220. In a radio survey of Arp 220, Batejat et al. (2012) found three rapidly varying sources in the western nucleus showing changes in shape, position and flux density over periods of less than four months in duration. While supernova remnant variability and/or rapid evolution of multiple SNe are contenders for the source of

these varying objects, an intriguing possibility is that they are microblazars: accreting stellar mass ($\sim 10M_{\odot}$) black holes that are beamed towards Earth.

Not all x-ray studies of Arp 220 support the presence of an AGN. Through another Chandra study of the eight closest ($z \leq 0.04$) ULIRGs - three of which are (spectroscopically) classified as harbouring an AGN - Ptak et al. (2003) find no evidence to support an AGN in the remaining five including Arp 220. They conclude there is no evidence to suggest buried AGN power most ULIRGs. Nevertheless, even if an AGN is present in Arp 220, a significant starburst ($L \sim 10^{11}L_{\odot}$) is still required to explain the infrared luminosity and radio supernovae (Iwasawa et al., 2005). Therefore, regardless of the presence of an AGN the starburst is the more important contributor to the overall energetics of the galaxy.

1.4.2 Supernovae in Arp 220

Based on the sheer magnitude of star formation deduced in Arp 220, and the fact that it is a major gas-rich merger, we anticipate quite a large supernova rate. We can estimate the SNR indirectly using relation 1.2 and measurements of the SFR in Arp 220 - which range from 100 to 400 $M_{\odot}$/yr (Lonsdale et al., 2006) - giving a range of $SNR_{cc} \simeq 1 - 3$ per year. Alternatively, using the FIR luminosity of Arp 220 ($L_{FIR} = 1.4 \times 10^{12}L_{\odot}$) together with (2.1) yields approximately 3.5 expected supernovae per year.

To date the only successful method for the discovery of supernovae in Arp 220 has been via radio observations. A large number of compact sources have recently been discovered from radio surveys of the nuclei of Arp 220. The favoured interpretation is that these radio sources constitute a mix of both radio supernovae and supernova remnants (Parra et al., 2007).

Very Long Baseline Interferometry (VLBI) observations of the nuclei of Arp 220 were taken at 18 cm by Smith et al. (1998). They found 12 unresolved compact sources in the western nucleus and 2 in the eastern, and attributing them to luminous radio supernovae, calculate a luminous SN rate of $SNR_{lum} = 1.75 - 3.5$ /yr. Note the agreement with our indirect rate estimates. Following this interpretation, the high density of supernovae concentrated in the nuclei presents the expected structure of a compact starburst; however AGN activity was not ruled out as a contributing factor to the radio emission.

Further VLBI observations at the same wavelength were conducted years later

with improved sensitivity (Lonsdale et al., 2006). In total 49 point sources were discovered, 29 in the west nucleus and 20 in the east. The sources were highly clustered; 22 in the western nucleus are found within a $0.25'' \times 0.15''$ (296 pc $\times$ 185 pc) region and 14 in the eastern nucleus within a $0.3'' \times 0.2''$ (370 $\times$ 259 pc) area. We will see in chapter 2 these regions span less than one square pixel in our observations. Sources located outside of these regions were found to be less emissive. It is clear the physical locations of these sources support the notion of a highly compact starburst in this ULIRG. Four new sources (3 in the W, 1 in the E) were found through comparison with similar data taken a year prior. Following the interpretation of Smith et al. (1998) that these sources are radio supernovae implies a supernova rate of $SNR_{lum} = 4 \pm 2$ /yr. Note this is a lower limit since it is unclear whether supernovae would remain above the flux detection threshold within 12 months of exploding, whereas some may have simply been missed during the interval between observations. Based on the total number of sources, the inferred supernova rate and the large luminosity of the remnants ($\simeq$ 50 times brighter than the brightest Galactic remnants with known dates of explosion), they estimate remnant ages of no more than a few decades. Most of the objects are thus quite young. Comparing Arp 220 to the starburst galaxy M82, it is apparent that the starburst in Arp 220 is not only confined to a smaller volume but roughly 50 times more luminous, again similar to the spectroscopic findings of Downes & Eckart (2007).

Parra et al. (2007) detected 18 sources in the nuclei at 3.6, 6 and 13 cm. The spectra of over half these sources are consistent with type IIn supernovae, core collapse SNe that occur in environments with extremely dense circumstellar material shed by the progenitor prior to explosion. Type IIn SNe can be significantly brighter than their typical type II counterparts, suggesting that a large fraction of type II events in Arp 220 are extremely luminous. Such powerful SNe may be due to short, intense starbursts of up to $1000 M_{\odot}$/yr. Even more recently, Batejat et al. (2011) detected 17 sources in both nuclei in separate fields of view $0.410'' \times 0.205''$ (518 pc $\times$ 259 pc) in size, similarly concentrated together in much smaller regions. From the total sample, 7 were classified as radio SNe (6 of which resided in the W nucleus), 2 as transition objects between the SNe and SNR Sedov phase and 7 as supernova remnants. They estimate ages of three SNe at 6-7 years. Likewise the remnants are thought to have a minimum age of 12 years. Therefore these objects are also very young, in agreement with the findings of Lonsdale et al. (2006) and further supporting the notion of an active, powerful starburst in the nuclei of Arp 220.

Consider the composition of the stellar populations in Arp 220. Engel et al. (2011) use integral field spectroscopy of Arp 220 in the H and K bands at a resolution of 0.3 arcsec and find that within the central kpc of the galaxy, most of the K-band luminosity is derived from a 10 Myr old starburst. They also find evidence for a substantial $\simeq 1$ Gyr old population and a smaller contribution from stars with ages less than approximately 8 Myr. It is apparent most of the stellar populations in the core are young enough to be producing core collapse supernovae at the high frequency radio findings imply (see figure 1.2; the peak in SNR occurs just prior to 10 Myr).

The large number of both SNe and remnants found in the nuclear regions of Arp 220 likely trace the star formation in the galaxy. These observations lend weight to the hypothesis that Arp 220 exhibits a highly compact, centrally concentrated starburst within the inner kpc of the galaxy. If so, the majority of SNe are expected to be found in this region, an area completely obscured by dust in the optical and with a likely $2 - 3$ magnitudes of extinction in the K-band (Cresci et al., 2007). Further, the young ages of the objects implies current SN activity in the galaxy, making it an excellent candidate for direct SN detection.

1.5 Overview

The first part of this thesis focuses on a search for obscured supernovae in Arp 220. Chapter 2 describes the search philosophy and methodology including data acquisition and processing. We describe in detail a variety of data analysis techniques employed to locate SNe in the galaxy in chapter 3, and compute an estimate for the degree of nuclear extinction in Arp 220 in chapter 4. The second part of this thesis involves an exploration of type Ia supernovae in old, elliptical galaxies from young bursts of star formation. Chapter 5 describes the entire project including background, stellar population modelling and application to observations. Finally we state our conclusions in chapter 6.

Chapter 2

Data

In this chapter we introduce the data and instrument utilized in our Arp 220 supernova search. Section 2.1 describes the study justification and places it into the context of other similar modern searches. We give an overview of the data processing and image detrending procedures in section 2.2 and perform aperture photometry on WIRCam Arp 220 data in 2.3. Lastly we calculate two important parameters of our detector, the gain and read noise, in section 2.4.

2.1 ULIRG Monitoring Feasibility Study

As mentioned previously, the severe extinction, coupled with the potentially strong background of active galactic nuclei emission are a challenge to monitoring ULIRGs for supernovae in the optical. To peer through such large amounts of dust, one can turn to the infrared where extinction is significantly more modest ($A_K \sim 0.1A_V$) (Rieke & Lebofsky, 1985). The two main observing considerations for a large-scale supernova monitoring project are cadence and number of objects. A trade-off exists between the two such that increasing the frequency at which a given galaxy is observed decreases the total number of galaxies that can be observed (assuming fixed telescope time and integration time per object). To study a larger number of galaxies, the integration time per galaxy could be reduced, but again at the cost of detecting fainter supernovae. First and foremost, it must be determined whether observations in the near-infrared are capable of revealing supernovae.

As mentioned in the introduction, searches in the infrared have been previously undertaken, focusing on a large contingent of starburst galaxies at few epochs instead

of a single ULIRG at many epochs. A sample of 177 IRAS starburst galaxies closer than 25 Mpc was monitored in roughly monthly intervals between 1992 and 1994 in a search of extinguished (highly reddened) SNe using the Michigan Infrared Camera at the Wyoming Infrared Observatory (Grossan et al., 1999). They expected to detect 1-6 SNe/yr in their sample. Three non-extinguished SNe were observed following their optical discovery, yet not a single obscured SN was found.

As discussed previously, Mannucci et al. (2003) observed a sample of 46 IRAS galaxies chosen such that $L_{FIR} > 10^{11.1} L_{\odot}$ to maximize the SFR of their sample and by association the SNR (see relations (1.2) and (2.1)). The observations took place between 1999 and 2001 using a monthly cadence and the K' filter (similar to K but cut off above 2.3 μm) . They detected four supernovae, only two of which were not first discovered in the optical (and thus not highly obscured). Their calculated SN rate, however, is still discrepant by a factor of 3-10 from that expected based on the far-infrared luminosity of the galaxy sample (i.e. using equation (2.1)).

Taking advantage of a much higher resolution telescope, Cresci et al. (2007) observed a sample of 16 galaxies at a single epoch using the Near Infrared Camera and Multi-Object Spectrometer instrument (NICMOS) in SNAPSHOT mode on the Hubble Space Telescope. They then compared their acquired data with archival data of each galaxy from a prior epoch. Between 12 and 27 supernovae were expected from this study, yet zero were discovered. Of note was a supernova candidate detected 1.1 arcsec away from the west nucleus of Arp 220 which could not be confirmed via spectroscopic follow-up months later.

These earlier studies surveyed large numbers of galaxies - often LIRGs - looking at each in small windows of time. Our unique approach was to monitor a single heavily starbursting galaxy (a ULIRG) over an extended period of time. The enhanced star formation rate in a ULIRG coupled with the large duration of time spent observing a single target improves the chances of detecting SNe. The enhanced FIR luminosity of a ULIRG also raises the expected SNR relative to LIRGs by as much as an order of magnitude (see equation).

In order to test the feasibility of detecting infrared supernovae in a single galaxy with an extremely high SFR, a monitoring survey of Arp 220 was conducted using the Wide-field Infrared Camera (WIRCam) on the Canada-France-Hawaii Telescope (CFHT). The most well-studied and closest ULIRG to Earth, Arp 220 serves as an excellent candidate for the direct detection of supernovae. The aim of this observing project was twofold: to directly verify the large expected (and until present indirectly

determined) supernova rate in Arp 220, and to establish the feasibility of a large-scale ULIRG survey in the hopes of capturing obscured SNe in a variety of starburst galaxies and solving the missing SNe problem.

2.1.1 CFHT Wide-field Infrared Camera

The Canada-France-Hawaii Telescope currently employs three main instruments in rotation: MegaCam (a wide-field optical imager), ESPaDOnS (a spectropolarimeter) and WIRCam (an infrared imager; see Puget et al., 2004 for technical specifications). A single observing run for the telescope consists of one lunation in time during which at least two of CFHT's instruments are mounted in succession. When WIRCam is in operation, it is mounted at the prime focus of CFHT for approximately 10 consecutive days. It is composed of four detectors, each containing 2048 x 2048 pixels. Each detector chip is separated by a 45 arcsecond gap, providing for a total (chip + chip gap) field of view of 21.5 square arc minutes. One pixel covers 0.3 arc seconds of sky and each detector contains 32 amplifiers which are read out in parallel. Image generation differs from the process in optical charged-coupled devices (CCDs) mainly due to the lack of a shutter on the infrared imager. Instead of opening and closing a shutter to mark the start and end of an exposure, WIRCam uses correlated double sampling (CDS) in which an image is taken at the start of integration and end of the integration (referred to as REF and RAW images, respectively); the resultant science image is formed by taking the difference between the two (RAW-REF). This has certain advantages such as eliminating any bias which merely gets subtracted out when forming the CDS image. Data are delivered in the form of four-extension fits images, each extension corresponding to one of the four infrared chips. WIRCam contains four broadband filters (Y, J, H, Ks) and seven narrow band filters. The detector's wide field of view, coupled with the exceptional seeing on the summit of Mauna Kea (typically ~ 0.7 arcsec in the infrared in our observations) make WIRCam an excellent instrument with which to observe Arp 220.

2.1.2 Arp 220 observing strategy

Arp 220 was observed over the course of 13 months from July 2011 to August 2012 using an approximately bi-monthly cadence, specifically observing near the start and end of each WIRCam run. By spacing observations in time, the chances of observing a supernova at peak light are maximized. Observations were performed in the J, H

and Ks filters. Information on each utilized filter, including the exposure time per individual observation, is provided in table 2.1.

A quick note on the difference between the Ks filter (the s stands for "short") and the traditional Johnson K filter. The latter exhibits significant transmission out to 2.4 microns, however beyond 2.3 microns thermal contributions from the atmosphere tend to become significant. As such the Ks filter was envisioned to contain a cutoff at 2.3 microns and reduce thermal background noise otherwise present in the K filter. From hereon we refer to the Ks filter as K for simplicity.

Filter	$\lambda_o(\mu m)$	Bandwidth (μm)	t_{exp} (s)
J	1.252	0.158	55
H	1.631	0.289	14
Ks	2.146	0.325	23

Table 2.1: *WIRCam near-infrared filter specifications. The exposure time t_{exp} is per individual exposure; between 5-10 single exposures were taken at each epoch. The exposure time in each filter was chosen based on achieving a signal to noise of 10 for the faintest Arp 220 nuclear component (the SE nucleus).*

The celestial coordinates (J2000) of Arp 220 according to the NASA Extragalactic Database[1] are (RA,DEC)=(15:34:57.1,23:30:11.0). Consequently at the location of Mauna Kea Arp 220 is barely visible above the horizon between October and December, and reaches maximum visibility in mid-May. A total of eighteen epochs of data were obtained, with a gap between the months of October-December 2011. Table 2.2 presents a catalog of observations.

[1] http://ned.ipac.caltech.edu

Epoch	Date (month/day/yr)	Day
1	07/17/11	0
2	07/19/11	2
3	07/21/11	4
4	08/06/11	20
5	08/15/11	29
6	09/10/11	55
7	09/18/11	63
8	01/19/12	186
9	01/22/12	189
10	03/02/12	229
11	03/14/12	241
12	03/31/12	258
13	04/04/12	262
14	04/10/12	268
15	07/27/12	376
16	08/03/12	383
17	08/10/12	390
18	08/14/12	394

Table 2.2: *Catalog of WIRCam Arp 220 observations. Plots in the remainder of the thesis refer to dates of observation either by epoch or day. The first date was set as day 0.*

2.1.3 HST Near-Infrared Camera and Multi-Object Spectrometer

The Hubble Space Telescope, arguably the most successful space-based telescope to be deployed, has provided unprecedented views of the cosmos. Its infrared instrument, NICMOS, contains three adjacent independently operating cameras and is capable of performing imaging, polarimetry, coronagraphy and grism spectroscopy over a wavelength range of 0.8 to 2.5 microns (see Thompson, 1994). Not only is its resolution superior to many ground-based detectors (specifically those that do not use adaptive optics), but its position above the atmosphere significantly reduces background from the infrared sky (by a factor of $\gtrsim 10^3$). NICMOS was used to observe Arp 220 on

April 4, 1997 in three near-IR filters for a combined exposure time of 1023 s in each filter. NICMOS archival data is used in this thesis as a comparison to WIRCam data.

The NICMOS filters used to observe Arp 220 are similar to those on WIRCam in H and K, yet differ significantly in J. We show NICMOS filter transmission alongside those of WIRCam in table 2.3.

$Filter_W$	$\lambda_o(\mu m)$	$\Delta\lambda(\mu m)$	$Filter_N$	$\lambda_o(\mu m)$	$\Delta\lambda(\mu m)$
J	1.252	0.158	F110W	1.100	0.592
H	1.631	0.289	F160W	1.594	0.403
Ks	2.146	0.325	F222M	2.216	0.143

Table 2.3: *NICMOS and WIRCam filter specifications for those used to observe Arp 220. The filter subscript denotes the instrument (W for WIRCam, N for NICMOS). The letters appended to NICMOS filters refer to the filter width; M and W represent medium and wide bandwidths respectively.*

2.2 WIRCam data processing

An infrared detector operates in a similar fashion to an optical charge-coupled device (CCD). Photons incident on the detector liberate electrons (with a 1:1 correspondence). The resultant charge is collected, converted to a voltage, digitized and amplified for ease of registration. The input is photons, the output a value in analog-to-digital units (adu). Each pixel in a science image has an associated adu value representing the number of photons incident on the pixel (though not a direct 1:1 correspondence; see section 2.4.2).

A number of preliminary steps are performed on the data at CFHT before they are put through a main processing pipeline. By comparing the RAW and REF images to a reference saturation map, badly saturated pixels are flagged. Raw images are stored in 16-bit integers but must be converted to 32-bit floats in order to be processed and form the CDS image. In this step, any negative integers can be wrapped around into large positive float values. To prevent this from occurring a purely digital and noiseless chipbias of 7000 adu is added to all pixels. Each detector image contains a 4 pixel-wide border which is used as a reference to correct for drifts in the bias, and the border is then subtracted from each chip. In addition, crosstalk between pixels can create artifacts from the bright guide star which is used for telescope pointing. To

avoid any interference the guide star window is crossed out. Lastly, charge is stored on the chips in a capacitor-like device which behaves slightly differently depending on the amount of charge. As such a non-linearity correction is applied to each detector by modelling the effect with a polynomial function. Once the preliminary pre-processing is completed, the data are ready to be detrended.

2.2.1 Image detrending

Any detector will imprint onto data a significant amount of interference in a variety of forms due to both the detector itself and its internal electronics. Further, other parts of the telescope system may emit in the near-IR such as warm objects lying along the optical path (i.e. dust). The main purpose of image detrending is to remove as much of any additional signature (instrumental or otherwise) from the data as possible, leaving behind an image inherently representative of the observing target, free of detector footprints.

Even when not actively collecting data, any detector will emit photons due to internal heat; this is referred to as the dark current. The WIRCam cryostat is regulated at 80K to within a thousandth of a degree and as such the dark current is both very low ($< 0.05e^{-}$/s) and stable over time. The variation in dark current is thus linear with integration time but still present. To remove this extra signal a dark field is subtracted from the CDS image. Normally a CCD dark is obtained by taking an exposure with the shutter of the detector closed. Since WIRCam is shutterless, two filters are crossed together instead which imitates the same effect as a closed shutter since no light is able to penetrate. Dark fields are captured at the end of each observing night, and a master dark is constructed at the end of each WIRCam run by median combining all dark frames taken with the same exposure time as the science image; the master dark is then subtracted off the science image.

Second, pixel response across the detector is not constant but exhibits slight systematic variations. This is corrected by flat fielding: taking exposures of a uniform source and dividing the science frame by the flat frame. Since all pixels should theoretically have the same value when imaging a uniform "flat" source, any differences are due to nonuniformities in the pixels themselves and can be removed by dividing the science frame by the flat. WIRCam uses twilight flats, exposures taken of the sky at dusk or dawn. Flats are first dark subtracted and multiplied by the appropriate bad pixel mask, which identifies bad ("hot" or nonresponsive) pixels on each chip and

sets their adu value to 0 while keeping good pixels at a level of 1. Then 15 flats are median combined and normalized to produce the master flat field (a weight map). The science image is then divided by the master flat.

The last and often most complex step of image reduction consists of removing the effect of the sky. The infrared sky is very bright and varies in time, typically on timescales of 5-15 minutes; thus removing its influence is quite a challenge. In the near infrared (J, H and K bands) the dominant background source is airglow, created by light radiated from excited OH^- radicals (Glass, 1999). These molecules are present in the atmosphere at an altitude of 85-100km and thus affect all Earth-based observing sites including the summit of Mauna Kea. The variance in airglow is not only temporal, but also spatial (over scales of tens of kilometres) and varying in intensity (the amplitude of emission can change by up to 300%). Consequently there is no simple way to completely filter out airglow, but the best method for reducing its effect is via sky subtraction. This consists of taking several exposures of the sky in fields close to (both spatially and temporally) the science frame. WIRCam uses adjacent science exposures for this task. To form a master sky frame in one filter, all science exposures taken in close proximity to the exposure in question (within 15 arcsec in the sky and 20 minutes in time) are used. Each adjacent exposure is slightly dithered from the previous by between approximately 15 and 20 arcsec (large enough shifts to avoid the blending of bright stars and extended objects). After median combining neighbouring exposures and masking bright sources, a sky construct is formed which is an excellent approximation to the current sky in the field of interest. By scaling the sky construct up to the mean of the science image, the sky can then be subtracted off.

To summarize the image detrending procedure:

1. Take science, dark and flat exposures.

2. Create sky frame from adjacent science exposures.

3. Perform dark subtraction on flat, sky and science frames.

4. Divide the sky and science images by the master flat field.

5. Subtract the sky frame from the science frame.

All three of these vital detrending steps - dark subtraction, sky subtraction and flat fielding - are performed by a CFHT pipeline called $'I'iwi$ which works in Interactive Data Language (IDL). The result is a set of processed individual science exposures, which must then be co-added together.

2.2.2 Zero point determination

Another important calibration vital to accurate photometry is the determination of photometric zero points. The zero point is a magnitude offset which transforms the measured magnitude into a specific photometric system (the Vega system for WIRCam). Zero points are determined for each WIRCam run using references stars in the detector's wide field of view; by comparing instrumental photometry to standard measurements from the Two Micron All Sky Survey (2MASS), the zero points can be calibrated in each filter. 2MASS was a large survey of the infrared sky performed between 1997 and 2001; its catalogue contains 470 *million* sources that were surveyed using two 1.3 m telescopes. The WIRCam zero points were verified during the first Arp 220 data release using the same method with reference stars on the detector chip containing Arp 220.

2.2.3 Image alignment

Each epoch of Arp 220 observations produces between five and ten exposures in each of the J, H and K filters. In order to extract the most detail from the images, individual detrended exposures must be co-added or stacked together. As mentioned before, the telescope is slightly dithered between exposures. Consequently prior to stacking, images must be aligned to a common coordinate system. Stacking is completed at CFHT using the program *SExtractor* which identifies known stars in the field, matches them between exposures, and then stacks all four chips together simultaneously into one continuous mosaic image. Stacking was also performed externally by P. Hudelot at Terapix. A sample composite image (all three bands together) is shown in figure 2.1.

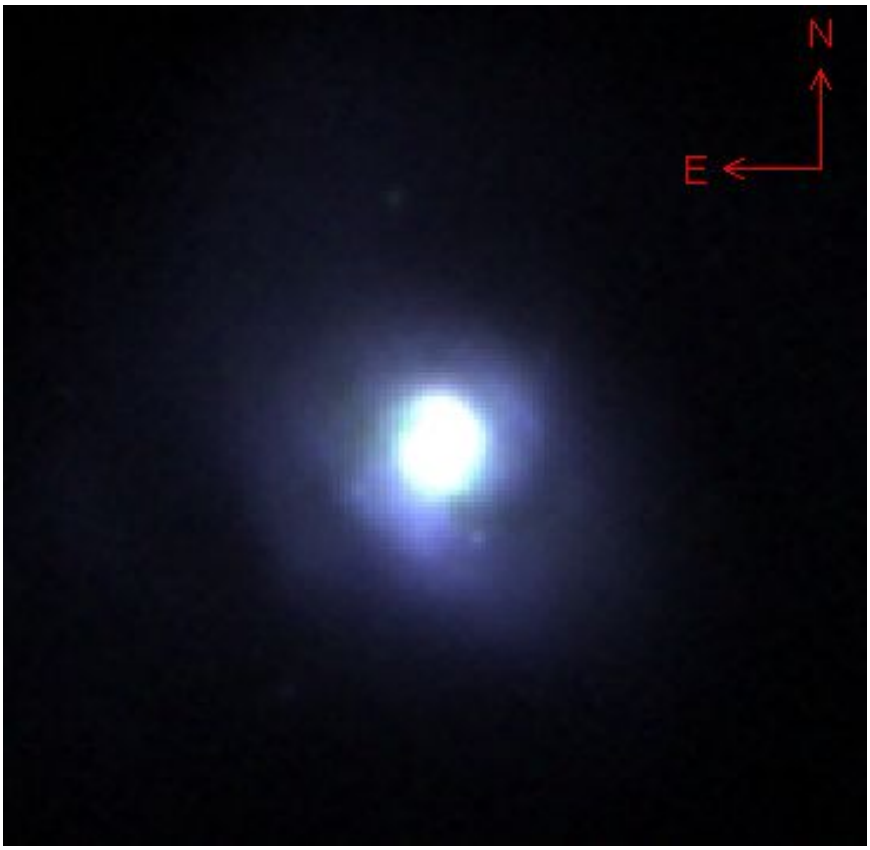

Figure 2.1: *Composite J, H and K WIRCam image from epoch 11. The field of view is approximately 48 arcsec × 48 arcsec. North is up and east is left in the image. Note the visibility of several prominent star clusters associated with the galaxy and disturbed morphology indicating merger activity.*

Mosaic images are not aligned between epochs, however; such alignment becomes necessary if images are to be compared across time. Our aim to search for SNe, by nature transient events, requires alignment between epochs. We achieve this via the *Groth* algorithm, a point-matching algorithm (Groth, 1986). Given two lists, the algorithm forms all possible triangles between the points in each list individually, and then attempts to match triangles between lists. The algorithm measures translation, rotation, magnification and inversion between lists.

The Groth algorithm, while ideal for the purpose of image alignment, has many potential applications beyond astronomy. A more Earth - or sea - bound usage puts the algorithm to use in tagging *Rhincodon typus*, otherwise known as the whale shark. Whale sharks are the largest fish in the world reaching up to 12 meters in length; each is characterized by a unique pattern of spots on the skin, akin to a fingerprint

(see figure 2.2). By treating the spots in an analogous manner to stars in a telescope image, researchers have adapted the Groth algorithm to identify individual whale sharks by matching the spot pattern between images (Arzoumanian et al., 2005). This allows the migratory patterns of specific whale sharks to be followed as they are photographed in completely different regions of ocean over long periods of time.

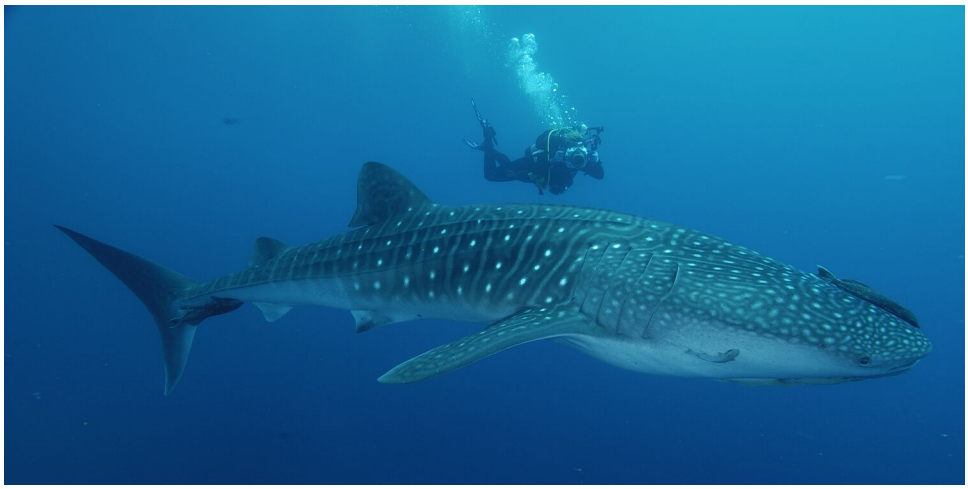

Figure 2.2: *A whale shark in the deeps. Note the distinctive spotted pattern on its body. Researchers use the Groth algorithm to identify and track individual whale sharks over time.*

Lists in the Groth algorithm can be sets of data points or images (as is the case with Arp 220 data), and the points used are therefore objects (stars) in the frame. The algorithm takes two images as input, one designated as the reference. It then outputs a coordinate transformation which will shift the image of interest into the same coordinate system as the reference. The image shifting is performed by another IRAF task, *scrosh* (developed by Chris Pritchet). Through the use of these two algorithms, stacks between epochs can be aligned to within an accuracy of 0.01 pixels. Since the plate scale (magnification) of WIRCam does not change between observing runs, and the amount of rotation is negligible, the *Groth* algorithm was run to correct solely for translation between stacks. Next we verify the effectiveness of the detrending procedure via photometry.

2.3 Aperture Photometry

2.3.1 Magnitude System

The brightness of an astronomical object is conventionally measured in magnitudes. Yet what we physically measure is a flux: an amount of energy per unit time per unit area. How do magnitudes relate to fluxes? The magnitude system is a relative scale, and typically employs Vega as a reference star. For an object with magnitude m and flux f, and a reference object with magnitude m_o and flux f_o, the following relation maps a difference in magnitudes to a ratio in flux:

$$m - m_o = -2.5 \log \left(\frac{f}{f_o} \right). \tag{2.1}$$

Note that measurements for each object must be in the same waveband to use the above equation. We can also rearrange relation (2.1) and put it into another useful form:

$$\frac{f}{f_o} = 10^{-\frac{2}{5}(m-m_o)}. \tag{2.2}$$

If given the magnitudes of two objects, the ratio of their fluxes can be determined and is related to the difference in magnitude. Thus the physically relevant quantities of interest are differences in magnitudes and ratios of fluxes. How do we measure the flux or magnitude of an object that has been imaged?

Aperture photometry is a technique used to extract the brightness of astronomical objects from imaging. Photometry typically involves placing a circular aperture over an object of interest, measuring counts in adu, and subtracting off the sky flux in the aperture region; the sky itself is measured in an annulus external to the aperture. See figure 2.3 for a graphical representation of the method.

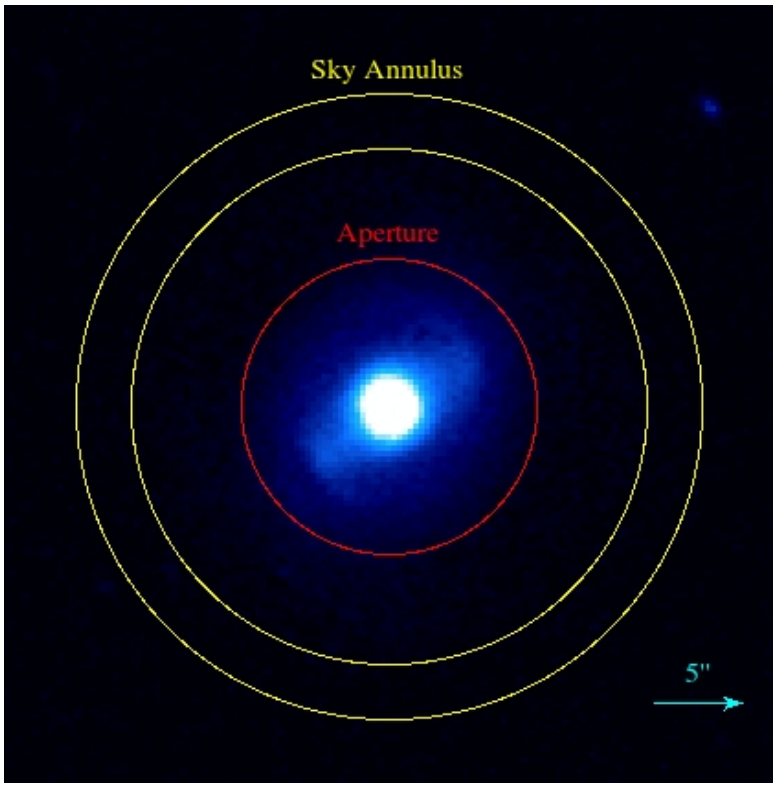

Figure 2.3: *Example of aperture photometry using a galaxy found in J-band WIRCam data. The vector shows the scale of the image; the sky annulus has a width of 3".*

To verify the effectiveness of the detrending and image stacking procedure as well as the accuracy of WIRCam's zero-point calibrations, we performed photometry on Arp 220 and compared with previous measurements. We used the IRAF task *qphot* which allows the user to select the size of the aperture, annulus, and specify the center of the object. It also allows for the optional use of a centering box that iteratively searches within the vicinity of the given coordinates for the exact peak in flux which is then used as the aperture centre.

The output brightnesses represent instrumental magnitudes, and several corrections have to be applied to convert to apparent magnitudes in a standard photometric system. The first is to account for exposure time, given that flux is in units per second but exposures span multiple seconds. The second correction is for the zero point. It is determined based on measurements of several reference stars in each WIRCam chip. The zero point is conventionally normalized to one second of exposure time. Further, the zero point is assumed to be constant over each observing run and is listed in the

fits header of each image (see table 2.4 for typical values in each filter). The third

Filter	ZP
J	23.6
H	23.8
Ks	23.0

Table 2.4: *WIRCam typical zero points in each filter under the Vega standard photometric system.*

correction is for atmospheric extinction which depends on the airmass at which the observation is taken; at greater airmasses, the observed brightness is reduced from light passing through a thicker segment of atmosphere. As such the airmass correction will be negative since the actual brightness will be greater (and magnitude less) than that measured. Airmass corrective terms specific to the Mauna Kea summit that we adopt are given on the WIRCam specifications webpage[2] as $k_J = 0.05$, $k_H = 0.03$ and $k_K = 0.05$ per airmass in the J, H and K bands respectively. Note that the zero points for each run are given at an airmass of one, an additional consideration that must be accounted for. Last is a colour correction which may arise from the difference in spectral response between the telescope filters and that of the standard system. While there is no measurement listed for this term on the WIRCam page, it is expected to be quite small and thus negligible due to the similarity between CFHT near-IR filters and the standard Johnson filters. To determine an apparent magnitude, sum the terms above:

$$m = -2.5 \log \left(\frac{counts}{t} \right) - k(a-1) + ZP \tag{2.3}$$

where counts is the aperture flux in adu, t is exposure time in seconds (values are given for each filter in table 2.1), k the appropriate airmass corrective term, a the airmass of observation and ZP the zero point. Expanding the logarithm yields

$$m = -2.5 \log(counts) + 2.5 \log(t) - k(a-1) + ZP. \tag{2.4}$$

We used a growth curve, which plots magnitude against aperture size, to find the ideal aperture encompassing the entirety of Arp 220 (see figure 2.4). It is clear the

[2]http://www.cfht.hawaii.edu/Instruments/Imaging/WIRCam

brightness levels off at an aperture radius of approximately 90 pixels, the value that we henceforth adopt.

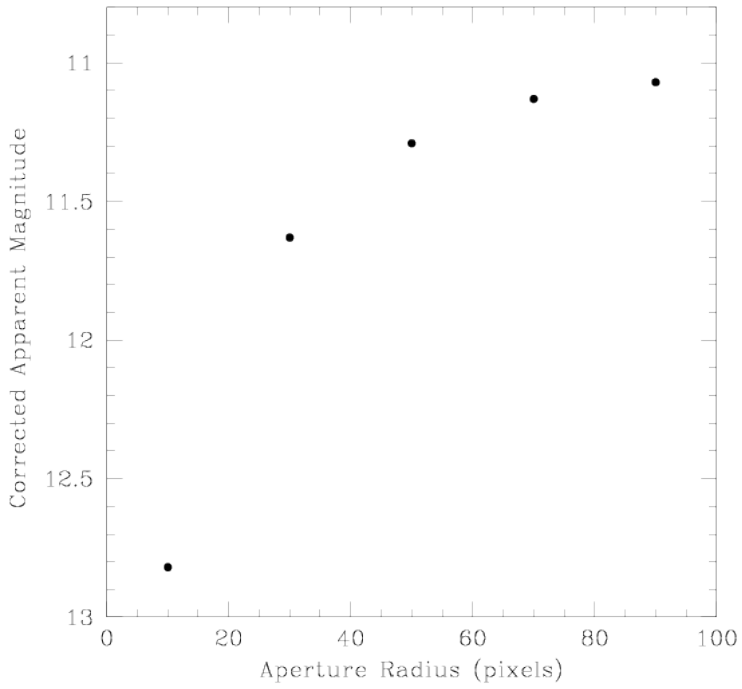

Figure 2.4: *Arp 220 J-band growth curve. A constant sky annulus with* $r_{inner} = 100$ *pixels and a width of 10 pixels was utilized for each measurement.*

We then performed photometry for each of the nine epochs available during the first data release at the time using the same sky annulus as employed in figure 2.4. Results are shown in table 2.5; WIRCam quoted magnitudes are the mean over all nine observing nights. We also provide 2MASS photometry for comparison. While the 2MASS filters differ from those on WIRCam, they are similar enough to form a solid basis of comparison and excellent agreement is found. As such the WIRCam zero point calibrations appear quite accurate.

Filter	WIRCam				2MASS			
	$\lambda_o(\mu m)$	$\Delta\lambda(\mu m)$	$\bar{m}$	σ_m	$\lambda_o(\mu m)$	$\Delta\lambda(\mu m)$	m	σ_m
J	1.252	0.158	11.057	0.014	1.235	0.162	11.035	0.026
H	1.631	0.289	10.287	0.019	1.662	0.251	10.306	0.028
Ks	2.146	0.325	9.827	0.024	2.159	0.262	9.852	0.036

Table 2.5: *Comparison of WIRCam and 2MASS Arp 220 photometry, including filter specifications. The bandwidth of each filer is denoted by $\Delta\lambda$. Note that even though the filters are not identical, agreement within errors is found. The uncertainty quoted in the WIRCam data is systematic and due to the spread in measurements between individual epochs; photometric errors, which were insignificant in comparison, are not included.*

Next we characterize the WIRCam detector.

2.4 WIRCam Gain and Readout Noise

2.4.1 Readout noise

Due to the elaborate process by which the imager registers detected photons and converts to adu, noise is introduced from the electronics anytime the infrared array is read out, even if no photons are detected. This is just one of several sources of noise in the detector. The noise present at zero signal is called the readout noise, and it is an important quantity to characterize in order to better understand WIRCam. This can be accomplished using flat fields; due to the uniformity of the flat source, and the expectation that all pixels should read the same value, these frames allow for a quantification of the internal electronics without concern of external influence. From the data header file, the value of the readout noise is $n_r = 7.9 \pm 2.6$ adu which will be our baseline for comparison. In general read noise is not a significant source of noise; for typical levels of signal, it is overshadowed by other sources of noise that we now discuss.

2.4.2 Gain

The number of photons impingent upon a pixel of the detector (or the number of electrons generated) does not share a one-to-one correspondence with the value of

output signal in adu. Instead a factor of proportionality relates the two, denoted as the gain of the detector and described by

$$S_e = gS_{adu} \tag{2.5}$$

where S_e and S_{adu} are the signal in electrons and adu respectively and g the gain in units of e^-/adu. The WIRCam gain is quoted as $g = 3.8 \pm 0.2$ e^-/adu.

We have already discussed readout noise, but there exist two more sources of noise we must consider. A fundamental noise contribution is referred to as photon noise and is a consequence of the quantized nature of light. In a given time interval, the number of photons a steady light source will emit is described by a Poisson distribution. Thus there will be a purely statistical uncertainty associated with the quantity of photons collected by the detector, described by the square root of equation (2.5). Relation (2.5) gives the signal in units of electrons, however pixel counts are given in adu which is therefore the more practical unit to work with. Dividing the photon noise in electrons by the gain will yield the noise in adu as

$$N^2_{photon} = \frac{S_{adu}}{g} \tag{2.6}$$

where henceforth S denotes the signal in adu.

A third contribution to noise comes from pixel nonuniformities, essentially why flat fielding is necessary. This effect is modelled via

$$N^2_{pixel} = kS^2 \tag{2.7}$$

in which k is a nonuniformity constant assumed to be quite small (typically ~ 0.01). Adding the square of the readout, photon and pixel noise (i.e. assuming they are uncorrelated) yields the total square noise in adu, given by

$$N^2_T = n^2_r + \frac{1}{g}S + kS^2. \tag{2.8}$$

where n_r is the readout noise. Note the read noise is constant, has no dependence on signal, and is typically quite small (much smaller than the other terms for broadband filters).

Each noise term dominates a different signal region. At low signal levels where the signal is of the same order of magnitude as the read noise, the readout noise will

prevail. Once the signal increases, the impact of readout noise will be overshadowed by photon noise which will begin to dominate. As the signal rises even higher the pixel noise will eventually dominate as the effect of the nonuniformity constant k starts to become significant. The difficulty lies in the ambiguity in determining the signal level at which each regime begins and ends, leaving some uncertainty in the modelling of noise.

2.4.3 Dome flats

We quantify the read noise and gain of WIRCam for a few purposes. These quantities were measured in the early days of WIRCam but the procedure has not been repeated for many years. As such, re-measuring provides a check of the consistency of the camera instrumentals over time. In order to measure the read noise and gain, we require a dataset that probes a wide range of signal in order to encompass all noise effects discussed above. A series of dome flats taken in 7 WIRCam filters (J, H, K, Y, H2, OH2, BrG) are used for this purpose. In each filter, 30 short exposures (3-5 s each) were taken of the CFHT dome from inside, 15 with the lamp on and 15 with the lamp off. Due to the inclusion of both brightly and non-lit exposures, measurements spanned a large range in signal.

Two 20x20 pixel regions were chosen in each flat field and the signal and noise were found in each using IRAF's *imstat* procedure. Regions were selected such that they displayed no apparent pixel variations and were located near the centre of the detector to reduce any uncertainty due to potential edge fringing effects. The square noise was plotted versus the signal, and a quadratic polynomial of the form ax^2+bx+c was fitted to the data; see figure 2.5. Curves were fitted to all points except the most extreme two sets (on the far right) in each filter to obtain a better estimate of the gain; by avoiding the outermost pixel noise points, the error in the gain term is reduced.

In total there were two filters (J and H) that contained almost zero signal in the lamp-off exposures (the leftmost points in figure 2.5), and we used measurements in these filters to estimate the readout noise. The average noise value was found for each set of 15 exposures, and the mean of these was determined, giving a readout noise of $n_r = 7.28 \pm 0.15$ adu. We find excellent agreement with the theoretical value of $n_r = 7.90 \pm 2.60$ adu.

It is clear from figure 2.5 that these flat fields probe mainly the readout noise and pixel noise regions, with a large gap in the middle. This gap accounts for the relatively

large errors in the gain values, as the value for the linear term b in the polynomial fit depends considerably on the noise behaviour in this region. Nevertheless the values for the gain largely agree with the theoretical value of $g = 3.80 \pm 0.20\ e^-/\text{adu}$; an average of each region yields a gain of $g = 3.88 \pm 1.08\ e^-/\text{adu}$.

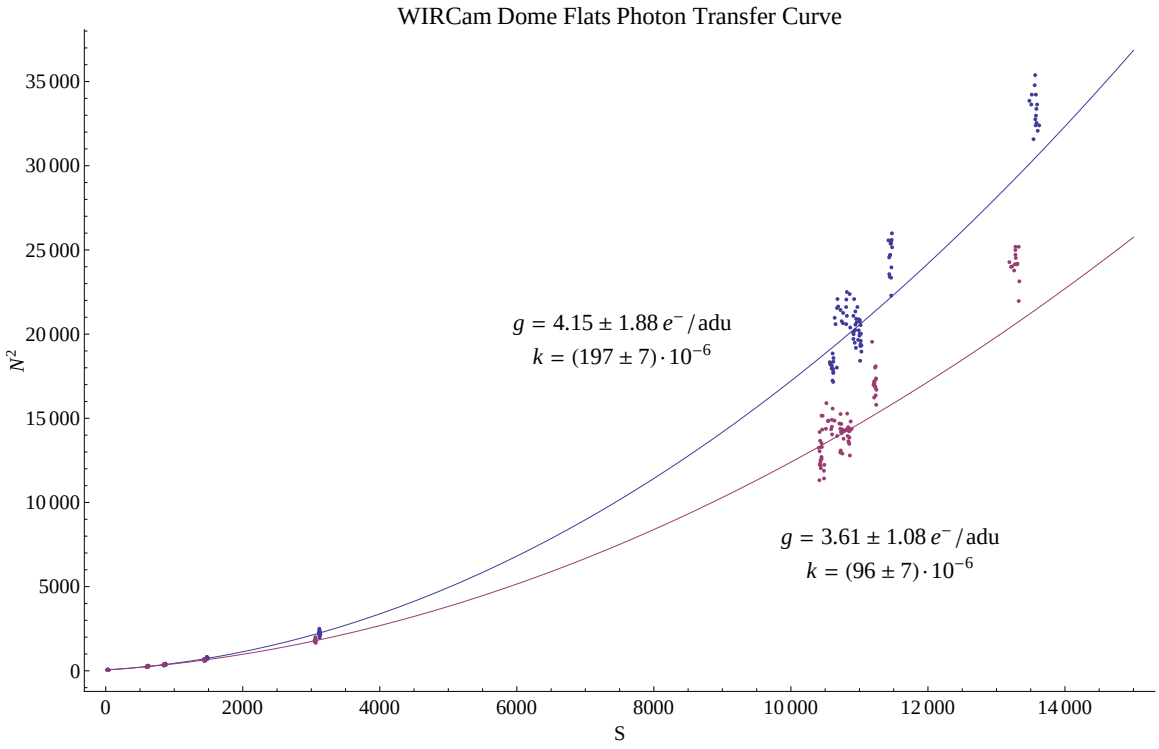

Figure 2.5: *Composite photon transfer curve for the two regions sampled. From each fit, the gain and pixel noise coefficient are shown, along with the quadratic fits as discussed in the text.*

The distinction between sources of noise becomes much more apparent when we plot figure 2.5 in logarithm-space. The log-log plot for both data sets is shown in figure 2.6 with the different noise regimes approximately labelled. The gain is estimated using the photon noise region. In this regime, relation 2.8 can then be approximated as

$$N_T^2 \simeq \frac{1}{g} S \tag{2.9}$$

as the other two sources of noise have little effect. Taking the base-10 logarithm of both sides and simplifying yields

$$\log(N_T) = \frac{1}{2}\log(S) - \frac{1}{2}\log(g). \tag{2.10}$$

Therefore the slope of the log-log plot should be approximately 1/2 and the gain determines the y-intercept.

Instead of fitting two parameters (slope and y-intercept) of a line to the log-space dome flat plot, the y-intercept was determined using the gain found from the photon transfer curve (figure 2.5). This y-intercept was set constant, leaving the slope as the only remaining fitting parameter to test the degree to which the resultant line matches the four data points in the photon noise region. As can be seen in figure 2.6, the match is excellent and the fitted slopes are close to the expected value of 0.5, verifying that these four points do indeed lie in the photon noise region. It is also clear how a line fitted to the pixel noise points would be considerably steeper, resulting in a significantly decreased y-intercept, and consequently a skewed value of the gain.

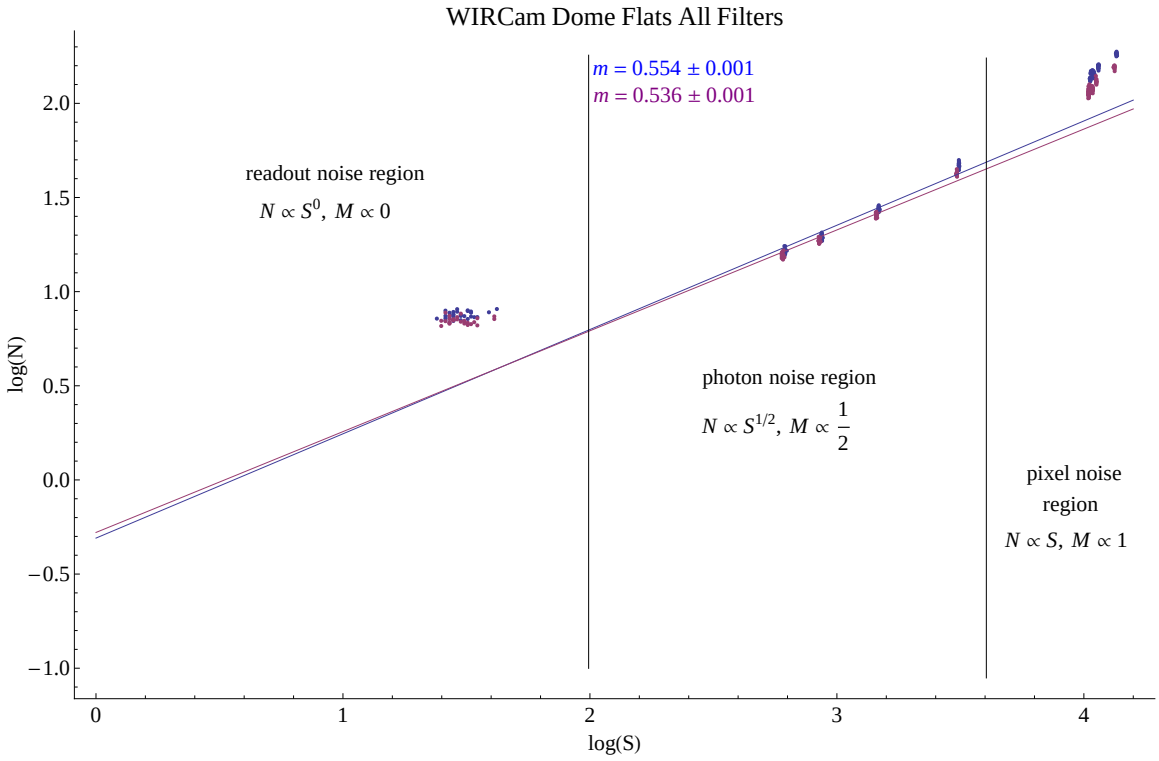

Figure 2.6: *Log-space plot of noise vs. signal for both curves of figure 2.5. The linear fits, performed as described in the text, are an excellent match to the photon noise data. The power law relation in each region, along with the implied logarithmic slope (M), are shown.*

In this chapter we gave an overview of previous infrared supernova surveys, moti-

vating our monitoring survey of Arp 220. We described our observations of Arp 220 using WIRCam on the Canada-France-Hawaii Telescope, along with the treatment of image processing. We performed absolute photometry in order to verify the WIRCam zero point determinations and found excellent agreement with prior 2MASS measurements. Further, we explored and measured the gain and readout noise of the detector using dome flat fields and found excellent agreement with previously measured values. In the next chapter we develop and carry out a variety of methods in attempt to locate supernovae in the data.

Chapter 3

Supernova Search in Arp 220

We employ a variety of data analysis techniques in attempt to detect supernovae in Arp 220. Section 3.1 outlines a point spread function matching procedure and presents image subtraction results. We perform differential photometry on the nuclear region of Arp 220 in section 3.2. Lastly section 3.3 details our method to subtract background light from Arp 220 using NICMOS data.

3.1 Point Spread Function Matching

We carried out a visual inspection of aligned and detrended images at each epoch in attempt to locate any supernovae by eye. This involved changing the pixel scale to emphasize brighter objects in the field. No supernovae were apparent; however the human eye is not the most reliable of scientific instruments. We now develop a more rigorous method to search for SNe.

While a visual search is sensitive to supernovae in the outer/circumnuclear regions of Arp 220, sensitivity greatly declines in the nuclei. Flux increases induced by nuclear supernovae would be effectively masked by the dominating brightness of the nuclei. Yet there is good evidence to suggest that most SN activity in ULIRGs occurs in the nuclei. Optical spectrometry of ULIRGs indicates that during the progenitor mergers, gas depletion proceeds from the outer disk inwards (Soto & Martin, 2010). Consequently most star formation will occur in the inner regions of these galaxies (within 1 kpc or less), and therefore type II supernovae are mainly expected to concentrate in the nuclei. Cresci et al. (2007) even speculate that a centralization of star formation within 200-300 pc may have explained the non-detection of SNe

in their NICMOS starburst survey. This condensed starburst hypothesis provides a possible explanation as to why no supernovae were spotted in the outer regions of Arp 220 when at least one would be expected (in the galaxy as a whole) in the time frame spanned by WIRCam observations. At the distance of Arp 220, 1 kpc covers approximately 3 arc seconds; this entire region is dominated by the bright nucleus of Arp 220 which would mask any SN light. Thus distinguishing supernovae by eye in this region is not possible. Instead, in order to search for supernovae it becomes necessary to subtract off a template of the galaxy from each observation and search the residuals for transient objects. This can be done via point spread function (PSF) matching and subsequent image subtraction (see section A.2 in the appendix for an overview of PSFs and PSF matching).

3.1.1 Method

The PSF-matching procedure makes use of convolutions; see section A.3 in the appendix for the relevant background theory. There are several ways to estimate the convolution kernel. The program *psfmatch3* (developed by Chris Pritchet; see Fraser et al., 2008) uses a least squares minimization procedure, whereas IRAF's *PSFmatch* utilizes Fourier transforms. *psfmatch3* was producing unexpected residuals after PSF matching, and so we settled on using the IRAF procedure.

PSF matching procedure

The procedure developed is outlined below.

1. Align images using the Groth algorithm on a square region 2100 $\times$ 2100 pixels centered on Arp 220. Images must be accurately aligned to within better than one pixel to reduce subtraction residuals; typical alignment was good to within 0.05 pixels or less.

2. Use Chris Pritchet's *findiso* to determine PSF at each epoch and locate the poorest quality PSF to use as a reference. The code finds isolated stars in an image by searching for intensities within a range specified by the user. It then fits Moffat profiles to each star and adds the residuals from a residual lookup table to construct a final mean PSF.

3. Use IRAF's PSFmatch to match PSFs between images. The worst-seeing epoch is used as the reference to match, and the kernel is determined using the PSFs (as fits files) output from *findiso*.

4. Subtract the first epoch of observations from each successive epoch to search for residuals.

3.1.2 Results

PSF-matching worked well for J and H data, but produced large residuals around Arp 220 in the K filter. In general PSF-matching often has difficulty with the K filter for reasons unknown. One theory is that aliasing starts to become an issue in this wavelength range. Aliasing can occur if the sampling is less than twice the FWHM; this means, with the 0.3 arcsec pixels of WIRCam, if the seeing is better than 0.6 arcsec aliasing will become an issue. Alternatively, in our K-band data particularly the central flux values in Arp 220 were quite high (approaching saturation) which may have produced residuals during PSF-matching. In the case of Arp 220, the nuclear flux in the K-band was significantly greater than in the other two filters; this may have caused issues when flux matching between images was attempted if pixel values neared saturation. Sample residuals are shown for J-band data, alongside original images, in figures 3.1 to 3.4 below.

No supernovae were apparent in the residual images over all filters. However, nuclear residuals as seen in figure 3.4 are common when performing ground-based difference imaging, reducing the sensitivity to SN detection in these regions. These residuals are introduced during the subtraction process itself, and typically prevent the detection of SNe, even bright ones ($m_k < 17$), within the central 2-3 arcsec of the nucleus (Cresci et al., 2007; Mannucci et al., 2003). There are a few potential causes of such residuals: the strong brightness gradient in the nuclear region can prevent accurate PSF subtraction; distant galaxies have more sharply peaked nuclei resulting in more noise post-subtraction relative to the peak brightness; even slight misalignments between images can cause subtraction residuals.

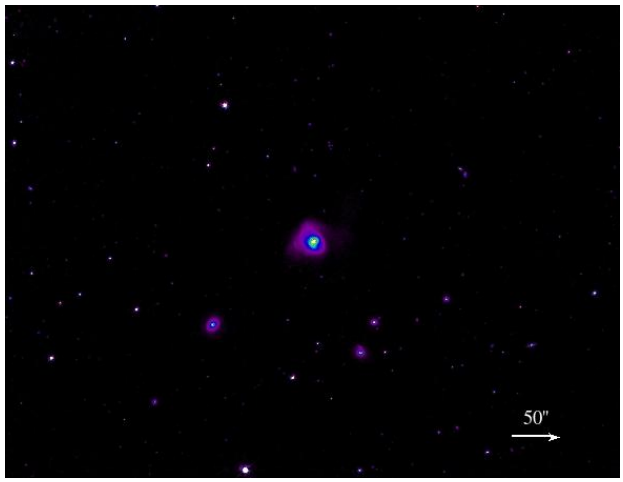

Figure 3.1: *Original J-band image stack centered on Arp 220. Only a small section of the whole 4-chip mosaic image is displayed.*

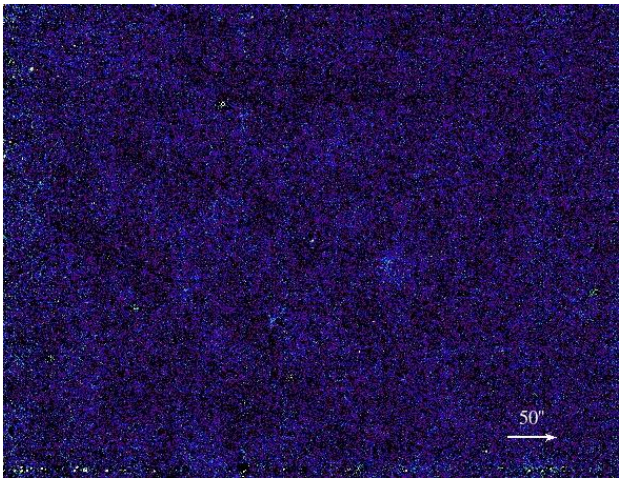

Figure 3.2: *Sample residual in the J-band with the same field of view as figure 3.1. Note how almost all stars in the image effectively subtract off, along with Arp 220.*

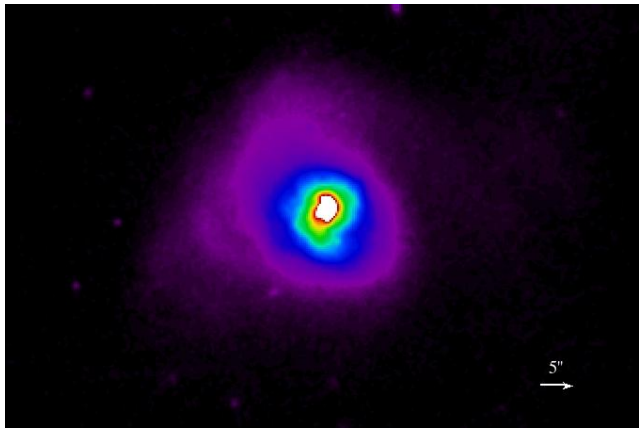

Figure 3.3: *Zoom in on Arp 220 from figure 3.1. Note the pixel intensity scale has been adjusted to emphasize the nuclear region.*

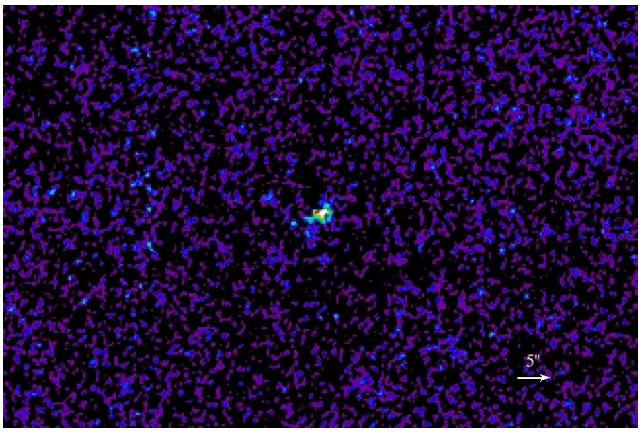

Figure 3.4: *Zoom in on the position of Arp 220 from figure 3.2, aligned to figure 3.3. Note the nuclear residuals, commonly found in ground based difference imaging.*

A region of non-detectability between 2 and 3 arcseconds in size corresponds to roughly 10 pixels on the WIRCam detector; the nuclear residuals were consistently seen to span an area of approximately this size. This region corresponds to about 1.1 kpc in radius; since the crux of the starburst may be taking place interior to this region, we may be missing SNe. To reduce the region of residual obscuration, we require improved spatial resolution such as can be achieved via space-based observations; Cresci et al. (2007) found that NICMOS residuals only plagued the inner ~ 0.35 arcsec of Arp 220, a region just 130 pc in physical size as opposed to the 2-3 arcseconds typical of ground-based imaging. Ground-based adaptive optics provides another alternative for reducing the region of nuclear residuals; Mattila et al. (2007) discovered a core collapse supernova with the European Southern Observatory Very Large Telescope at a distance of 1.4" (500 pc) from the nucleus of the LIRG IRAS 18293-3413.

While we have ruled out the presence of any SNe outside the Arp 220 nuclei, the existence of nuclear residuals prevents any potential detection of nuclear supernovae. Since there are reasons to believe the starburst is highly centrally concentrated, and consequently that the SN distribution will be spatially correlated with the star formation activity, we may still be missing SNe. We attempt to discover nuclear supernovae through the use of photometry.

3.2 Differential Photometry

Point spread function matching revealed no SN candidates in the outer regions of Arp 220, however the starburst is likely highly concentrated in the central nuclear region of the galaxy. As such supernovae may have occurred in this area throughout the duration of observations but remain undiscovered due to nuclear residuals. To search for the presence of these potential SNe in the form of flux variations, we perform differential photometry on the galactic nuclei. If a SN is present, it should reveal itself in the form of an increase in nuclear flux and then a decay over roughly 100 days. Therefore constructing light curves in each filter is our ultimate goal. Both the shape and peak magnitude of the light curve will give clues as to the nature of any changes in brightness.

The basic concept behind differential photometry is to compare the brightness of one object to several reference objects in the same field of view, preferably within close proximity to the object of interest. It is imperative the references are constant in

magnitude to ensure that any shifts in brightness are therefore due to changes in the flux of the object of interest and not the references. In this instance, we choose stars as references. Differential photometry is highly effective because it compares relative fluxes, thus eliminating any extraneous effects such as flat fielding issues or errors in zero-point determination. For this reason it is a preferable method to absolute photometry, especially for our purposes of extracting brightness changes due to any potential transients.

3.2.1 Method

We adopt the following method:

1. Choose 5 reference stars that exhibit minimal variation in brightness over the course of Arp 220 observations. See subsection 3.2.2 for elucidation of reference star selection.

2. Perform photometry on the nuclear region of Arp 220 and on each reference star.

3. Calculate the difference between the instrumental magnitude of Arp 220 and the reference stars at each epoch:

$$\delta m_j^i = m_N^i - m_j^i \tag{3.1}$$

   where N represents the nucleus, i the epoch of observation ($i = 1, 2, ..., 18$) and j the reference star number ($j = 1, 2, ..., 5$).

4. Compute the baseline magnitude difference by taking the mean difference over all nights for each reference star:

$$\overline{\delta m_j} = \frac{1}{18} \sum_{i=1}^{18} \delta m_j^i. \tag{3.2}$$

5. Calculate the change in magnitude difference from the mean at each epoch:

$$\Delta m_j^i = \delta m_j^i - \overline{\delta m_j}. \tag{3.3}$$

If the nuclear region of Arp 220 were constant in brightness, Δm_j^i would be equal to zero.

A few notes on the above procedure. The choice of baseline is important, as it is the point of comparison for each epoch. Choosing a single epoch for this task may skew the results; we have no prior knowledge as to whether a single epoch has any additional or reduced flux; the epoch chosen may happen to contain a large brightening event. For this reason the mean over all epochs serves as an appropriate baseline. Given 18 different nights of observation, the mean difference should be a reasonable approximation to the true, typical difference between the magnitude of the Arp 220 nucleus and the magnitude of each reference star.

The analysis was performed relative to individual reference stars. It is also possible to combine the final values that arise out of step #5 by taking the mean over all five reference stars; however this would not isolate whether the same behaviour occurs with respect to each reference star but only present an overall trend. As such it is more fitting to compare the Arp 220 nucleus to each reference star individually as a consistency check. This approach will also provide an alternative verification of our choice in reference stars based on the agreement between the light curves with respect to each star.

What region of the nuclei of Arp 220 should be analyzed? As mentioned previously, in our WIRCam data the two main W and E nuclei are not isolated but blended together. Furthermore, the sizes of the nuclei - the FWHM of the larger, W nucleus is barely one square WIRCam pixel (Scoville et al., 1998) - present a significant challenge to performing precision photometry. Consequently it is neither possible nor practical to attempt to place an aperture over each nuclear component. Instead, an aperture that effectively encompasses all nuclear components would be more appropriate. Two circular apertures were utilized and compared, with radii $R_{ap} = 5$ pix and $R_{ap} = 7$ pix (1.5 arcsec and 2.1 arcsec respectively). The aperture centre used was that quoted by Scoville et al. (1998) as the centre for all nuclear components, with no employment of a centering box. We used a sky annulus with inner radius 30 arcsec and a width of 6 arcsec, well outside the galaxy light.

3.2.2 Reference stars

The choice of reference stars is vital as they need to be bright enough to reduce photometric errors without reaching saturation, and they must stay roughly constant in

brightness over all epochs (i.e. they cannot be variable stars). Thirty candidate stars were manually picked from the WIRCam field with the requirement that they be visible in each epoch and stellar in origin (avoiding extended objects such as background galaxies). Photometry was performed on each candidate star using apertures with the same radii as those employed for Arp 220. The following was then implemented.

1. Calculate for each epoch the difference in instrumental magnitude of every unique pair of stars. That amounts to $N(N-1)/2$ difference plots, which for $N = 30$ is 435.

2. For each difference plot, calculate the systematic standard deviation. Note the total standard deviation (or root-mean square, rms) involves both photometric and systematic contributions, i.e. $\sigma^2 = \sigma^2_{phot} + \sigma^2_{sys}$. The photometric error is calculated by IRAF during the photometry procedure and includes photon noise (see equation (2.6)) and sky noise. Systematic errors on the other hand are due to imperfect image detrending which will never fully remove the instrumental signature from the data. These are much larger than photometric errors (which are typically less than a hundredth of a magnitude) and consequently we can consider just the former. The root-mean square between two stars is given by:

$$\sigma = \sqrt{\frac{1}{n-1}\sum_{i=1}^{18}(\Delta m_i - \overline{\Delta m})^2} \tag{3.4}$$

   where the specific observing epoch is i and n is the total number of epochs. The mean difference ($\overline{\Delta m}$) is taken over all 18 epochs whereas the difference on an individual epoch is denoted by Δm_i.

3. We identify the best candidate stars by scanning through the rms values for each star and locating those stars that consistently display the smallest variations with respect to all others. Such stars stay roughly constant in brightness relative to a large number of other test stars and thus serve as ideal references. Since we analyzed a sample of 30 stars, each star has 29 difference plots to search. To find these promising reference stars, a threshold value of σ is chosen and for each star the frequency with which its rms value lies below this cutoff is measured. The stars with the top five frequencies were then appropriated as references.

The large sampling of candidate stars provided a robust method for finding the most ideal references. While the same candidates were used in each filter, different sets of reference stars were chosen for J, H and K in the end based on the above analysis.

3.2.3 Results

Once a set of reference stars was chosen in each filter, the method of subsection 3.2.1 was applied. Typical aperture corrections were several hundredths of a magnitude and overshadowed by the systematic and photometric uncertainties; therefore we can safely omit them.

A brightness peak in Arp 220 was observed across all reference stars in the K and H filters at epoch #6 (day 55). See figures 3.5 - 3.10 for a representative sample all plotted on the same scale for ease of comparison. Note how the brightening event at epoch six is not present in the reference star plots for K and H.

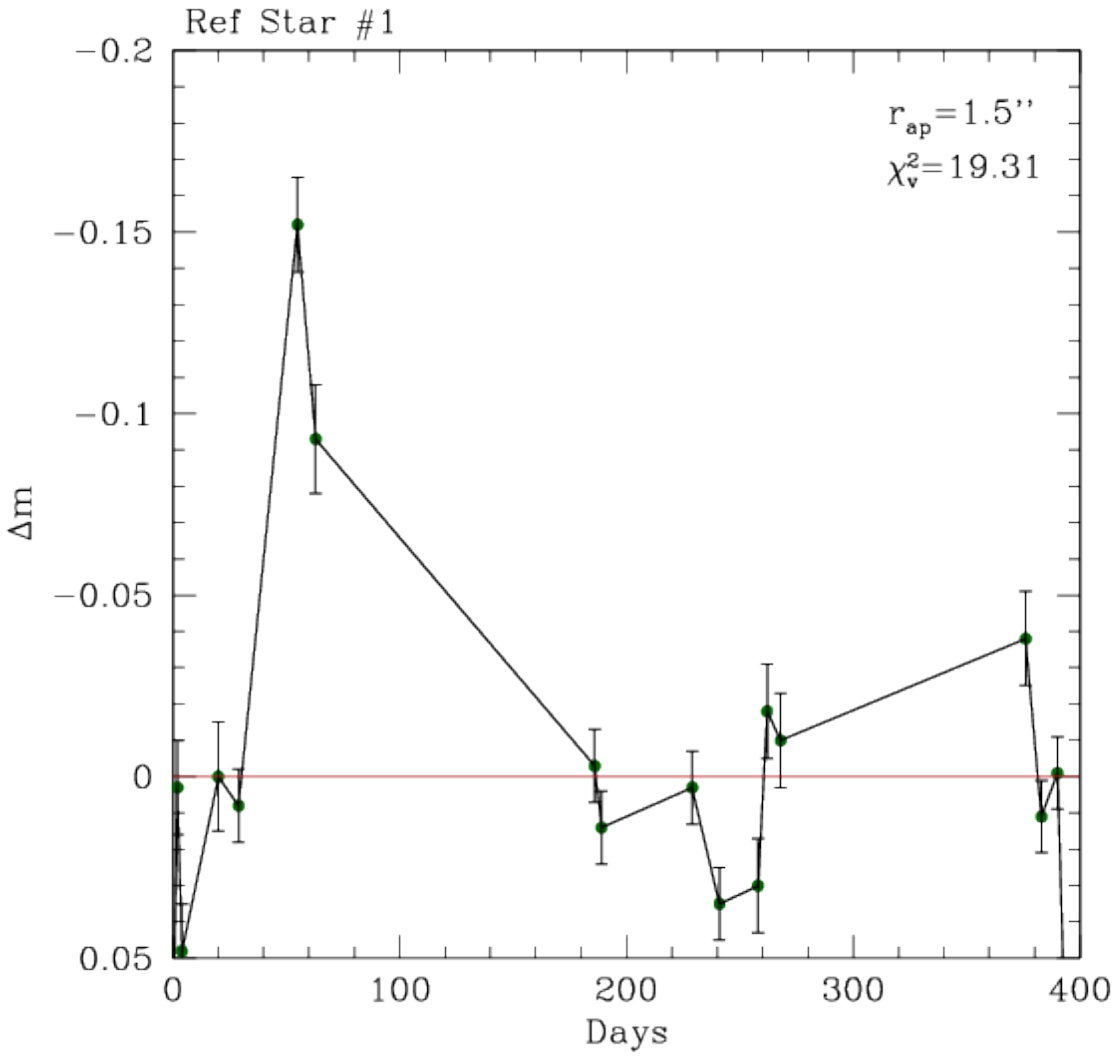

Figure 3.5: *Sample Arp 220 nuclear light curve in the K-band from differential photometry relative to a single reference star. Photometry was performed using an aperture radius of 1.5 arcsec as described in the text. The red horizontal line denotes the baseline- the mean difference between Arp 220 and reference star brightness. The chi-square value for the entire curve is given in each plot (see subsubsection 3.2.4).*

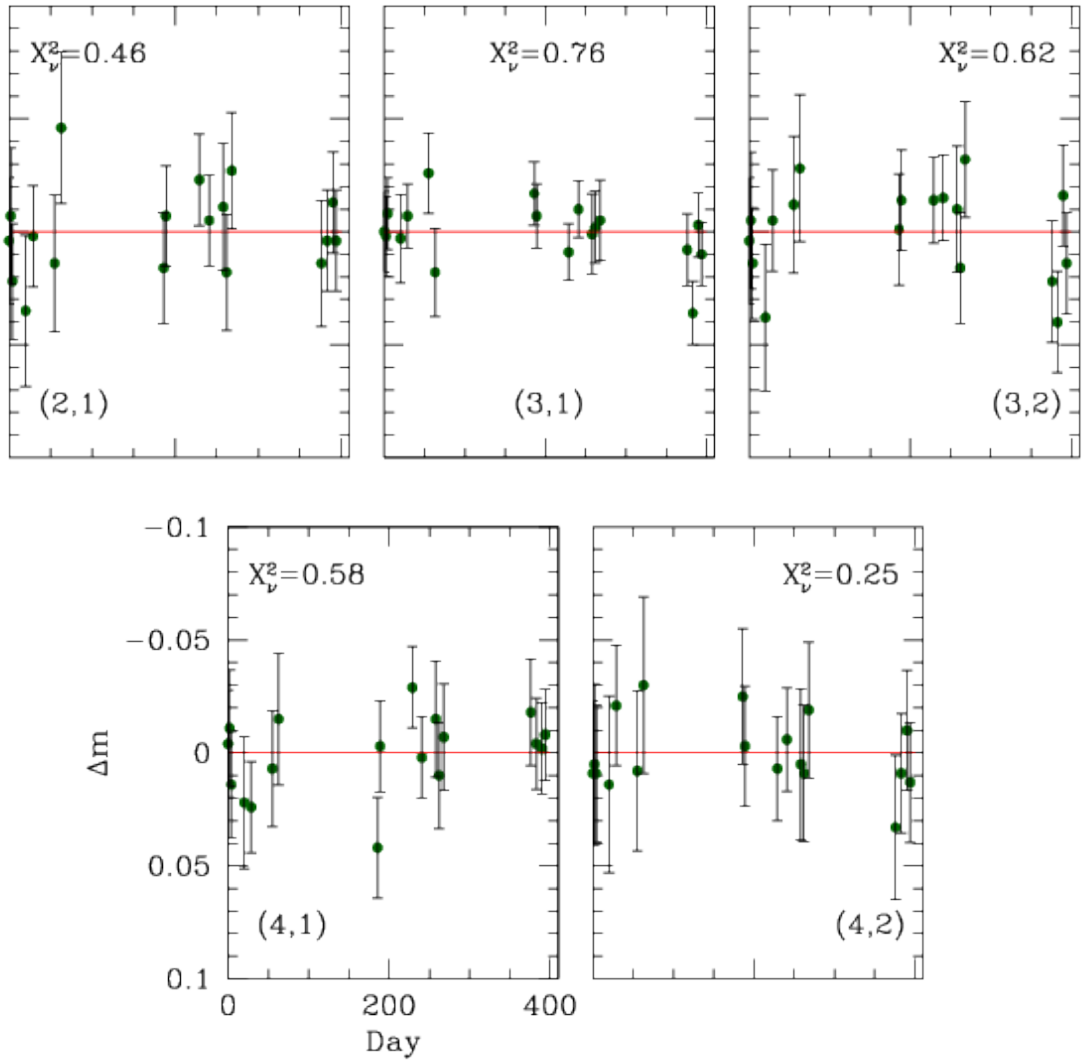

Figure 3.6: *Five reference star difference plots in K and the resulting chi-square value of each for an aperture radius of 1.5 arcsec. The red horizontal line is again the point of equal flux ratio between stars compared to the mean as discussed in the text. Errors originate from IRAF and have been scaled such that* $\chi^2_\nu \sim 1$*; this scaling was applied to the light curves as well. Reference star designations are given at the bottom of each plot as (star A,star B).*

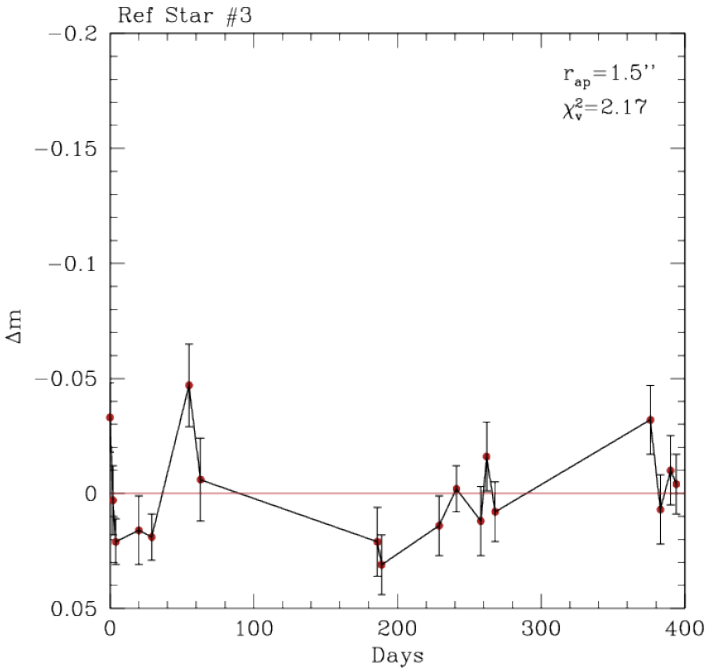

Figure 3.7: *Representative nuclear light curve in H.*

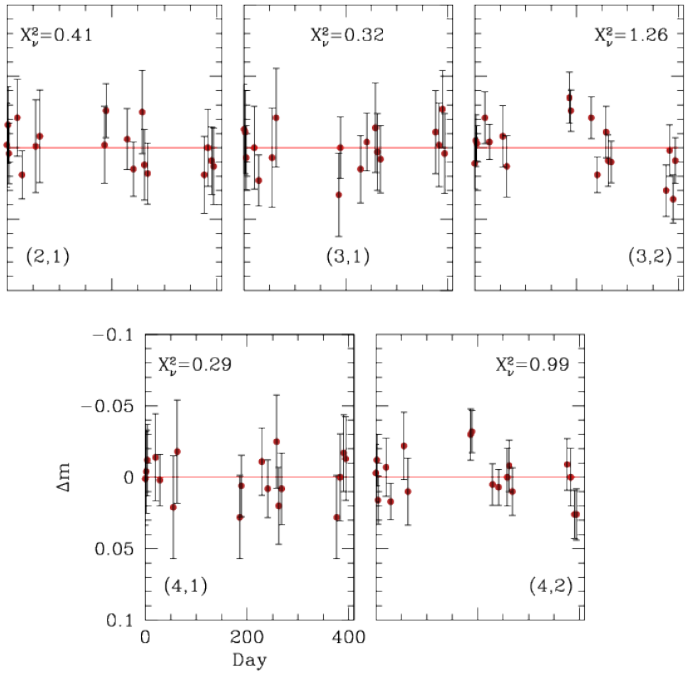

Figure 3.8: *Representative reference star difference plots in H.*

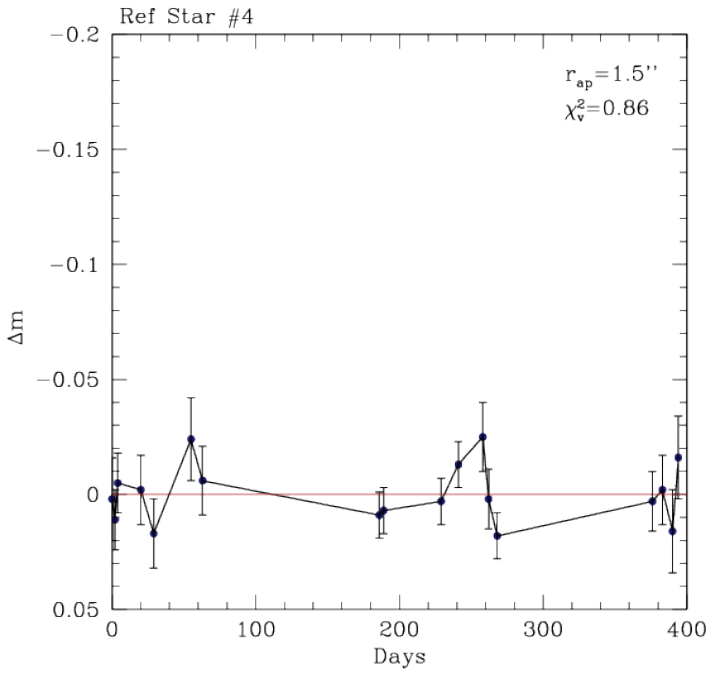

Figure 3.9: *Representative nuclear light curve in J.*

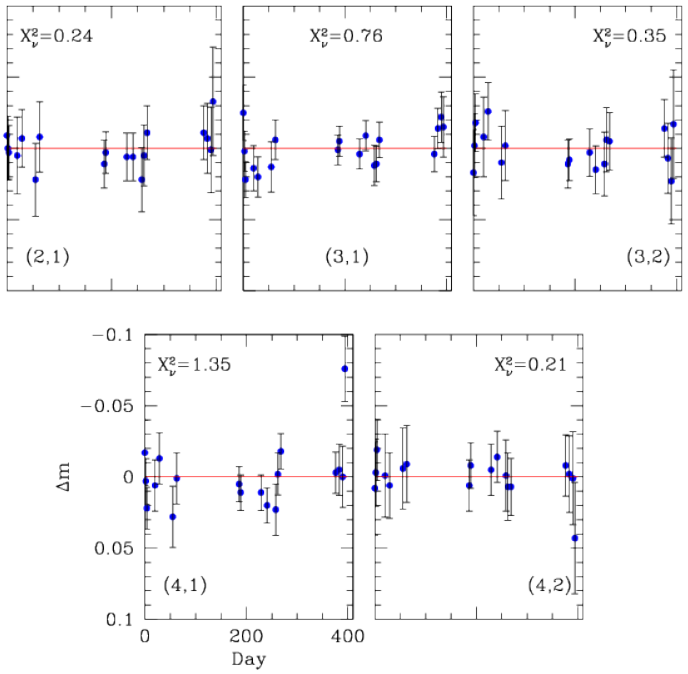

Figure 3.10: *Representative reference star difference plots in J.*

3.2.4 Statistical Analysis

We now determine the statistical significance of each light curve using a chi-square analysis. The chi-square statistic is defined and its application discussed in appendix section A.4.

Chi-square photometric application

It can be seen in figures 3.5 and 3.6 that there is a peak in the K and H data at the 6th observing epoch. Neglecting for the moment the issue of the absolute brightness of the event, in the K-band the peak appears to decay over a roughly 150 day period which coincides with the decay-time of a core collapse light curve (see e.g. Matilla & Meikle, 2001 template light curves). What is the probability of obtaining these light curves?

First we specify the null hypothesis which represents our model, and the alternative hypothesis.
H_o: There is no change in nuclear brightness between nights. In other words, the difference between the magnitude of Arp 220 and each reference star on every epoch of observation is constant and equal to the mean difference (within photometric errors).
H_ν: The nuclear brightness varies between observing epochs.
Note that the alternative hypothesis does not stipulate a source of nuclear variations, just that they occur.

Next we translate the chi-square theory developed previously into a form applicable to our data, which has 18 epochs. Since we determine a single parameter from the data points, specifically the mean brightness difference (the null hypothesis), there are $N - 1 = 17$ degrees of freedom. To calculate the value of reduced chi-square for a single light curve, we adapt (A.5) along with (A.6):

$$\chi^2_\nu = \frac{1}{17} \sum_{i=1}^{18} \left(\frac{\Delta m_i}{\sigma_i} \right)^2 . \tag{3.5}$$

Note that $\Delta m = \delta m - \overline{\delta m}$ in which δm is a relative magnitude (the difference between the nucleus and reference on a single epoch) and $\overline{\delta m}$ is the mean brightness difference; $\Delta m_i = 0$ for all i is the null hypothesis. Values of reduced chi-square are shown in each light curve above, as well as for all reference star difference plots. A scaling was applied to the reference star error bars such that $\chi^2_\nu \simeq 1$ and the same scaling was

used for light curve uncertainties which are propagated from initial IRAF photometric errors.

Based on the acquired χ^2_ν values, it is clear the light curve in K is statistically significant with an extremely low probability in all 5 reference stars, and $\chi^2_\nu > 1$ in H for 3 of 5 reference stars. In J, 3 of 5 references showed $\chi^2_\nu > 1$ due to a large spike on the 18th epoch; as mentioned previously due to poor observing conditions during this epoch these points should not be heavily weighted. Upon removal of epoch 18 all 5 stars show $\chi^2_\nu \simeq 1$. Further, an examination of reference star difference plots (see figures 3.6, 3.8, and 3.10) shows excellent consistency and minimal variation from the mean, confirming our choice in reference stars and reiterating our result.

We have extracted light curves in each filter relative to five reference stars for a total of fifteen curves. We see a statistically significant brightening in K with p-values $<<$ 0.001 and in some of the H light curves with brightness increases of approximately $\Delta m_K = 0.16$ and $\Delta m_H = 0.04$. Next we aim to quantify the precise absolute magnitude of these peaks using data from the Hubble Space Telescope.

3.3 Background Modelling

Examining the light curves of figures 3.5 and 3.7, a second flux peak is apparent at epoch #15 (day 376). The reason we focus on the brightening event of epoch #6 as opposed to that on epoch #15 is twofold: the former has a larger flux difference (most notably in K), and a subsequent period of decay that is reasonable for a core collapse supernova.

The peak magnitude differences found in the previous section via differential photometry are not a proper representation of changes in nuclear flux due to the presence of contamination from background galaxy light. In particular, the 1.5 arcsecond target aperture, while effectively encompassing the nuclei, also encompasses some amount of background emission from the circumnuclear regions of Arp 220. To quantify this, consider the components that the total emission (E) consists of: the nuclear flux (N), bulge flux (B) and flux of the variable component (P). Note that both nuclear and bulge flux contribute to background light. The total flux is just the superposition of all three components:

$$E = N + B + P. \tag{3.6}$$

We can find a rough estimate of the true peak brightness (without background

emission) using HST NICMOS archival data described in subsection 2.1.3. Since the western nucleus is the brightest and largest component, we will at the moment ignore contributions from the other nuclear sources. According to Scoville et al. (1998), the K-band apparent magnitude of the western nucleus in a $(0.92'' \times 0.58'')$ aperture is $m = 13.04$. Using a $0.90''$ diameter circular aperture on WIRCam K-band images from all epochs and correcting for the zero-point, we find the average apparent magnitude to be $m = 12.83$. Since the NICMOS aperture tightly encompasses the crescent-shaped western nucleus, ignore the bulge contribution to this magnitude; this cannot be done with the WIRCam measurement since a circular aperture was used. Further, the assumption must be made that the nuclear and bulge light do not differ between WIRCam and NICMOS. This is perhaps a reasonable assumption; however two factors must be kept in mind. First, the duration of elapsed time between observations - from 1997 with HST to 2012 with CFHT - makes no guarantee these components remain fixed in brightness. If Arp 220 does indeed harbour an AGN (or multiple AGNs), variations in its energy output within 15 years are easily possible which could potentially alter the brightness of the nuclei. A second, and perhaps subtler, effect lies in the difference between the HST and CFHT filters (see table 2.3), with no simple way to convert from one system to the other.

Thus using equation (2.1), we can relate nuclear and bulge light:

$$m_{N+B} - m_N = -2.5 \log \left(\frac{N+B}{N} \right) \tag{3.7}$$

in which the NICMOS magnitude is m_N and WIRCam magnitude m_{N+B}. This results in a relation between the fluxes (from relation (2.2)); using values mentioned above of $m_{N+B} = 12.83$, $m_N = 13.04$ we find

$$N + B = 1.213N. \tag{3.8}$$

Now consider the WIRCam brightening event and recall that in the K filter it was approximately 16% of the nuclear light (bulge + nucleus). Thus in flux,

$$N + B + P = 1.16(N + B). \tag{3.9}$$

Equation (3.9) states that when the peak is added onto the nuclear and bulge light, the result is a 16% increase in brightness. Inserting (3.8) into (3.9) results in a relation

between peak and nuclear flux, exactly what we are looking for:

$$P = 0.194N. \tag{3.10}$$

Using the measured NICMOS K magnitude of the west nucleus, and correcting to absolute magnitude via the distance modulus of Arp 220 ($m - M = 34.37$), we find a peak absolute magnitude of $M_K(P) \simeq -19.55$ from equation (2.1). Therefore from this rough estimate we find the true absolute magnitude of the peak to be at least -19.55; note this is not yet corrected for extinction, and thus will be made more luminous by a few magnitudes. A more rigorous technique can be employed to pinpoint the peak brightness with greater accuracy (see subsection 3.3.4).

An important detail when performing relative photometry on data from two different telescopes is to match aperture sizes. To determine the factor required, we must consider the resolution of each telescope. WIRCam has a sampling of $0.301''$/pixel whereas that of NICMOS is $0.076''$/pixel. In order to accurately compare photometry, the radius of each aperture must be matched to the proper scale:

$$\frac{r_{WIR}}{r_{NIC}} = 3.961. \tag{3.11}$$

Thus NICMOS has a sampling that is roughly four times better than that of WIRCam. In other words every WIRCam aperture will correspond to a NICMOS aperture with a radius 3.96 times greater in pixels. Using this factor ensures the physical area covered by each aperture does not differ between the two datasets.

3.3.1 Point spread function convolution

How can we quantitatively compare data from two completely different telescopes, one which is ground-based and another space-based? Although HST has a smaller mirror than CFHT (the former's 2.4m diameter compared to the latter's 3.6m), HST data - largely due to its position above the atmosphere which eliminates seeing - has a significantly better resolution than that of WIRCam. To effectively compare data, we can convolve the NICMOS images with the WIRCam point-spread function. By doing so we effectively transform the NICMOS image, taken in 1997, into a WIRCam image taken on the same date. This process can alternatively be thought of as PSF-matching between WIRCam and NICMOS. This method works because WIRCam has a much larger PSF than NICMOS; NICMOS data can essentially be considered

an “un-blurred” version of WIRCam data.

The WIRCam PSF from every epoch of observation in each filter was determined using *findiso*. Recall that the program produces a PSF for each image through an examination of isolated stars in the field. Since WIRCam mosaics feature all four infrared chips together, a significant sampling of stars is available for accurate PSF determination.

First we had to account for the difference in pixel size between the WIRCam and NICMOS detectors. Each WIRCam PSF was adjusted accordingly using IRAF's *magnify* routine. The PSF from epoch #6 was then convolved with the appropriate NICMOS image using IRAF's *fconvolve* algorithm included in the STSDAS package. See figures 3.11, 3.12 and 3.13 for a visualization including before and after images.

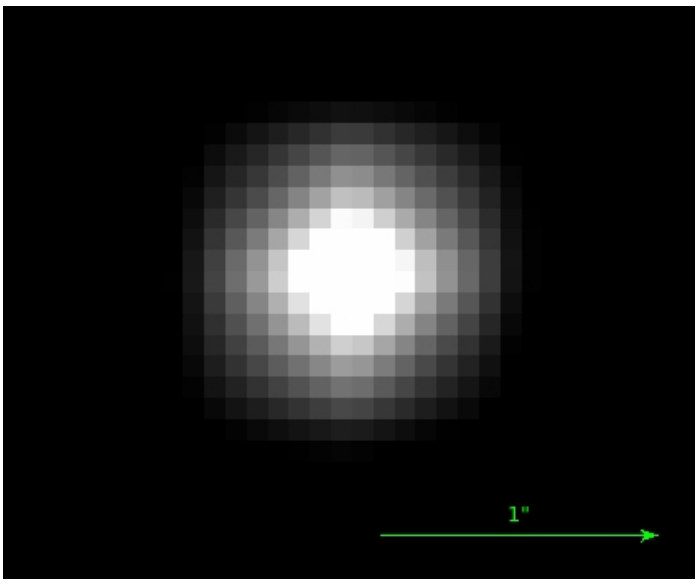

Figure 3.11: *K-band PSF at epoch #6 (after magnification) used for convolution with NICMOS data and constructed as described in the text.*

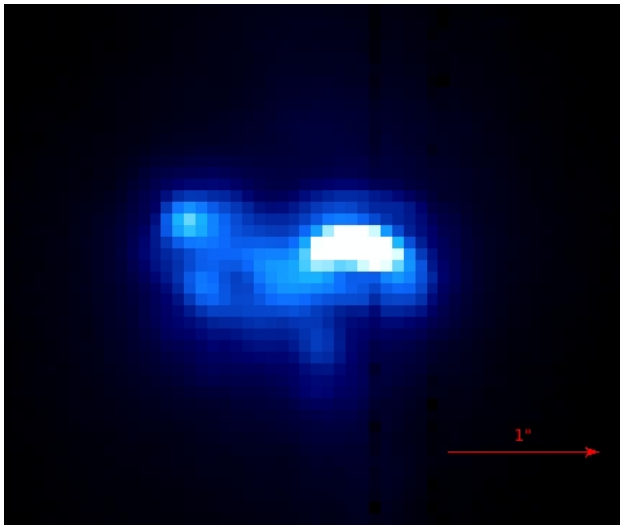

Figure 3.12: *Original NICMOS archival image in the F222M filter, zoomed in to the nuclear region.*

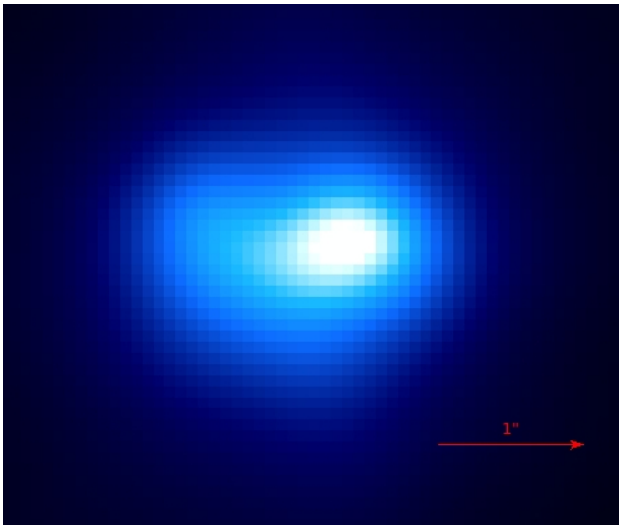

Figure 3.13: *NICMOS image of figure 3.12 convolved with the magnified PSF from epoch #6.*

3.3.2 Flux normalization

To reliably subtract off the background from the WIRCam data, the fluxes must be matched between data from the two telescopes. Once they are on the same relative scale, fluxes can be subtracted leaving only excess emission in the WIRCam data from any additional sources. First we must convert instrumental magnitudes to fluxes using a common scale.

We use WIRCam K-band data from epoch #6 and NICMOS K-band equivalent archival imaging to develop the method before applying it to the remaining filters. An appropriate reference was chosen based on the highest magnitude (faintest) photometric data point; thus $m_o = -6.0$ corresponding to $f_o = 1$ was adopted. Fluxes were then found using equation (2.2).

What is the most effective way to match the flux between each image? The fluxes out to a certain radius could be matched; however if the WIRCam data does indeed have excess emission, it would add in some degree of contamination. Instead, we match fluxes inside an annular region around the nuclei of the galaxy which we know will not vary. For an annulus with inner radius R_{inner} and outer R_{outer}, the flux contained is

$$f_{annulus} = f(< R_{outer}) - f(< R_{inner}) \tag{3.12}$$

in which the terms on the right side represent the total flux contained in an aperture of given radius. The choice of annulus is important since it must lie far enough from the nucleus to avoid contamination from nuclear light, yet not too far as to encompass an insignificant amount of galaxy light. The concept is outlined in figures 3.14 and 3.15.

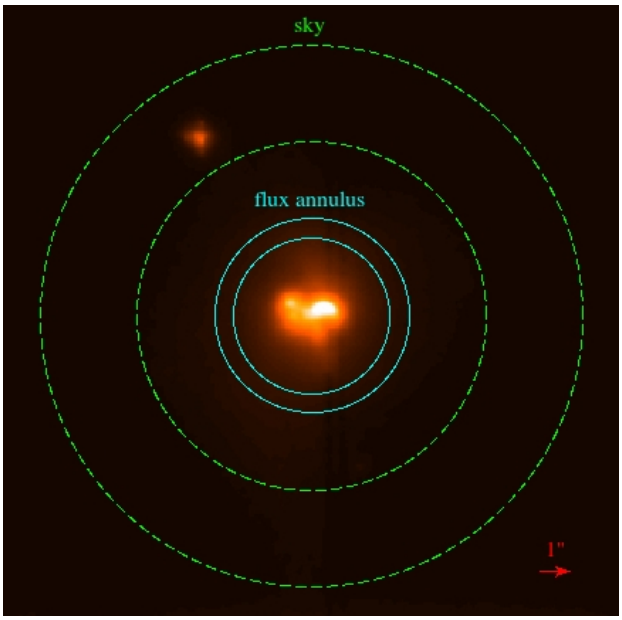

Figure 3.14: *Flux matching visualization for the NICMOS F222M image (non-convolved). The flux annulus has* $R_{inner} = 2.4$", $R_{outer} = 3.0$", *and the sky annulus lies between* $5.4" < R < 8.4"$. *The pixel scale has been set to emphasize the individual nuclear components and show that the annulus lies outside their influence.*

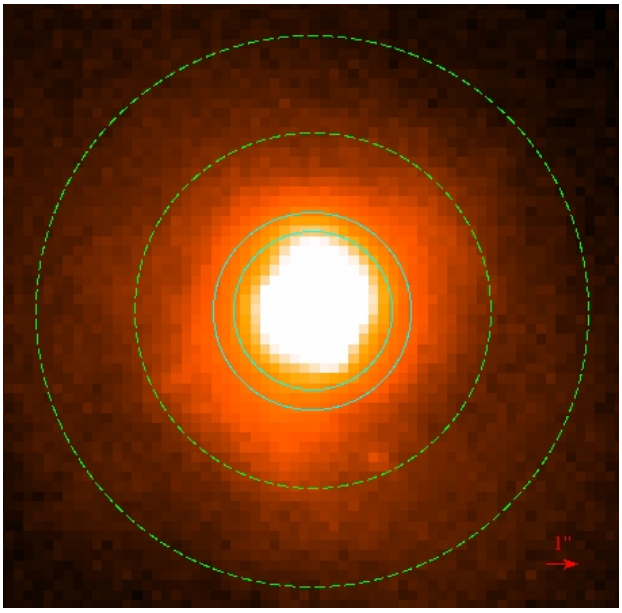

Figure 3.15: *Flux matching visualization for WIRCam K-band image with the same annuli as in figure 3.14. The pixel scale is much smaller in range to outline additional background galaxy emission.*

3.3.3 Photometric growth curves

Three different normalization annuli were tested. By calculating the flux in the annulus for both WIRCam and NICMOS images (after subtracting the sky) and taking the ratio, a flux conversion factor is found between the two. This factor was applied to scale the NICMOS flux up to the WIRCam flux, and the former was subtracted from the latter. Results in the form of a growth curve at the sixth epoch are displayed in figure 3.16.

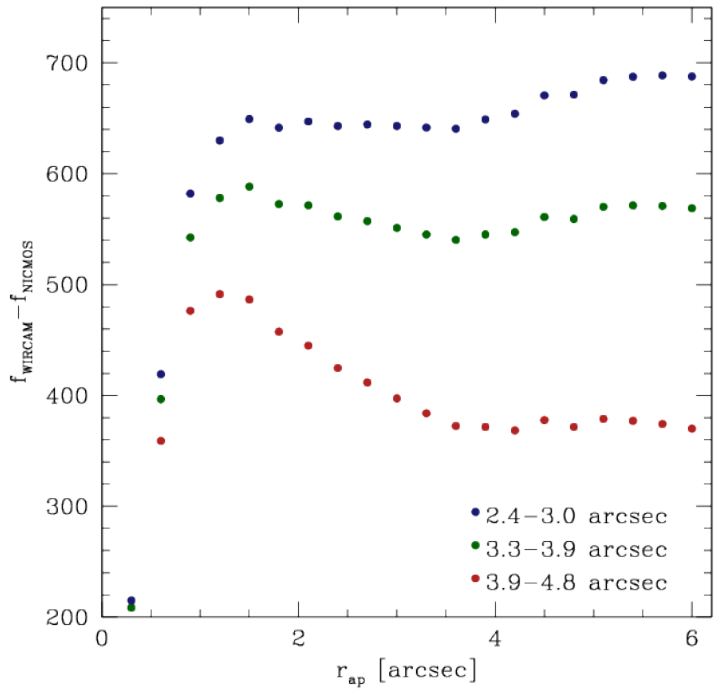

Figure 3.16: *Flux difference at epoch 6 after normalization in the K-band. Note the top curve corresponds to the situation shown in figures 3.14 and 3.15. The units of flux are arbitrary and bear no physical significance.*

We can see that the blue annulus works best since it provides what appears to be a stellar profile out to approximately 4 arcsec, after which background galaxy light begins to dominate. The green and blue growth curves, on the other hand, do not resemble a PSF as closely; it is possible these annuli lie far enough from the nuclei that they encompass an insufficient amount of light from which to flux match. To verify how closely the flux difference resembles that of the point-spread function, it can be

compared to the PSF profile. The blue flux difference of figure 3.16 was converted back to instrumental magnitudes using equation (2.1) and plotted concurrently with the profiles of the PSF on epoch #6 and the mean-PSF (figure 3.17).

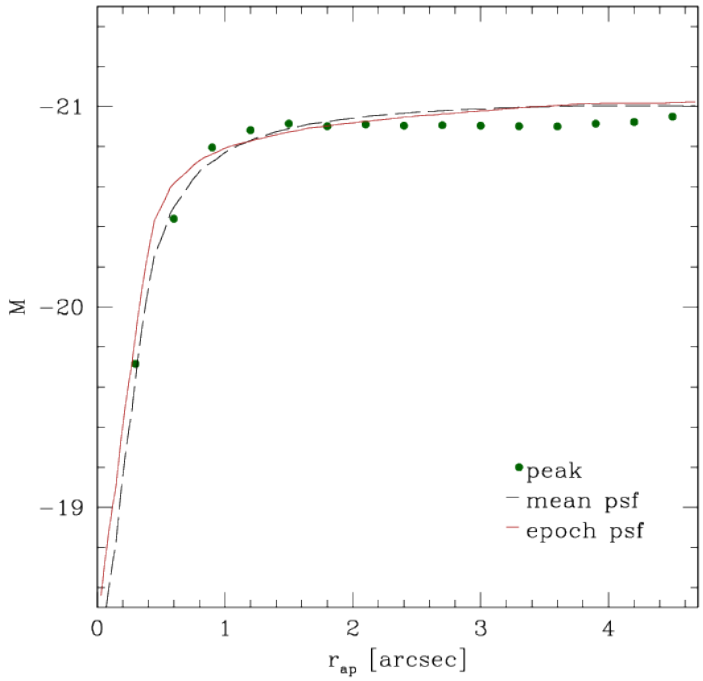

Figure 3.17: *Growth curve comparison between flux difference at epoch 6, the mean-PSF, and the PSF of this epoch. The vertical axis is in units of instrumental magnitudes.*

Barring some fluctuations which are to be expected when working with photometry in the dense nuclei of Arp 220, the peak in flux variability bears a strong resemblance to the growth curves of the point-spread function. Therefore the flux peak appears to be stellar in origin. This still does not distinguish between AGN activity and a supernova; a more precise measurement of the brightness is required. Further we are unable to determine in which nucleus the peak is harboured since neither is resolved by CFHT; they are blended together.

3.3.4 Flux matching

Photometry was performed for each epoch in all three filters. Adopting a flux annulus with $R_{inner} = 2.4$ arcsec and $R_{outer} = 3.0$ arcsec, and a sky annulus ranging between

5.4 arcsec $< R <$ 8.4 arcsec, fluxes were scaled and subtracted for the 1.5 arcsec aperture. Notice the light reaches maximum and levels off at approximately $r_{ap} = 1.5$ arcsec (figure 3.17), justifying our choice in nuclear aperture size for both this method and the differential photometry of section 3.2.

We are ultimately interested in the absolute magnitude of the variable flux peak at epoch #6. Now that the flux between instruments has been matched and the NICMOS background subtracted off, is it possible this peak could be a supernova? To answer, the absolute magnitude of the peak must be known. This requires external knowledge of the brightness of the Arp 220 nuclei. For this we use photometry performed on the NICMOS archival images by Scoville et al. (1998), which includes apparent magnitudes of each nuclear component and the nuclear system as a whole (see table 3.1 for these measurements, converted to absolute magnitudes).

Component	Aperture	$M_{1.25}$	$M_{1.6}$	$M_{2.2}$
W	$0.92'' \times 0.58''$	-18.97	-20.27	-21.33
S	$0.40'' \times 0.40''$	-17.09	-18.28	-19.21
SE	$0.40'' \times 0.40''$	-16.69	-18.06	-19.54
NE	$0.55'' \times 0.55''$	-17.80	-19.10	-20.23
All	$5''$ circular	-21.29	-22.42	-23.24

Table 3.1: *NICMOS photometry performed on Arp 220 nuclear components (Scoville et al., 1998). Magnitudes are quoted as absolute, corrected from apparent magnitudes using the distance modulus. Note these values as observed are not extinction-corrected. The subscript in each magnitude represents the central wavelength of the observation in μm. The size of the aperture covering all sources is given as a diameter.*

Recall that WIRCam cannot resolve the separate nuclear components of Arp 220. As such the best choice for comparison is the measurement covering all nuclei, using an aperture radius of $R_{ap} = 2.5$ arcsec. The flux scaling procedure was applied to the NICMOS images using this new aperture. To convert from arbitrary flux units to physical absolute magnitudes, the reference magnitude from table 3.1 was used along with the corresponding flux contained within this aperture, and relation (2.1)

was applied. The results for the peak fluxes on epoch #6 are as follows:

$$\begin{aligned} M_K &= -22.19 \pm 0.16 \\ M_H &= -20.18 \pm 0.23 \\ M_J &= -18.30 \pm 0.46. \end{aligned} \tag{3.13}$$

The K-magnitude is already quite large for a core collapse supernova (typically $M_K \simeq -18.6$) (Matilla & Meikle, 2001); the magnitude will be brightened even further when extinction is factored in.

3.4 Summary

In this chapter we described a variety of methods utilized to detect supernovae in Arp 220 data from WIRCam. A visual search revealed no SNe in the circumnuclear regions of the galaxy, however the bright nucleus prevents the detection of nuclear SNe. No transients were found after PSF matching and image subtraction; a consistent region of residuals spanning up to roughly three arcsec in diameter still obscures any potential SNe in the core of Arp 220. We extracted nuclear light curves using differential photometry with reference stars in the Arp 220 field which showed evidence for variations in nuclear brightness. In particular we isolated a peak in flux on the sixth epoch of observation, with a growth curve resembling a point source in nature. Due to its strong brightness ($M_K \simeq -22$), it is very unlikely this peak is a single supernova event; to determine this we first need to gain a better understanding of the extinction in Arp 220. We directly estimate this quantity in the next chapter.

Chapter 4

Nuclear Extinction in Arp 220

Extinction refers to the attenuation of radiation due to the presence of intervening material between the observer and the source. The main culprit responsible for extinction is interstellar dust which originates primarily from stellar winds and supernova ejecta. Extinction encompasses two effects: absorption, in which grains of dust absorb light and re-emit at different wavelengths (primarily in the infrared), and scattering, in which photons are redirected out of (and into) the line of sight. Shorter wavelength photons are preferentially scattered more than those of longer wavelength, an effect referred to as reddening. Thus light which has suffered extinction appears redder than it actually is, a phenomenon seen in Earth's atmosphere during sunrise and sunset when blue photons are scattered out of the line of sight to the Sun and we observe a reddened sky.

The extinction in magnitudes in a waveband λ is defined as

$$A_\lambda = -2.5 \log \left(\frac{f_\lambda}{f_{\lambda_o}} \right) \tag{4.1}$$

where f_λ represents the measured flux and f_{λ_o} the intrinsic, un-attenuated flux from a source. In order to determine the absolute magnitude M_λ of a source at a distance d parsecs with measured apparent magnitude m_λ, the extinction must be subtracted via

$$M_\lambda = m_\lambda - 5 \log(d) + 5 - A_\lambda. \tag{4.2}$$

ULIRGs contain atypically high amounts of dust due to the rapidity and strength of the merger-induced starburst. Contained in a much smaller volume, the dust has a significantly higher density than in quiescent galaxies resulting in a greater opacity.

Further, the more intense the starburst, the more mass is lost in stellar winds and supernova ejecta from massive stars; both are sources of dust production. As a result such galaxies are observed to exhibit significant extinction. In the optical for instance (see figure 1.3) the entire nuclear region of Arp 220 is obscured. Understanding the degree of extinction in Arp 220 is important in determining the intrinsic brightness of its components as well as piecing together the morphology, specifically the dust structure, of its nuclei.

The flux comparison analysis described in chapter 3 analyzed the nuclear region of Arp 220. Using the obtained absolute but absorbed magnitudes of the peak observing epoch, and assuming that it represents a core collapse event, it is possible to place limits on the total extinction in this region of the galaxy.

Section 4.1 describes the two reddening laws utilized in this calculation. We outline our chi-square minimization based estimation procedure in section 4.2 and derive uncertainties in the extinction in section 4.3. Finally we explore the sensitivity of our observations to supernovae in the nuclei in section 4.4.

4.1 Extinction Curves

The extinction in a specific filter can be related to that in another (typically using the V band as a reference) to form an extinction curve. A variety of studies have been undertaken to determine the form Galactic extinction takes in the infrared. Two in particular are used here to place upper and lower limits on the amount of extinction in the K-band in Arp 220.

We use the Galactic extinction laws of Rieke & Lebofsky (1985) and Fitzpatrick & Massa (2009) (hereafter RL and FM respectively) to model the extinction. The former derive the extinction law using sightlines toward both the Galactic centre and Scorpius from 1 to 13 μm whereas the latter examine extinction curves to 14 different O and B stars, and show that a power law of the form $A_\lambda \propto \lambda^\beta$ with $\beta = -1.84$ fits most sight lines well. Though FM advise against a universal beta value for the Galactic extinction law, we adopt a single value. The large uncertainties in extragalactic extinction laws justifies this choice. The resulting extinction relations in J and H relative to K are

$$\begin{aligned} A_J &= 2.518 A_K, \;\; A_H = 1.563 A_K \\ A_J &= 2.695 A_K, \;\; A_H = 1.657 A_K \end{aligned} \tag{4.3}$$

from RL and FM, respectively. It is apparent that extinction is significantly greater in the J-band than in K, however still far less when compared with the optical where $A_V = 8.9A_K$ (RL). Using both laws will allow for an upper and lower limit to be placed on the amount of absorption.

4.2 Chi-square minimization

We first determined theoretical (expected) values for the J and H magnitudes of the variable peak luminosity using the observed K absolute magnitude as an anchor and correcting for the magnitudes in the remaining filters using the colours of a typical core collapse SN at peak. This is done under the assumptions that the event at epoch #6 was indeed a single core collapse supernova, and reached the peak on this night. As mentioned in chapter 3, the shape of the K-band light curve from differential photometry supports this notion of a supernova event. Matilla & Meikle (2001) compile near-infrared photometric data of 13 core collapse supernovae to create templates of core collapse light curves in J, H, K and L. They subdivide their light curves into two separate supernova classes: ordinary and slow-declining. The former are characterized by a post-peak linear decline in brightness for approximately 200 days, whereas the latter plateau in almost every filter after 100 days. Further, slow-decliners display brighter peaks. Since only two of their total sample of 13 supernovae were assigned to the slow-declining class, we assumed the Arp 220 event was an ordinary supernova and used the appropriate colours which are derived from the peak brightness of the template. Even if this "supernova" was not caught during its peak (see table 2.2 for intervals between observation epochs), the near-IR template light curves in J, H and K (see fig. #1 in Matilla & Meikle, 2001) show very similar slopes both preceeding and following peak brightness; therefore the colours would remain nearly the same (see subsection 4.3.2 for a more detailed discussion of the colours employed). The resultant colours are

$$\begin{aligned} J - K &= 0.2 \\ H - K &= 0. \end{aligned} \tag{4.4}$$

Let us now attempt to derive the expected absolute magnitude in the J and H bands based on the observed magnitude in the K band, M_K^{obs}. For a given amount of

extinction A_K, the true extinction-corrected absolute magnitude M_K is given by

$$M_K = M_K^{obs} - A_K. \tag{4.5}$$

If there were no extinction present in the J or H filters, the brightness that would be observed is that given by applying the colour corrections of (4.4) to M_K. To take extinction into account in J and H, an extinction law from (4.3) is adopted and applied to the colour-corrected magnitudes:

$$M_\lambda^{corr} = M_K + C + A_\lambda \tag{4.6}$$

where C is the appropriate colour correction. M_λ^{corr} is therefore the expected magnitude based on a given value of A_K.

We now return to the determination of the extinction that best fits the data. We want to maximize the likelihood that a given absorption will produce the observed magnitudes. Maximizing the probability is equivalent to minimizing the chi-square value for differing amounts of A_K. The absorption in K was incremented from $A_K = 0 - 10$ in small step sizes and the value of chi-square was calculated in each step via

$$\chi^2 = \sum_{\lambda=J,H} \left(\frac{M_\lambda^{corr} - M_\lambda^{obs}}{\sigma_\lambda} \right)^2. \tag{4.7}$$

The uncertainty σ_λ is the error in each magnitude measurement, propagated through from initial photometry. Note that while only two measurements are involved in equation (4.7), this is a chi-square problem with three degrees of freedom due to the use of the K-band measurement as a baseline. The minimum chi-square value was then found, corresponding to the most likely value of the absorption. See figures 4.1 and 4.2 for the resulting chi-square distributions.

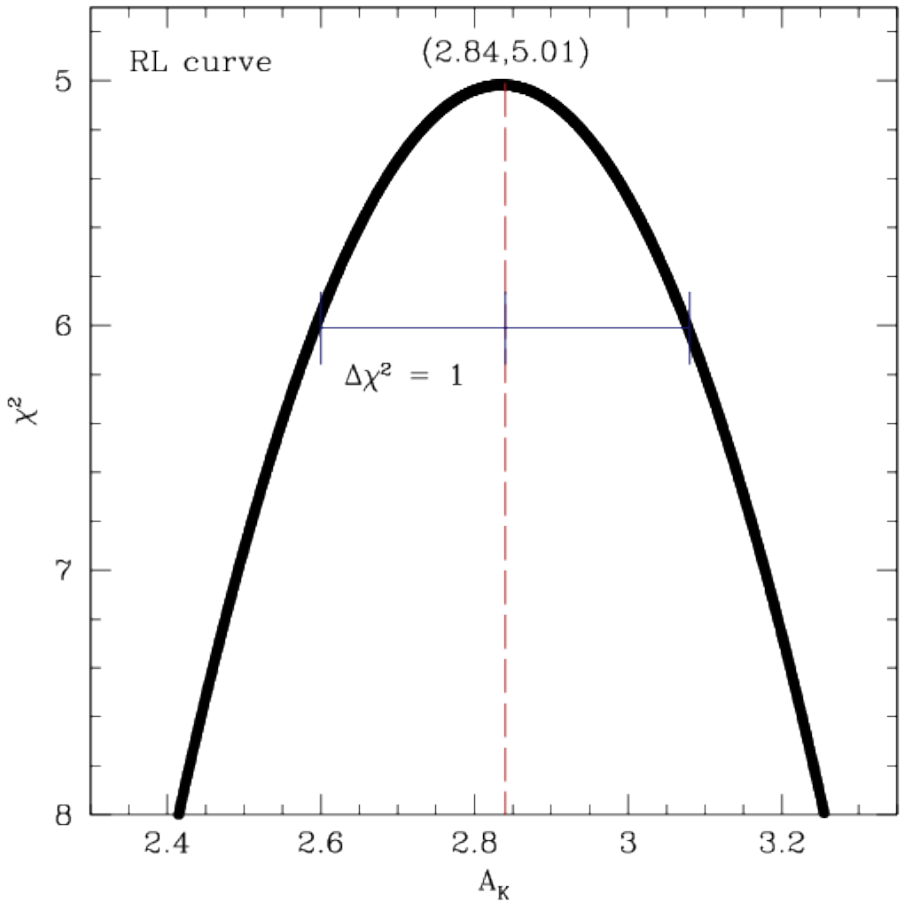

Figure 4.1: *Chi-square distribution as a function of K-band extinction using the Rieke & Lebofsky (1985) extinction law as described in the text. Note that the y-axis is inverted to emphasize the minimum of the distribution corresponding to the maximum probability. The peak coordinate is labeled on the plot. The horizontal line from the centre of the peak to the curve represents the change in A_K resulting in a difference in chi-square of one (see section 4.3).*

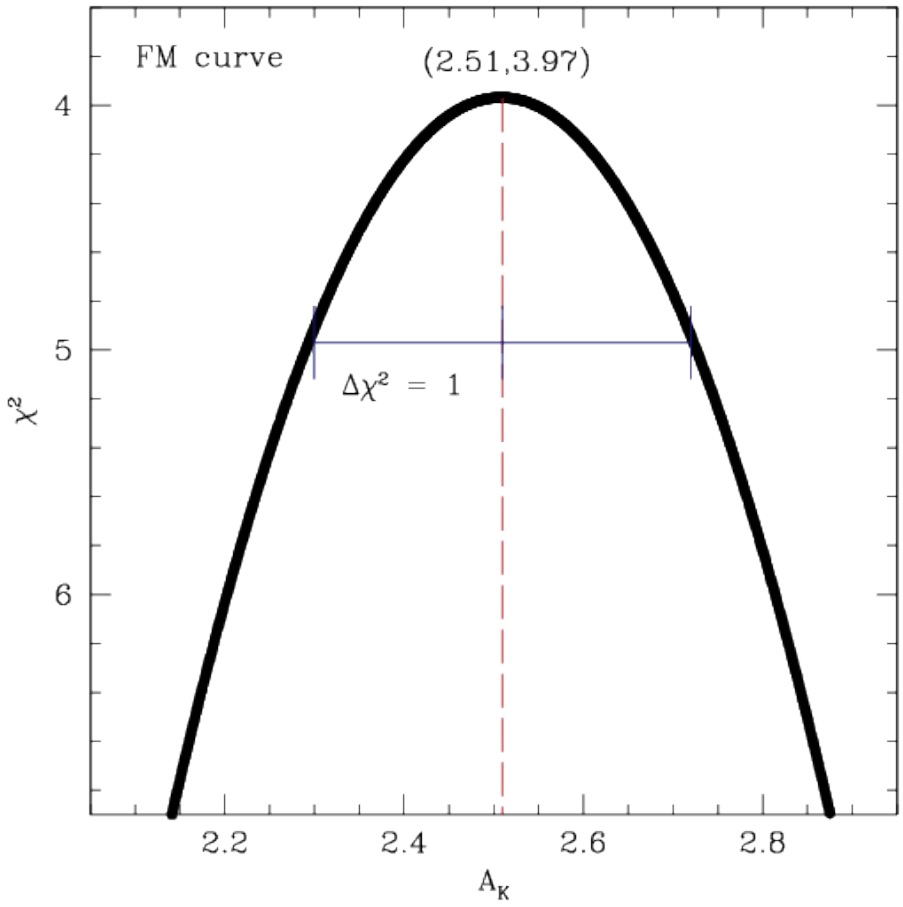

Figure 4.2: *Chi-square distribution using the Fitzpatrick & Massa (2009) extinction law.*

4.3 Uncertainties

From the previous section it is apparent that a value of $A_K \simeq 3$ minimizes χ^2. In order to gain a better understanding, it is vital to assess the uncertainty in this estimate, which ultimately stems from the uncertainties in the observed magnitudes as well as the assumption in intrinsic colour. Peak brightness uncertainties translate to a characteristic spread in the chi-square distribution, apparent in figures 4.1 and 4.2.

To determine the uncertainty in the estimated parameter A_K, consider changing

the chi-square minimized parameter by some amount ϵ such that

$$\chi^2\left(A_K^{\chi^2_{min}}+\epsilon\right)=\chi^2\left(A_K^{\chi^2_{min}}\right)+1 \tag{4.8}$$

in which $A_K^{\chi^2_{min}}$ is the value of absorption which minimizes chi-square and $\epsilon=\left|A_K-A_K^{\chi^2_{min}}\right|$. In other words, one must find the perturbation to the determined parameter A_K such that $\Delta\chi^2=1$. The change ϵ is simply the variance of the extinction ($\sigma^2_{A_K}=\epsilon$), thus the standard deviation is determined via

$$\sigma_{A_K}=\sqrt{\epsilon}. \tag{4.9}$$

The absorption code was modified to find the error using both wings of the distribution. Since step sizes in A_K were finite, this was done by searching for values of chi-squared (and associated A_K) that lay between

$$\chi^2\left(A_K^{\chi^2_{min}}\right)+0.995\leq\chi^2\left(A_K\right)\leq\chi^2\left(A_K^{\chi^2_{min}}\right)+1.005. \tag{4.10}$$

In other words, the difference in chi-squared was bounded by

$$0.995\leq\chi^2\left(A_K\right)-\chi^2\left(A_K^{\chi^2_{min}}\right)\leq 1.005. \tag{4.11}$$

The resulting absorption estimates and uncertainties are

$$\begin{aligned} A_K &= 2.84\pm 0.49 \\ A_K &= 2.51\pm 0.46 \end{aligned} \tag{4.12}$$

using the RL and FM extinction curves respectively. V-band extinction was determined using the RL relation

$$\frac{A_K}{A_V}=0.112. \tag{4.13}$$

Therefore the full (1-σ) range of extinction is

$$\begin{aligned} 2.05 &\leq A_K \leq 3.33 \\ 18.30 &\leq A_V \leq 29.73. \end{aligned} \tag{4.14}$$

The magnitude uncertainty can be estimated alternatively by considering the following. In an ideal world, $\chi^2_{\nu,min}\simeq 1$, corresponding to a situation in which the

difference between theory and observation is close to the uncertainty; in this case with $\nu = 3$ we expect $\chi^2_{min} \simeq 3$. Examining the peaks in figures 4.1 and 4.2 it is clear that $\chi^2_{min} \gtrsim 3$. By what factor do the errors have to be increased such that $\chi^2_{min} = 3$ exactly?

Using the values of $A_K^{\chi^2_{min}}$ for each extinction curve, we determined the scale factor that produced $\chi^2_{min} = 1$ and scaled our magnitude errors. This factor was found to be less than 1.5 times our initial uncertainties. The same analysis as above was repeated to calculate the error, namely finding the value of A_K such that $\Delta\chi^2 = 1$.

The resulting absorption estimates and uncertainties are

$$\begin{aligned} A_K &= 2.84 \pm 0.56 \\ A_K &= 2.51 \pm 0.50 \end{aligned} \tag{4.15}$$

in the RL and FM extinction curves respectively. Therefore the range of extinction (1-σ) from this method is

$$\begin{aligned} 2.01 \leq A_K \leq 3.40 \\ 17.95 \leq A_V \leq 30.36. \end{aligned} \tag{4.16}$$

Though the estimates are quite close, the true uncertainty will lie between that determined from this and the previous method.

4.3.1 Literature Comparison

As mentioned in the introduction, via integral field spectroscopy Engel et al. (2011) conclude that in the K-band they observe only $\sim 7\%$ of the total emitted stellar light in the nuclei of Arp 220. Using the definition of total extinction (relation 4.1) results in an extinction in K of $A_K \simeq 2.89$, which lies well within the range determined using WIRCAM and NICMOS data, showing good agreement between widely differing observational methods.

Matilla & Meikle (2001) simulate a supernova search in the nuclear regions of starburst galaxies and find typical extinction values of $A_K = 2 - 4$. Using mid-IR line ratios, Genzel et al. (1998) find $A_V = 45$ in the nucleus of Arp 220 corresponding to $A_K = 5$, even higher than we find. Furthermore, in their NICMOS search for SNe in starburst galaxies, Cresci et al. (2007) state the most probable cause for their non-detection is high extinction in the galactic nuclei. They determine that $A_V > 11$

is necessary to explain the results when using the limiting magnitude of the nuclear regions, and $A_V > 25$ when using the limiting magnitude of the outer galactic regions.

Our determination of the extinction in the nuclei of Arp 220 fits well with most estimates and is even an underestimate compared to some.

4.3.2 Colours

Adopting roughly three magnitudes of extinction in the K-band, the brightening event on epoch #6 has an absolute magnitude of approximately $M \simeq -25$, significantly brighter than a typical core collapse or even type Ia SN. Yet we estimated the extinction by assuming the near-IR colours of a typical core collapse SN at peak luminosity. Is this assumption reasonable, even if this event was not a core collapse supernova?

What do we know about this brightening event? From differential photometry it is a clear peak in the data that, based on the preceding analysis in this chapter, is affected by extinction in the appropriate way; its luminosity increases with observed wavelength. The magnitude system we appropriate uses Vega as a reference star. Stars can, to first order, be modeled as blackbody emitters. If we assume our event also emits like a blackbody (a reasonable assumption for a SN), we can compare it to Vega.

Vega is an A0V star with effective surface temperature of $T \simeq 10,000K$ (Yoon et al., 2010). Being the reference of the magnitude system, all of its colours are automatically set to zero. We can model the intensity of a blackbody at this temperature using the Planck curve:

$$I(\lambda) = \frac{2hc^2}{\lambda^5} \frac{1}{e^{\frac{hc}{\lambda kT}} - 1} \tag{4.17}$$

in which h is Planck's constant, c the speed of light, λ the wavelength, k Boltzmann's constant and T the temperature. From Wien's displacement law ($\lambda_{max}T = C$ in which $C = 2.90 \times 10^{-3} mK$ is a constant), a 10,000 K blackbody peaks in emission at 0.29 μm. Figure 4.3 shows the Planck curve for three different temperatures that are typical for stellar surfaces. The temperature of the expanding shell of a supernova is also of order 10^4 K (Salvaterra et al., 2004). Since we observed with WIRCam in the near-infrared (J-band at $\sim 1.2\mu$m to K at $\sim 2.2\mu$m), this wavelength range is clearly in the region beyond the peak of each distribution and in the Rayleigh-Jeans limit of the spectrum (where $\lambda >> hc/kT$). In this limit, the intensity becomes $I = 2ckT/\lambda^4$, a power-law in which $I \propto \lambda^{-4}$. Even at lower temperatures the near-IR is clearly in

the Rayleigh-Jeans regime, which has identical behaviour. Therefore we would expect that even if the temperature of the epoch #6 event was less (or greater) than 10,000 K, its near-IR colours would be very close to zero. One can also verify that stars with a wide range in temperature between roughly ($8000K < T < 25000K$) have near-IR colours of nearly zero (Tokunaga, 2000). Consequently even if this event was not a core-collapse SN, our choice in colours is reasonable for the purposes of estimating extinction. It is also interesting to note that for a stellar population less than 10 Myr old, the colours are nearly identical to those we employ: $J - K = 0$, $H - K = 0$ (Scoville et al., 1998).

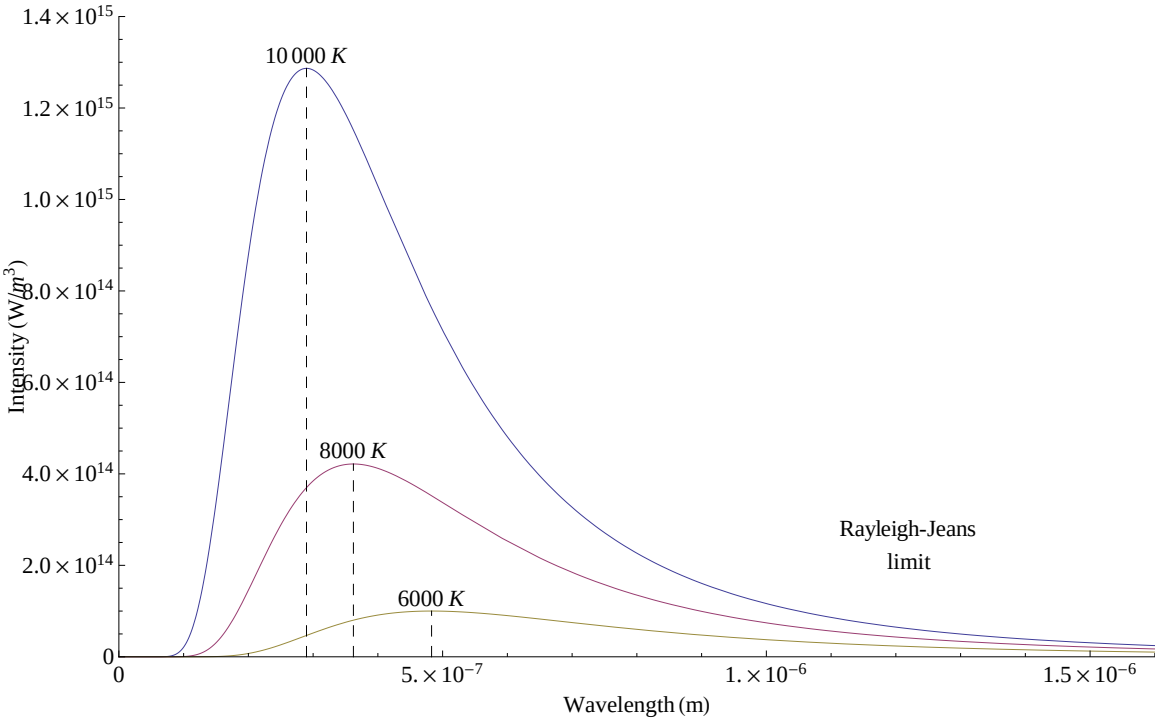

Figure 4.3: *Blackbody intensity profiles for three different temperatures. Our Sun can be approximated by the 6000 K curve. The Rayleigh-Jeans limit is labelled. Note how, as described in the text, the behaviour of the emission in this region is nearly identical for each curve.*

4.4 Sensitivity to Supernovae

Based on the above analysis it is clear that the peak seen on epoch #6 has a brightness several magnitudes brighter than that of a typical core collapse supernova. If a

supernova had gone off throughout the observations, would we have been able to detect it? In other words how sensitive are our observations to detecting SNe? To answer this question, we consider two regions of Arp 220 separately: interior and exterior to the nuclei.

4.4.1 Limiting Magnitudes

Any astronomical instrument will have a limit to the brightness of an object it is capable of detecting. Further, the apparent brightness at which photometry can be effectively performed will often be even brighter than this. We refer to this as the limiting magnitude of the observation.

There are two general methods for determining the limiting magnitude. One can locate the faintest visible stars in an image and look up their apparent magnitudes in a stellar catalog. Alternatively, one can measure the noise in the relevant section of the data to then estimate a magnitude. For the sake of thoroughness we use a combination of the two to find the limiting magnitude outside the nuclear region.

An examination of Arp 220 HST data reveals many visible star clusters, several of which are also apparent in WIRCam data (see figures 1.4 and 2.1). Both the brightness of these objects and the distance of Arp 220 eliminates the possibility of them being singular stars. NICMOS detected eight circumnuclear clusters in total (all unresolved) and photometry was performed by Scoville et al. (1998). The spread in absolute magnitudes of these clusters show the following range:

$$\begin{aligned} -14.22 \leq M_J \leq -11.85 \\ -15.03 \leq M_H \leq -12.66 \\ -15.25 \leq M_K \leq -13.67. \end{aligned} \tag{4.18}$$

Of note is the brightest cluster located 1.5" west and 4.8" south of the centre of the nuclei (see figure 4.4); its absolute magnitude is represented by the brightest values in (4.18). The cluster is quite prominent in WIRCam images, and is several magnitudes fainter than a core collapse supernova (see table 1.1), even with a generous 2 magnitudes of extinction. The lack of intervening dust in the circumnuclear regions when compared to the nuclei implies that extinction will be even less substantial outside the galactic centre. Thus it is clear a regular core collapse supernova would be readily detectable external to the nuclei.

For the purposes of comparison we now quantify the limiting magnitude using

image statistics. We begin with the definition of the signal-to-noise ratio, which represents the amount of desired signal obtained relative to the background noise present. Mathematically we can represent this ratio via

$$\frac{S}{N} = \frac{I \times t}{\sqrt{\pi r_o^2 \sigma}} \tag{4.19}$$

in which S is the signal, N the noise, I the intensity per second in adu, t the exposure time in seconds, r_o the PSF FWHM in pixels and σ the sky noise in adu. We subdivide Arp 220 into four rectangular regions that surround the central area of the galaxy which we take to be a square region $12'' \times 12''$ in size. We then measure the noise in each region using IRAF's *imstat* algorithm which calculates the mean and standard deviation (noise) in a specified area. We repeat this for all observing epochs and find the mean noise in all four regions. See figure 4.4 for a visual representation of the method.

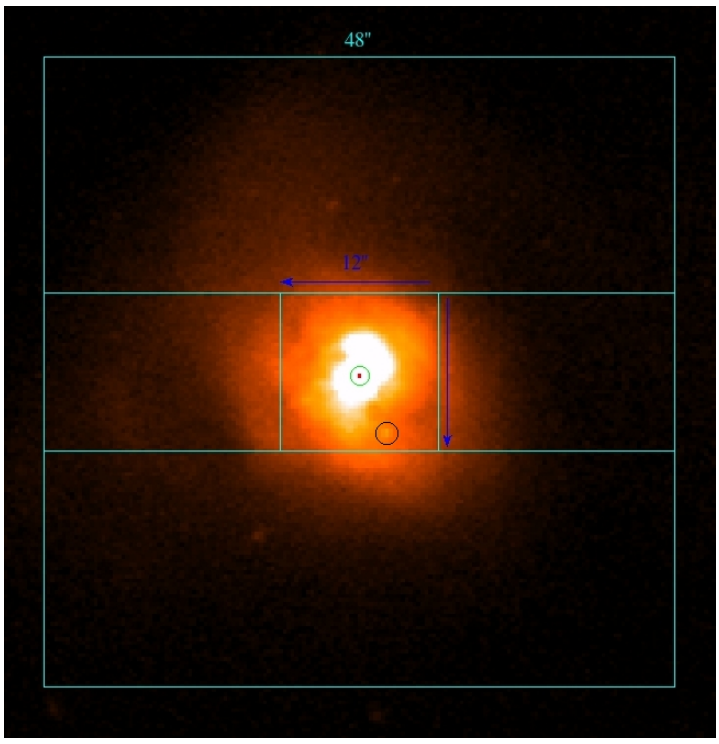

Figure 4.4: *Method used to extract noise values in Arp 220 in the J band, isolating the nuclear region. The red dot denotes the centre of the nuclei and the green circle is the aperture used by Scoville et al. (1998) to encompass all nuclei. The black ellipse outlines the brightest cluster as mentioned in the text. The entire region analyzed is a square with side 48 arcseconds.*

We adopt a value of $r_o = 2.3$ pixels (0.7 arcsec) as the mean FWHM in each filter and assume a signal-to-noise of 10. We then calculate the intensity per second using (4.19) and the exposure times listed in table 2.1. Once the intensity is known, we calculate the limiting magnitude via

$$m = -2.5\log(I) + ZP \tag{4.20}$$

in which ZP is the zero-point of the observation. Recall the zero-point is normalized to one second of exposure time, consistent with the intensity per second that we solve for in (4.19). While the zero-point differs between observing runs, the changes are slight and we adopt representative values shown in table 2.4.

Resulting apparent magnitudes are then converted to absolute magnitudes using the distance modulus of Arp 220. The results are outlined in table 4.1.

Filter	M_{lim}
J	-16.1
H	-16.7
Ks	-17.1

Table 4.1: *Limiting absolute magnitudes of WIRCam observations of stars estimated as described in the text for a S/N of 10.*

Compared with the brightest cluster in (4.18), these values are close to 2 magnitudes brighter. Using real noise data from the images, the latter values more closely represent magnitudes at which photometry can be accurately performed, while the former values can be thought of as a lower limit for the brightness at which an object will be visible in the data. Furthermore, we have assumed a signal-to-noise of 10; smaller values would increase the limiting magnitude (i.e. we would be able to detect fainter objects at lower signal-to-noise). Nevertheless it is still apparent that a supernova would be visible outside the nuclear regions of the galaxy. Now we consider sensitivity to SNe in the nuclei.

4.4.2 Nuclear Sensitivity

If a supernova had gone off in the core regions of Arp 220, would we have been able to detect it with WIRCam photometry? We can answer this by calculating the photometric threshold of detection for a single core collapse SN in the nuclear regions

of Arp 220.

Using regular core collapse absolute peak magnitudes from table 1.1 and the absolute magnitudes of Arp 220 nuclear components (table 3.1) coupled with equation (2.2), we determine the fraction of nuclear flux that a single supernova event would comprise. In other words we calculate the brightness of a SN relative to the nuclei to determine the visibility of a SN in our data through photometry. We do this relative to both the western (and brightest) nucleus as well as the entire nuclear region (5 arcsec aperture).

Remember that the nuclear magnitudes of table 3.1 include extinction; thus for the purposes of comparison, theoretical supernova peak magnitudes must also be dimmed for extinction. We assume a modest 2 magnitudes of extinction in the K-band, $A_K = 2$, and adopt extinction relations from the average of Rieke & Lebofsky (1985) and Fitzpatrick & Massa (2009) values:

$$\begin{aligned} A_H &= 1.6 A_K \\ A_J &= 2.6 A_K \end{aligned} \tag{4.21}$$

which yield $A_H = 3.2$ and $A_J = 5.2$. An examination of nuclear magnitudes (table 3.1) reveals an interesting effect: as we proceed from higher to lower wavelengths, the brightness of nuclear components decreases. Extinction undoubtedly plays a role in this flux decrease; however other factors may contribute such as intrinsic reduced emissivity of the starburst or AGN at lower wavelengths. In a similar manner core collapse SN peak brightnesses also show an inverse relation to filter central wavelength due to extinction. Thus we have two competing effects: as we move from K to J, the nuclei become fainter, but so too do the supernovae. If the nuclei reduce in brightness more rapidly with decreasing wavelength than the expected SN maximum, it might be easier to detect a SN at a lower wavelength. Which effect dominates? The answer will illuminate the filter in which a supernova would be most readily visible.

Results for the fraction of total flux that core collapse events (both regular and slow-decliners) would represent are outlined in table 4.2. We also include values for type Ia SNe (typical absolute magnitudes taken from Wood-Vasey et al., 2008 and Jack et al., 2012) along with the most superluminous type IIn ($M_u \sim -22$; see Chornock et al., 2013).

Nuclear Component	Filter	core collapse (regular) f/f_o	core collapse (slow) f/f_o	type Ia f/f_o	type IIn f/f_o
West	J	0.005	0.020	0.005	0.136
	H	0.011	0.041	0.006	0.258
	K	0.013	0.047	0.009	0.294
All	J	0.001	0.002	0.001	0.016
	H	0.002	0.005	0.001	0.036
	K	0.002	0.008	0.002	0.051

Table 4.2: *Photometric sensitivity to various types of individual SNe in the nucleus of Arp 220. f/f_o is the fraction of nuclear flux a SN would comprise at peak luminosity. Two nuclear components are considered: the western nucleus and the entire central region as defined by Scoville et al. (1998).*

Clearly the diminishing SN flux due to extinction dominates the drop in nuclear flux, resulting in a maximum possibility of detection in the K-band. Further note how minimal a fraction of the nuclear light a regular core collapse SN would consist-at peak detectability, only 1.3% of the western nucleus. Recall from chapters 3 and 4 that photometry was performed using aperture sizes of $R_{ap} = 1.5$ and 2.1 arcsec which lies in between the aperture sizes utilized by Scoville et al. (1998) for the western nucleus and all components (table 3.1). Thus the detectability in our aperture will lie someplace between the two values found in the west and for all nuclear sources. A comparison with differential photometry (figures 3.5, 3.7, 3.9) reveals that the average error bars in each measurement are approximately 0.02 magnitudes in width. Equation (2.2) shows this to correspond to $f/f_o = 0.02$; that is, our error bars are larger in flux than a regular core collapse (or type Ia) supernova, and even if we could photometrically isolate the western nucleus alone in the K-band we would be unable to detect a single event. The nuclei are so bright they outshine almost any potential SNe. The only event we are capable of detecting at the multiple-sigma level is an extremely superluminous type IIn SN; these events are extremely rare and the absorption corrected absolute K-magnitude we find is two magnitudes brighter than the most luminous SN observed to date.

This leads credence to the hypothesis that we are actually observing short-term fluctuations in nuclear light due to AGN activity, which can vary on a variety of timescales. In contrast, the nuclear variations may owe their origin to multiple SNe

occurring in the nuclei, the light curves of which add together. The latter possibility is more likely if the SN rate in Arp 220 has been underestimated which would allow for multiple SNe to occur in short time intervals.

In this chapter we used the brightening event of epoch #6 to estimate the degree of extinction present in the nuclear regions of Arp 220. We further explored the sensitivity of WIRCam observations to supernovae by estimating the limiting magnitude of our observations. In the galactic centre we are not sensitive to individual core collapse SNe, though the presence of multiple superposed SN light curves is not ruled out.

Chapter 5

Type Ia Supernovae in Old Galaxies from Young Bursts

5.1 Introduction

Galaxies are broadly classified as elliptical, spiral and irregular, a scheme first introduced by Edwin Hubble (Hubble, 1936). Though Hubble assigned such designations based on observed morphology, it was later discovered that galaxy morphology is correlated with the stellar populations residing within. In general spiral galaxies contain a blue component and still exhibit star formation whereas ellipticals are significantly more red, devoid of gas and have ceased forming stars. One quantifiable way to distinguish galaxies is through the galaxy colour-magnitude diagram, the galactic equivalent of the observational Hertzsprung-Russell stellar diagram. Plotting the colour vs. magnitude of a variety of galaxies, three separate regions emerge: the red sequence (RS), blue cloud and the green valley between them; see figure 5.1 for a simple schematic. It is on the red sequence where elliptical galaxies are found, and here that we focus our attention.

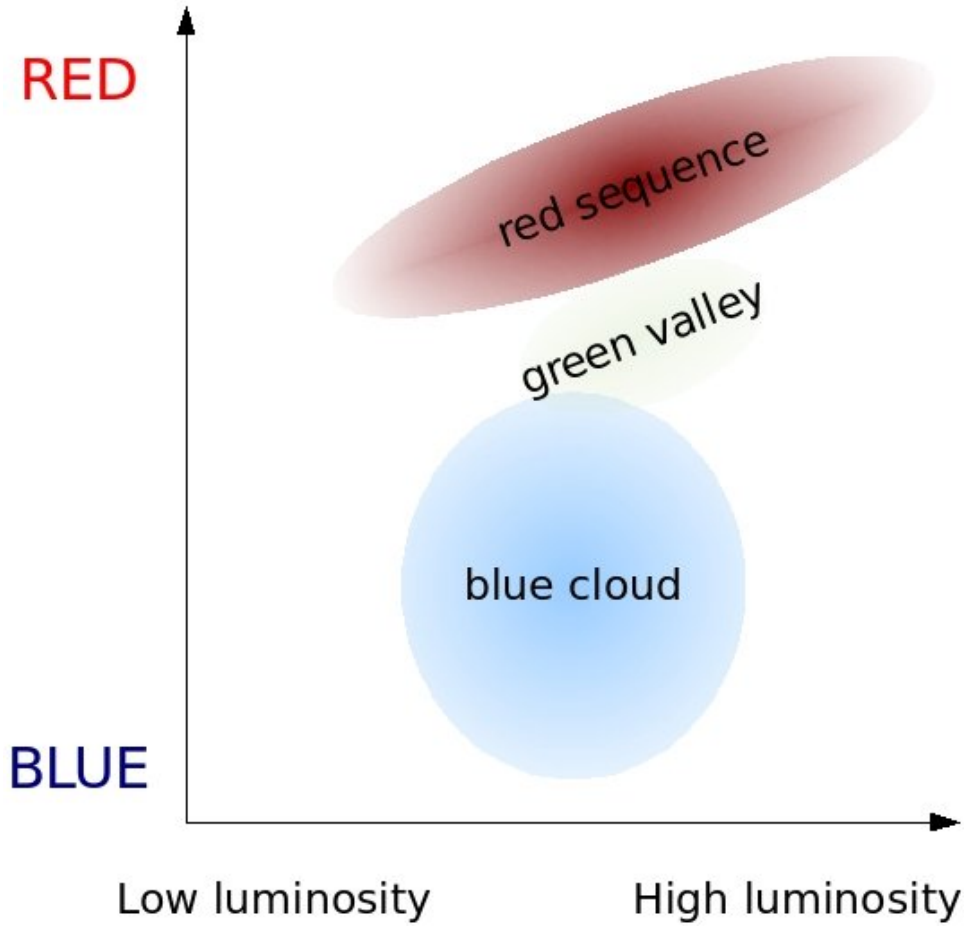

Figure 5.1: *Galaxy colour magnitude diagram schematic. Early-type galaxies (ellipticals, lenticulars) are found on the red sequence whereas late-type galaxies (spirals) are found in the blue cloud. (From Wikipedia.)*

What is the origin of the red sequence? At a given redshift, there is a limit to the maximum age of a galaxy, set by the epoch at which galaxies formed. This is supported by the finding that early type galaxies formed the bulk of their stars between redshifts of $z = 2-3$ in clusters and $z = 1-2$ in less dense environments (i.e. the field); early-type galaxies thus share a common formation epoch (e.g. Thomas et al., 2005). Consequently each cluster will have its own red sequence which is dependent on its redshift. The age of the oldest galaxies determines the colour of the red sequence, and no galaxies redder than the sequence should exist.

The RS is typically represented as a linear relation between the colour and brightness (in magnitudes) of galaxies. It is a general feature of the red sequence that fainter galaxies are more blue in contrast to brighter galaxies. This is likely an effect

due to the mass and metallicity of cluster galaxies; less massive galaxies have more trouble retaining their metals and are consequently metal-poor in relation to more massive galaxies. Metal-poor stars are generally more blue; this trend will also apply to galaxies that have lost much of their metal content. Thus the deviation from a horizontal slope in the RS can be interpreted as a metallicity effect.

Type Ia supernovae represent a vital class of supernovae that have been extensively observed in the Universe. In contrast to core-collapse events, a type Ia SN involves the thermonuclear explosion of one (or multiple) carbon-oxygen (CO) white dwarfs (WDs) at or near the Chandrasekhar mass. Once carbon fusion begins in the stellar core, oxygen fusion initiates shortly after and the core temperature rapidly rises. Normally, a main sequence star would expand to cool and balance the increase in thermal energy, maintaining hydrostatic equilibrium. This is not the case with white dwarfs however, which are supported by electron degeneracy pressure instead of thermal pressure and unable to counterbalance the temperature increase (since degeneracy pressure has no temperature dependence). Consequently a runaway fusion reaction is initiated. Within a period of seconds, a considerable fraction of the carbon and oxygen in the star is fused into heavier elements and the temperature rises to billions of degrees (Röpke & Hillebrandt, 2004). The energy released from nuclear burning unbinds the star resulting in a violent explosion.

Type Ia supernovae have been used with much success as standard candles for measuring distances in the Universe and establishing the widely accepted lambda-CDM model of the expanding cosmos (Riess et al., 1998; Perlmutter et al., 1999). This is largely due to the uniformity in SN Ia maximum brightness, typically $M_V \simeq M_B \simeq -19.3$ with a spread of roughly 0.15 magnitudes after standardization (e.g. Conley et al., 2008; Sullivan et al., 2010). As opposed to type II SNe, type Ia spectra show no hydrogen or helium lines but exhibit a strong ionized silicon feature near maximum light. Though no hydrogen may be released, extremely large amounts of iron are produced in the explosion, to such a degree that the present iron mass fraction in the solar neighbourhood cannot be explained without the inclusion of type Ia SNe in galactic chemical evolution models (Mennekens et al., 2010). This iron owes its origin to the radioactive decay of nickel-56 to cobalt-56 and finally iron-56; it is this decay which is largely responsible for the supernova ejecta energy output at intermediate to late stages after explosion (Hillebrandt & Niemeyer, 2000).

While the explosion mechanism is generally agreed to be the ignition of carbon and oxygen in the core of a white dwarf, there is still a great deal of uncertainty

with regards to the exact progenitor system(s) which lead to a type Ia event. Two separate models have long been considered, both requiring a binary star system. The single degenerate (SD) scenario involves a single white dwarf accreting mass from a main sequence or red giant companion until the primary reaches the Chandrasekhar mass (see e.g. Whelan & Iben, 1973; Nomoto, 1982). On the other hand the double degenerate (DD) channel is characterized by the merger of two white dwarfs, the combined mass of which reaches or exceeds the Chandrasekhar mass (e.g. Iben & Tutukov, 1984; Webbink, 1984). The orbits of the double WD stars decay over time due to gravitational wave radiation until they are within close enough proximity to merge.

An important quantity of interest when studying supernovae in galaxies is the rate at which they occur. Establishing the frequency of both core collapse and type Ia SNe can shed light not only on the star formation history of the Universe, but help to reconstruct the chemical histories of galaxies, ultimately contributing to questions about the origins of life on Earth. Type Ia SN rates are often quantified via the delay-time distribution (DTD): the expected Ia rate of a single-burst of star formation as a function of the age of the burst. The delay-time distribution gives a method to distinguish between various Ia progenitor scenarios, since the shape of the DTD differs based on the supernova formation mechanism. For instance the double degenerate DTD is largely shaped by the timescale of binary orbital decay due to gravitational wave emission, while the single degenerate DTD depends largely on the main sequence lifetime of the companion star (Greggio, 2005). The DTD is often parameterized as a power law, $DTD \propto t^x$ in which t is the time after initial star formation (e.g. Totani et al., 2008). Generally speaking, it is predicted that the DD scenario follows an $x = -1$ power-law, whereas the SD channel is thought to exhibit a steeper decline for old SNe (Greggio, 2005). DTDs have been measured in a variety of environments from low to high redshift and have also been estimated theoretically.

In section 5.2 we introduce the motivation for studying supernovae from younger populations. The stellar population templates we use to form models of elliptical galaxies are described in detail in section 5.3, and we derive type Ia supernova rates for our models in section 5.5. We present our results in section 5.6 and lastly apply the models to observations in section 5.7.

5.2 Motivation

Early studies of red sequence galaxies found in clusters revealed that the bulk of their stars formed at high redshift ($z \simeq 2-3$) in a single-burst and henceforth evolved passively (e.g. Rakos & Schombert, 1995; Barrientos et al., 1996; Stanford et al., 1998; Kelson et al., 2001). As such, cluster early-type galaxies provide an excellent probe of the delay-time-distribution devoid of the complications involved in modelling the star-formation history of a more complex galaxy population. The Multi-Epoch Nearby Cluster Survey (MENeaCS) conducted by Sand et al. (2012) was a CFHT survey aimed at discovering type Ia SNe in 57 low-redshift ($z \simeq 0.1$) galaxy clusters. Over its roughly two year span, 23 Ia SNe were discovered and spectroscopically confirmed, allowing for a determination of both the cluster and early-type galaxy SN Ia rate. In addition 7 type II SNe were detected and verified via spectroscopic follow-up (Graham et al., 2012).

Figure 5.2 from Sand et al. (2012) plots, for each supernova Ia host galaxy, its shift in $g-r$ colour from the red sequence vs. its r magnitude. Initially this plot displayed a strong asymmetry around the red sequence such that nearly all RS hosts lay on the blue side. The tendency of hosts to have colours bluer than the RS was intriguing, suggesting a potential intrinsic connection between type Ia host galaxies. Collections of younger stars are often biased toward bluer colours; hot young stars, modelled via blackbody emission, peak at lower wavelengths in accordance with Wien's displacement law. Consequently it seemed plausible from this figure that elliptical galaxies could contain non-negligible amounts of younger stars from a recent or ongoing starburst; and that these stars might have been responsible for the type Ia SNe. However, on checking the photometry, this effect vanished. We show the revised MENeaCS plot in figure 5.2 in which elliptical hosts are distributed nearly uniformly around the RS.

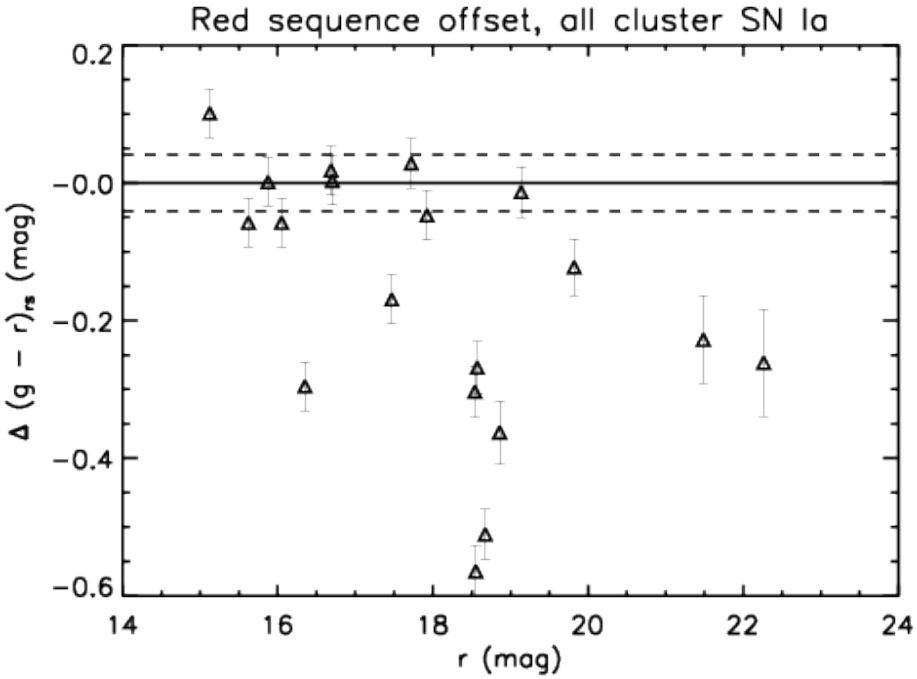

Figure 5.2: *Revised red sequence offset of MENeaCS type Ia SN host galaxies as a function of apparent r magnitude from Sand et al. (2012). The solid horizontal line represents the red sequence with dashed lines showing the mean scatter of the sequence.*

The question still remains, however. Is it possible that some early type galaxies harbour not only an underlying old stellar population but also a younger population due to a more recent starburst which would manifest observationally as a bias of host colours toward the blue? Proposed almost two decades ago from evidence that late-type galaxies seem to produce more type Ia SNe, the hypothesis postulating the presence of younger stars in old elliptical galaxies is not completely unfounded (Della Valle & Livio, 1994). More recently data from the Galaxy Evolution Explorer, Spitzer Space Telescope and HST have revealed that a non-negligible fraction of early type galaxies show a strong infrared and ultraviolet excess along with polycyclic aromatic hydrocarbon emission, all implying low levels of recent or ongoing star formation (e.g. Yi et al., 2005; Young et al., 2009; Salim & Rich, 2010). Other studies using the Sloan Digital Sky Survey have found similar results, such as that of Zhu et al. (2010) who find evidence for low level star formation in field elliptical galaxies with low velocity dispersion. In addition, of the seven type II events detected in MENeaCS,

one was hosted in a red sequence galaxy. This is strong evidence for ongoing star formation in some cluster elliptical galaxies. Even more telling, spectroscopy model fits to early type galaxies typically favour a "frosting" model, consisting of an old underlying population coupled with a smaller frosting of young stars (e.g. Trager et al., 2000; Gebhardt et al., 2003; Schiavon, 2007). Best fits typically find the younger population to represent less than 10% of the total (stellar) galactic mass.

A relation between the mass of elliptical galaxies and their current star formation activity is also found. The star formation history of less massive ellipticals is more extended over time, often even exhibiting some current star formation; above approximately $10^{11} M_{\odot}$, ellipticals are largely passively evolving (e.g. Kodama et al., 2004). It is also found that RS galaxies are more massive than those which lie blueward of the sequence. As such we anticipate a relation between a galaxy's colour relative to the red sequence and the fraction of younger stars present in the galaxy, which can then be correlated to a supernova rate by assuming a specific delay-time distribution.

We know based on the form of the DTD, both theoretical and observational, that the Ia rates in younger populations exceed those in older populations by a substantial amount (e.g. Greggio, 2005). Furthermore, by examining the type Ia rates in various Hubble sequence galaxies, Mannucci et al. (2003) find a rate enhancement in irregulars and late-type galaxies relative to ellipticals. Their results are consistent with the hypothesis that a substantial fraction of type Ia SNe are associated with young stellar populations. If elliptical galaxies therefore house some frosting of a younger population, the detected supernovae may owe their origins to the young population. Is it possible that *all* type Ia SNe in ellipticals come from traces of younger populations? We set out to explore this question in more detail in what follows by exploring the relation between the colours of an elliptical galaxy and the type Ia rate.

5.3 Stellar Population Templates

We model elliptical galaxies using synthetic stellar populations from PEGASE (Fioc & Rocca-Volmerange, 1997). PEGASE models the spectral evolution of galaxies from the ultraviolet through the near-infrared, while being able to account for such effects as nebular emission, galactic winds and extinction. Each template provides the stellar population spectrum at 200 discrete ages from the zero age main sequence to an age of 20 Gyr. We utilize the single-burst template which features an instantaneous burst of star formation at $t = 0$. The mass evolution of the single-burst is displayed in

figure 5.3. Note that the burst is a delta function. As we proceed in time and stars go supernova, the stellar mass declines while the gas mass simultaneously builds. The amount of gas in the galaxy continues to buildup from planetary nebulae and stellar winds, and the white dwarf mass settles at around 10% of the total mass after 10 Gyr. The single-burst scenario uses a RB initial mass function (Rana & Basu, 1992) with stars formed in the mass range ($0.09M_{\odot} \leq M \leq 120M_{\odot}$) and does not include the effects of galactic winds or extinction. Thus the single burst template can be considered the simplest model of a starburst, and will be effective in modelling elliptical galaxies.

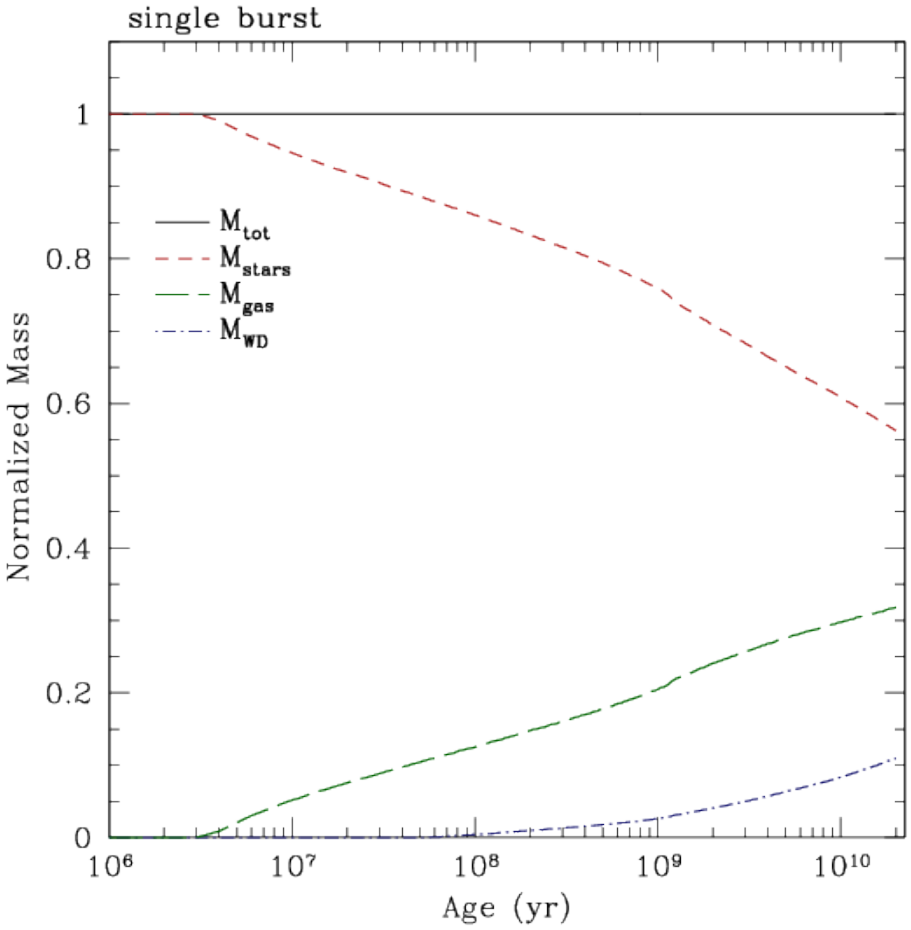

Figure 5.3: *Normalized mass evolution of single-burst template over time. The total mass includes stars + gas. Note the stars are all formed instantaneously and according to an RB initial-mass-function.*

5.3.1 Elliptical galaxy models

To model elliptical galaxies we form composite stellar populations consisting of two single burst components akin to the frosting model. We start with a fixed underlying old population with an age of 10 Gyr (at redshift $z = 0$) and add a younger population, the age and mass of which we can vary.

More specifically, the latter parameter of interest is actually the mass ratio between the young and old population. Seeing as how we are interested in the colours of the resultant composite population, we can show the irrelevance of absolute mass by starting with the (mass) normalized fluxes from PEGASE models. If f_o, M_o and f_y, M_y are the normalized fluxes (in a given waveband) and normalized mass of the old and young population respectively, normalized for 1 $M_\odot$ of material, the total composite flux F_c is given by

$$F_c = M_o f_o + M_y f_y. \tag{5.1}$$

The corresponding magnitude m_c is, in accordance with equation (2.1),

$$\begin{aligned} m_c &= -2.5 \log(M_o f_o + M_y f_y) \\ &= -2.5 \log(M_o) - 2.5 \log\left(f_o + \frac{M_y}{M_o} f_y \right). \end{aligned} \tag{5.2}$$

After a small amount of algebra we can see that the mass separates into its own logarithm. Now we can find the colour $X - Y$, where the superscript denotes the filter,

$$\begin{aligned} X - Y &= m_c^X - m_c^Y \\ &= 2.5 \log\left(f_o^Y + \frac{M_y}{M_o} f_y^Y \right) - 2.5 \log\left(f_o^X + \frac{M_y}{M_o} f_y^X \right) \end{aligned} \tag{5.3}$$

in which it is clear that the absolute mass cancels out and we are left solely with the mass ratio M_y/M_o. Therefore only the relative mass between each population component has an effect on the colour.

Figures 5.4 and 5.5 show two sample spectra of individual single-burst populations, one young (100 Myr) and the other our underlying population (10022 Myr). The full-width-half-maxima of Sloan Digital Sky Survey optical u,g,r,i,z filters (data release 7) are shown. As expected, the younger population is significantly bluer than the

older population while also being over an order of magnitude more luminous (for each population having the same mass).

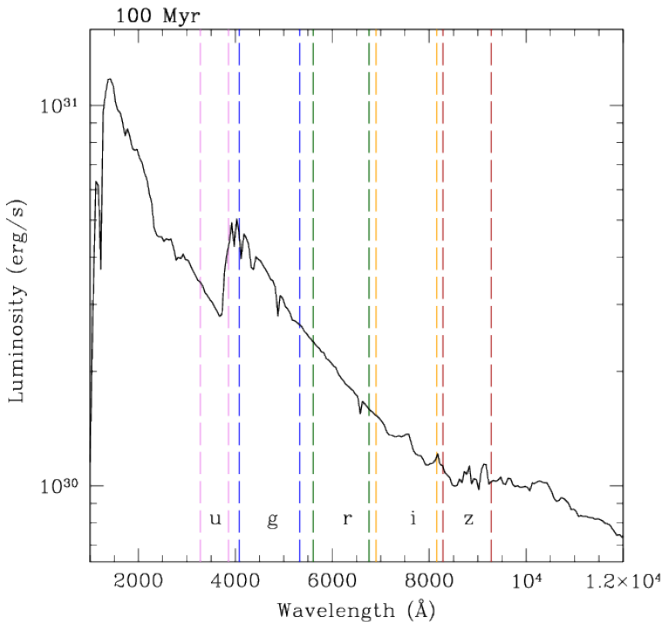

Figure 5.4: *Young single-burst spectrum. SDSS filters are displayed as described in the text.*

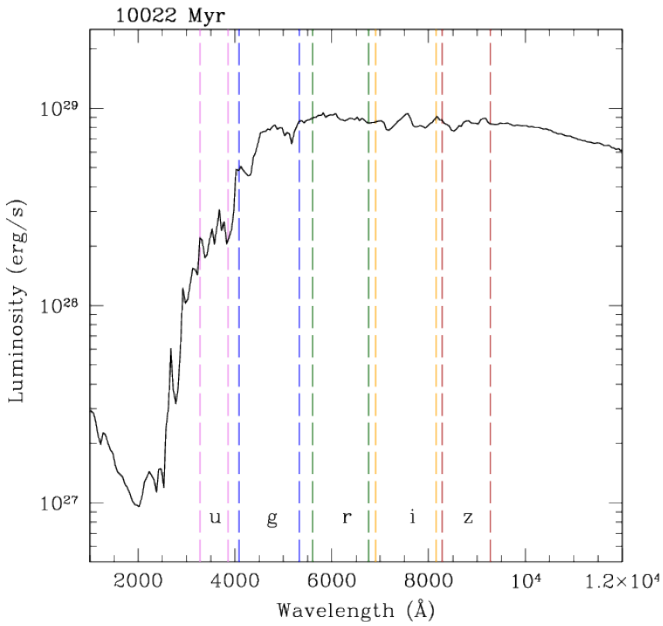

Figure 5.5: *Old single-burst spectrum. Note the decreased luminosity when compared with the 100 Myr burst.*

5.3.2 Redshift

In order to thoroughly explore the effect of younger populations on the overall elliptical supernova rate, we redshift PEGASE templates using the code ZPEG (Le Borgne & Rocca-Volmerange, 2002). ZPEG is a tool which uses PEGASE templates to estimate photometric redshifts based on observational data. To do so, ZPEG redshifts template spectral energy distributions (SEDs) using the k-correction and evolutionary correction and then uses a method of chi-square minimization to find the most probable match to observational data. We make use of the redshifted templates without any need for finding photometric redshifts.

Why are we interested in redshifting our composite populations? As redshift increases, the SED shifts further in wavelength; the ultraviolet part of the spectrum begins to seep into the optical. Since the emissivity of hot young stars is even stronger in the UV compared to the optical, at higher redshift we will be more sensitive to younger populations. In addition to changing the mass ratio and age of the younger

population, it is therefore also important to explore the redshift parameter space.

One complication with examining redshift involves the age of the underlying population in our models. As one goes further back in time (i.e. increasing redshift), it becomes increasingly more rare to find a stellar population 10 Gyr old due to the decreasing age of the Universe. If we maintained a constant background population age with redshift, we would scarcely be able to go beyond $z = 0.3$ at which point the Universe is roughly 10 Gyr old. For redshifts $z > 0.3$, the Universe is simply not old enough to harbour such an old galaxy. Consequently we vary the underlying population age in order to emulate stellar evolution with redshift, starting with an age $t(z)$ of 10022 Myr at $z = 0$ and adjusting according to

$$t(z) = 10022Myr - t_L(z) \tag{5.4}$$

where $t_L(z)$ denotes the lookback time with redshift. Throughout the procedure we adopt canonical cosmological parameters: $H_o = 70$ km/s/Mpc, $\Omega_M = 0.3$, $\Omega_\Lambda = 0.7$ and $w = -1$.

As a preliminary consistency test between PEGASE and ZPEG, we compare the colour of the PEGASE ($z = 0$) templates with ZPEG ($z = 0.01$) templates. At such a small redshift there should be no noticeable shift in colours. We use the elliptical (E) template and u,g,r,i,z prime filter set in order to match filters between the two codes. See figures 5.6 and 5.7; the agreement is excellent and ensures compatibility between ZPEG and PEGASE.

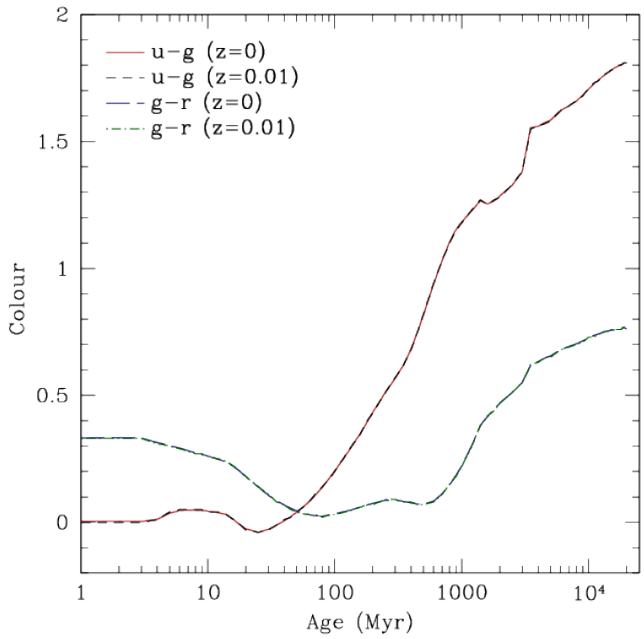

Figure 5.6: *Colour comparison between PEGASE (z=0; solid curves) and ZPEG (z=0.01; dashed curves) for $u' - g'$ and $g' - r'$ as a function of template age.*

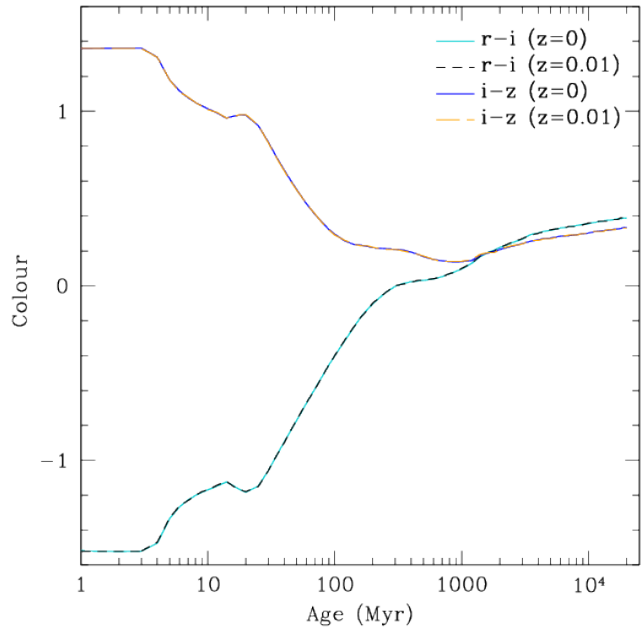

Figure 5.7: *Colour comparison for $r' - i'$ and $i' - z'$.*

5.3.3 Colours

First we determine how the addition of a younger population affects the colours of the overall galaxy in comparison to the single old population. The colour shift will naturally be toward the blue, but by what degree? The magnitude of the shift will be determined by both the age and mass fraction of the younger population.

Photometric magnitudes in each filter were taken from ZPEG and converted to fluxes via equation (2.2) using reference values of $f_o = 1$ and $m_o = 0$. In each filter, the fluxes from the younger (f_y) and underlying (f_o) population were summed to determine the composite flux (f_c):

$$f_c = f_y + f_o. \tag{5.5}$$

Once the composite flux was known, it was converted back to magnitudes via (2.1). Colours were then computed by taking appropriate differences between composite magnitudes.

Throughout the analysis we use the u,g,r,i,z SDSS data release 7 filter set (see figures 5.4 and 5.5 for their FWHM). We place emphasis on three different colours in our models: $u - g$, $g - r$ and $u - r$. Not only are these colours commonly used in observational surveys, $u - r$ is effective since the u filter is more sensitive to younger populations whilst r is more sensitive to older populations. Consequently we expect $u - r$ to be a robust diagnostic for examining composite population models. Figures 5.8, 5.9 and 5.10 show the colours $u - g$, $g - r$ and $u - r$ respectively as a function of young population age for a variety of mass ratio scenarios at redshift $z = 0.01$.

The underlying colour is the value of the ordinate at which all curves converge; this occurs at the age of the old population, specifically 10^{10} yr. This convergence is expected; when the age of the added "young" population reaches that of the underlying population, the colours of each component will be equal and consequently the composite colour will be identical to that of the underlying colour. The underlying colour (without any young component) is thus represented by a horizontal line at this vertical level through the entire plot. First note that the smallest mass ratio, $M_y/M_o = 10^{-5}$ has almost no impact on the underlying colour. As the mass ratio increases, a perturbation to this colour becomes apparent and grows in intensity. The greater the mass ratio, the bluer the composite colours (i.e. the lower the curve lies). As the mass fraction continues to increase and surpasses 10%, the composite curve tends to the single population black curve as expected. The more massive the

younger population relative to the old, the more it dominates the composite colour. Further, it is apparent that the young component has the most influence at younger ages, when its luminosity is larger. We will see shortly however (subsection 5.5.1) that when considering type Ia supernovae, not all ages shown in these figures are physically relevant.

We are not ultimately interested in the absolute colour of the composite populations, but rather the perturbation in the colour due to the young component in relation to the single, underlying population; specifically

$$\Delta(X-Y) = (X-Y)_{comp} - (X-Y)_{old} \tag{5.6}$$

where *comp* represents the composite (old + young) population and X and Y are filters. It is this colour shift that we will associate with a type Ia rate in future sections. Note that based on this definition $\Delta(X-Y) \leq 0$; the composite colour will always be bluer than (or equal to) the underlying colour. Now that we have explored the colours of our composite elliptical models, we turn to the other observable: the rates of type Ia SNe.

5.4 Metallicity

A quick note on metals in our models. The composite stellar populations we use start with an initial metallicity of $Z = 0.02$ where Z is the mass fraction of metals, and the metal content of the interstellar medium is then evolved with time. The main assumption we make is that colour shifts blue of the RS are due to younger stars; however as a result of the well-known age-metallicity degeneracy metal deficiencies can also replicate this effect. Metal poor stars are seen to have bluer colours, higher temperatures and shorter lifetimes than those with higher metallicities. Quantitatively this is described by the "3/2 rule": the spectral effects of a factor of 3 change in the age of a stellar population is nearly indistinguishable from those resulting from a factor of 2 shift in its metallicity (Worthey, 1994). As such the spectra of two stellar populations, one which is three times older but with half the metallicity, will appear nearly identical. Since we only explore the effect of age in our models, metallicity is an important quantity that should be examined in future work.

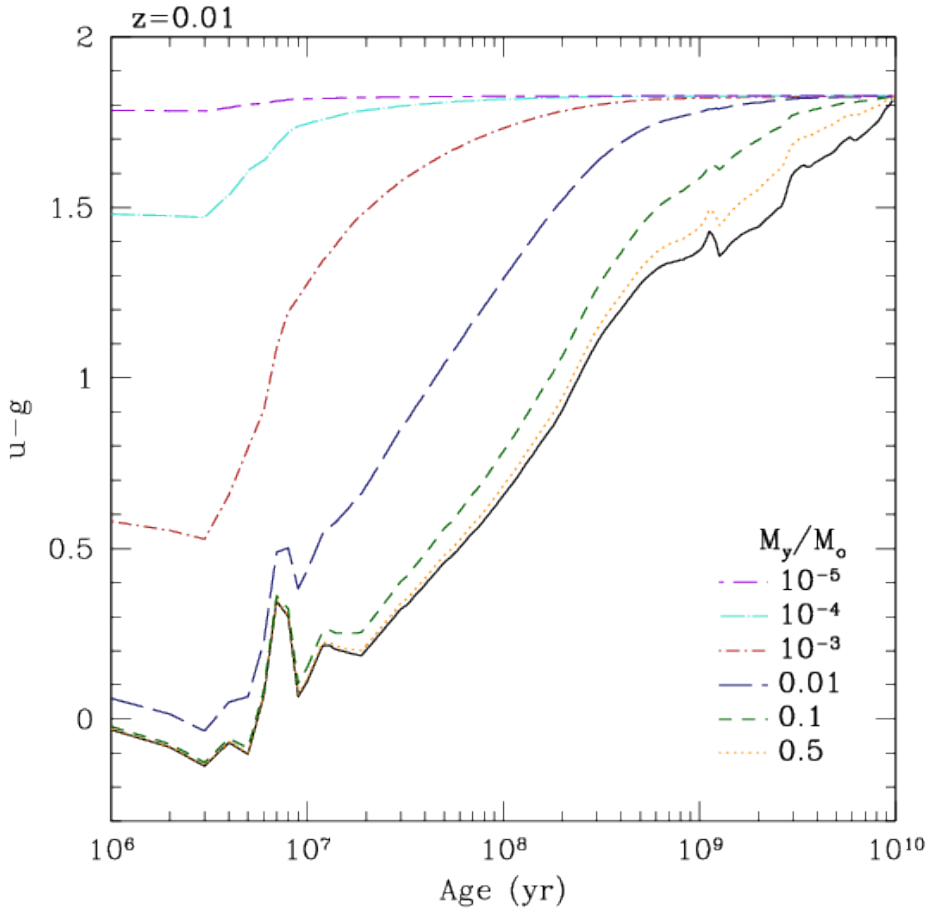

Figure 5.8: *Composite population $(u-g)$ colour as a function of young population age. The black curve represents a single simple population (i.e. no underlying component). The underlying population colour is the point of convergence of all curves. For reference, lower colour values are more blue.*

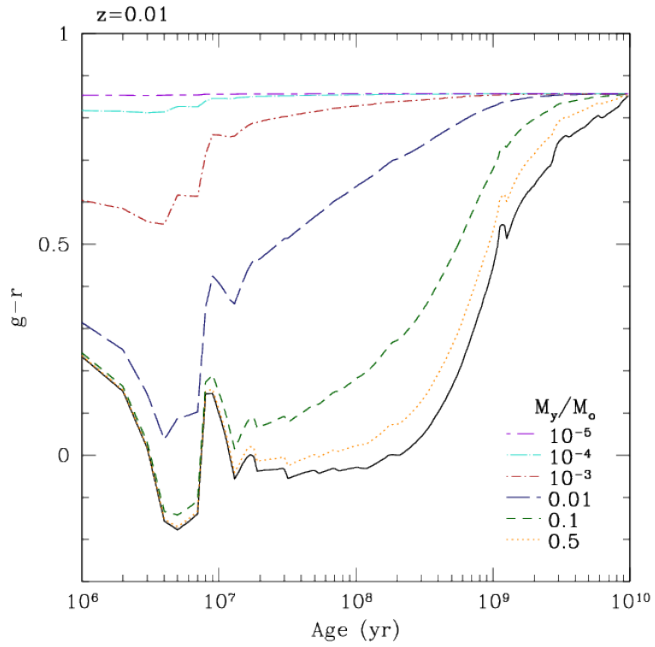

Figure 5.9: *Composite population* $(g-r)$ *colour as a function of young population age.*

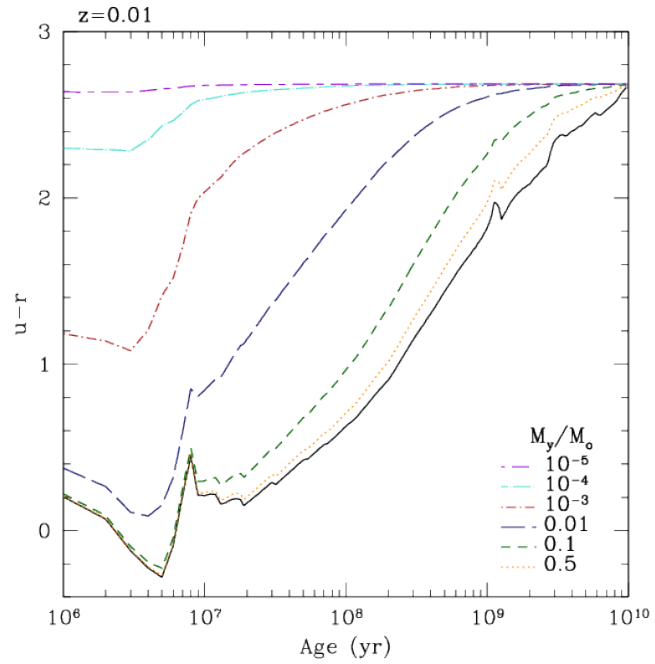

Figure 5.10: *Composite population* $(u-r)$ *colour as a function of young population age.*

5.5 Type Ia Supernova Rates

Normally, in a galaxy with a complex star formation history, the supernova rate at a given time is given by the convolution of the star formation history with the DTD:

$$SNR(t) = DTD(t) * SFR(t). \tag{5.7}$$

Since both components in our elliptical models consist of instantaneous bursts however ($SFR(t)$ is a delta function), the parameter t is simply the age of the component and we can use the DTD directly to find the SNR, specifically

$$SNR(t) = DTD(t) \tag{5.8}$$

We first begin with a power-law form for the delay-time distribution in which the rate in SN/yr is proportional to the time elapsed after a single burst (t) raised to some power x, $DTD \propto t^x$. The proportionality becomes an equality by adding in two constants: a normalization (C) and the mass of the stellar component (M),

$$SNR = C \cdot M \cdot t^x. \tag{5.9}$$

There is still a fair amount of uncertainty as to the DTD power x. Throughout our analysis we consider three different powers: the canonical $x = -1$ (e.g. Totani et al., 2008; Hachisu et al., 2008), $x = -0.7$ (e.g. Pritchet et al., 2008) and $x = -1.5$ (e.g. Maoz et al., 2010). As alluded to previously an $x = -1$ power corresponds to the DD scenario; a flatter power $x = -0.7$ resembles a case in which the WD formation rate determines the type Ia rate, and $x = -1.5$ best represents the SD channel (e.g. Mennekens et al., 2010; Hillebrandt et al., 2013). See the appendix (section A.5) for general derivations of the above. Note the DTD may not necessarily be described by a single tidy power law; its form depends on the dominant progenitor channel, over which there is still a considerable amount of debate. We explore this in more detail in subsection 5.5.5 in which we implement theoretical delay-time distributions into our models.

5.5.1 Age limits

Note that since not all stars form white dwarfs, there is a maximum main-sequence mass for a white dwarf progenitor. This maximum mass will set the timescale prior

to which no type Ia SNe will occur, since a degenerate white dwarf star is a necessary requirement. This timescale is thus the minimum young population age we can consider in our models. It is found (see section A.6 in appendix for derivation) that the stellar lifetime is a power-law relation dependent solely on the mass of the star, specifically

$$t \propto M^{-2.5}. \tag{5.10}$$

We can then insert values for the Sun, transforming the proportionality of (5.10) into an equality:

$$t = 10^{10} \left(\frac{M}{M_{\odot}} \right)^{-2.5}. \tag{5.11}$$

Assuming a maximum white-dwarf progenitor mass of 8 $M_{\odot}$ (see e.g. Heger et al., 2003), the main sequence lifetime of such a star is 55 Myr. Note equation (5.11) is an approximation since the mass-luminosity relationship differs depending on the mass of the star. For comparison, Buzzoni (2002) finds a fit to the main sequence lifetime and mass from theoretical models, specifically

$$\log(t) = 0.825 \log^2(M/120) + 6.43 \tag{5.12}$$

spanning the whole stellar mass range. Using the above we find a main sequence lifetime of 37 Myr for an eight solar mass star. These two values differ by less than a factor of two; we henceforth adopt 55 Myr as our cutoff age.

Since the lifetime of a star is inversely proportional to its mass (i.e. more massive stars burn their hydrogen faster and leave the main sequence more rapidly; see relation (5.10)), stars of eight solar masses will be the first to become white dwarfs after a single burst of star formation. Therefore it is only realistic to consider our composite models for ages $t > 55$ Myr; prior to this there are simply no white dwarfs to explode. Using 8 $M_{\odot}$ as the lower mass limit of core-collapse progenitors (i.e. see calculation (1.2)), it is also clear why we are only concerned with type Ia SNe. By 55 Myr, all core collapse progenitors ($M > 8M_{\odot}$) in a single burst have exploded due to their more rapid evolution (see also figure 1.2). Thus by adopting this cutoff in age we do not have to worry about contamination by core collapse objects, effectively separating the two broad classes of SNe.

5.5.2 Rate cutoffs

Even if we assume a power-law form for the delay time distribution, observational and theoretical studies both reveal that this power law is not constant over all age ranges. More specifically, at roughly $t \simeq 10^9$ yr, the single degenerate Ia rate drastically drops off (Greggio, 2005). To account for this astrophysically, consider the mechanism by which a type Ia supernova is formed. Irrespective of progenitor scenario (DD or SD), type Ia SNe require a binary star system. Furthermore, it is found that Helium white dwarfs do not explode; the primary must be a Carbon-Oxygen white dwarf. As stars of lower mass than $\sim 2M_\odot$ evolve off the main sequence, they develop a degenerate He core and become red giants. In order to begin burning He, these stars must undergo the core He flash which occurs when the stellar radius is of order a few hundred solar radii (Deupree & Wallace, 1987). If the star is in a binary system with a binary separation less than approximately $r \sim 400R_\odot$, the secondary may accrete enough mass from the primary to essentially truncate the evolution of the primary into a CO WD by preventing the He flash. Instead it becomes a He WD which cannot form a type Ia SN (Greggio, 2005). The He flash will fail to occur if the primary mass drops below roughly $\sim 0.5M_\odot$ *before* the primary reaches the tip of the red-giant branch. Such low-mass He WDs have been discovered and extensively studied (see e.g. Liebert et al., 2004). The minimum binary separation coupled with the primary mass requirement consequently sets the timescale upon which type Ia explosions occur. From relation (5.11) a $2M_\odot$ star has a main-sequence lifetime of approximately 1.8 Gyr (or 1.1 Gyr from equation (5.12)); any star less massive in a close binary is more likely to form a He white dwarf. Therefore a sharp dropoff results approximately 1-2 Gyr after an instantaneous burst of star formation. Such a rate falloff is not expected in the double degenerate scenario where both stars are already white dwarfs.

Incorporating a cutoff into our models will only serve to boost the rate of the young population relative to the old, while simultaneously lowering the absolute supernova rate. In other words, we will require a larger amount of blueing to explain the observed rates in ellipticals when compared to a scenario with no cutoff (i.e. the younger population must "do more work", providing more SNe). We modify the DTD to include two different cutoff scenarios:

1. A steep cutoff at which the DTD power suddenly becomes $x = -3.0$ at a specified age. In this case the underlying population will still contribute to the

type Ia rate albeit by a minimal amount (i.e. the young component, as long as it has age $t_y < t_{cutoff}$, will dominate the supernova rate).

2. A catastrophic cutoff at which the rate suddenly drops to zero. In this scenario the underlying population contributes *no* supernovae, and the young component is responsible for *all* type Ia events. The age of the young component is constrained by the cutoff age such that $t_y < t_{cutoff}$ in order to have *any* SNe in this scheme.

In this sense it is clear that the concept of a rate cutoff is inextricably linked to the degree to which young stellar frostings contribute SNe. If a cutoff exists beginning at 1-2 Gyr after a single burst of star formation, nearly all supernovae detected in ellipticals older than this limit *must* come from younger stars. Exploring whether a cutoff is possible is therefore of paramount significance.

5.5.3 Absolute rates

In order to compare with data, we derive the specific type Ia rate for our models. Calculation of rate values from the power-law form of the delay-time distribution (5.9) requires finding the normalization C. We normalize the delay-time distribution as follows. Constraints exist on the supernova rate in early-type galaxies from measurements of the most powerful starbursting galaxies. We use data from the SDSS-II Supernova Survey which discovered 520 spectroscopically confirmed type Ia SNe. Gao & Pritchet (2013) (hereafter GP) fit the "A+B" model (Scannapieco & Bildsten, 2005) to this SN host sample. The A+B model states that the supernova rate is a linear superposition of a prompt component dependent on the star formation rate (SFR) and a delayed component dependent on the mass of the galaxy (M) :

$$SNR = A \cdot M + B \cdot SFR \tag{5.13}$$

where A and B are constants. The A+B model can be recast by dividing out the mass, specifically

$$sSNR = A + B \cdot sSFR \tag{5.14}$$

in which $sSNR = SNR/M$ and $sSFR = SFR/M$ are the specific supernova and specific star formation rates respectively. For their sample GP find $A = 3.5^{+0.9}_{-0.7} \times 10^{-14}$ SNe/yr/$M_\odot$ and $B = 1.3^{+0.4}_{-0.3} \times 10^{-3}$ (SNe/yr)$(M_\odot/\mathrm{yr})^{-1}$. We will return to

the relevance of these values later (section 5.6). Considering the *specific* SN rates provides a common basis of comparison for galaxies regardless of mass. It is then straightforward to determine a non-specific rate by scaling by mass.

Figure 5.11 from GP plots the specific supernova rate of their sample against the specific star formation rate. The upper-rightmost SDSS (solid circular) point $((\log(sSFR), \log(sSNR)) \sim (-9.2, -12.2))$ represents the youngest and most powerful star forming galaxies; it is this point we use for normalizing the delay time distribution. Based on the sSFR, these galaxies formed all of their stars within roughly 0.5 to 1 Gyr. Further, measurements of the SFR in galaxies are typically made as an average over the past few hundred million years (e.g. Sullivan et al., 2006 use 500 Myr). Thus we adopt a rate of $sSNR = 10^{-12.2}$ SNe/yr/$M_\odot$ for a maximum age of $t = 5 \times 10^8$ yr. The most powerful bursts cannot maintain such a strong SFR (and consequently SNR) beyond this age (since the galaxy would be fully formed), providing a constraint on our type Ia rates.

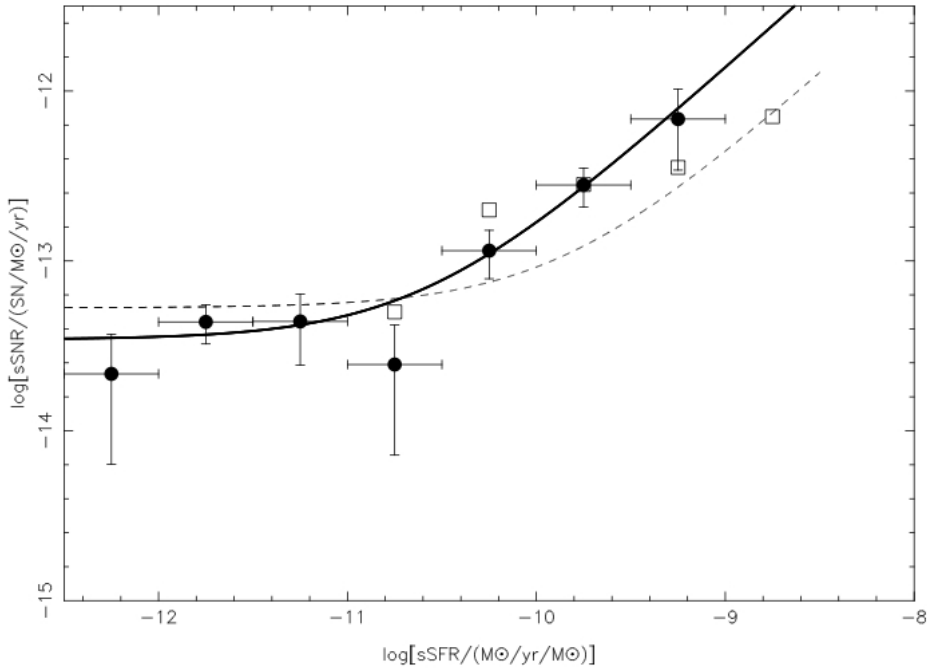

Figure 5.11: *Specific supernova rate versus specific star formation rate of galaxies from GP. Black points are from the SDSS-II SN Survey, the black curve represents their best-fit A+B model; the squares and dashed line are data from the Supernova Legacy Survey and predictions respectively from Sullivan et al. (2006).*

Normalization consists of starting with the power-law DTD, equation (5.9). To

find the specific rate for an individual stellar population divide by mass to yield

$$sSNR = C \cdot t^x. \tag{5.15}$$

Then we solve for the constant C given three different values for the power, $x = -1.0, -0.7, -1.5$. Each DTD power yields a different normalization.

Why do we normalize to the younger end and not the older (instead of, for instance, normalizing our underlying population to the "A" value)? We are ultimately concerned with how the addition of a young stellar frosting to an old galaxy affects both the colours and the supernova rate. As such, normalizing to the younger side ensures a greater accuracy when we add in a young component. It will be shown later (section 5.6) that this choice of normalization is quite reasonable.

Our models consist of two stellar components: one young and one old. Moreover, they feature no continuous star formation, and so in the A+B model we can neglect the B component; the rate is solely proportional to the mass of the galaxy. It is therefore the value of A that we will compare our model results to. We do not use the A+B model to determine rates but a power law form of the delay-time distribution. To analytically determine the total specific SNR, we add the SNR of each galaxy component (old and young), from equation (5.9), and divide by the total mass of the galaxy $M_T = M_y + M_o$:

$$\begin{aligned} SNR &= SNR_y + SNR_o \\ sSNR &= \frac{SNR}{M_T} \\ sSNR &= \frac{C_y}{1 + M_o/M_y} t_y^w + \frac{C_o}{1 + M_y/M_o} t_o^z. \end{aligned} \tag{5.16}$$

in which the DTD powers w and z are not necessarily equal for each stellar component. Likewise the normalizations C_y and C_o can also in principle differ in accordance with the DTD powers. Notice how absolute masses cancel and we are merely left with relative mass fractions.

For a straight DTD power law the exponents are equal ($w = z$). Implementing a rate cutoff into (5.16) is fairly straightforward. For a $x = -3.0$ cutoff, we change the power when $t > t_{cutoff}$. A catastrophic cutoff, on the other hand (assuming $t_y < t_{cutoff}$, otherwise we have no SNe), involves truncating the old rate such that the second term on the right side of (5.16) is zero. In order to properly implement a

cutoff in the rate we must perform an additional normalization.

5.5.4 Cutoff normalization

For a non-catastrophic supernova rate cutoff, once the age of a population surpasses the cutoff, $t > t_{cutoff}$, the DTD power changes. To properly take this into account we must normalize the second segment in the delay-time distribution such that it is a continuous function, i.e.

$$sSNR = \begin{cases} C_1 \cdot t^x & , \ t < t_{cutoff} \\ C_2 \cdot t^{-3} & , \ t > t_{cutoff} \end{cases} \tag{5.17}$$

in which t is the age of the stellar population in question, C_1 the normalization found as discussed previously using the appropriate power x and C_2 the normalization under the condition that the two functional forms are equal at $t = t_{cutoff}$. Since C_1 differs with the three values of x that were tested, so too will C_2. A sample DTD with proper normalizations is given in figure 5.12.

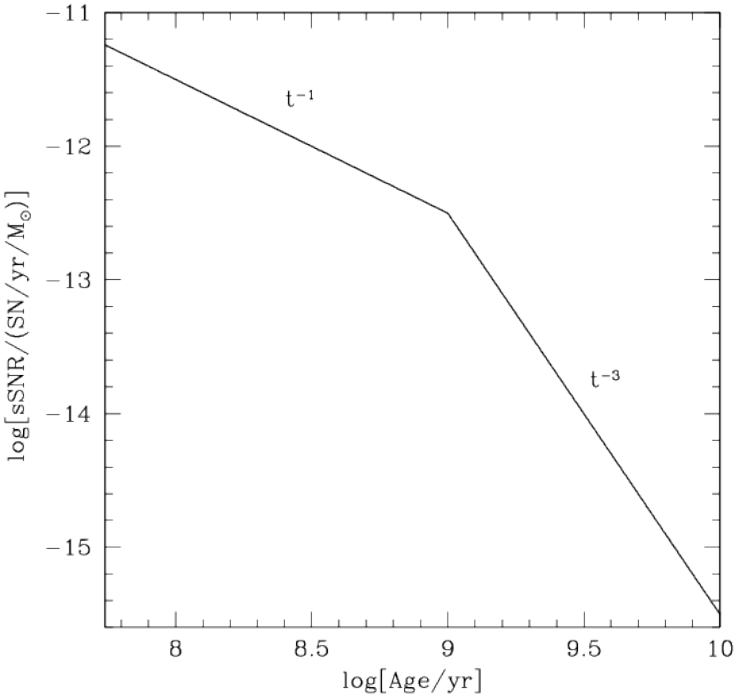

Figure 5.12: *Sample delay-time distribution with a pre-cutoff power of $x = -1$, a cutoff at 1 Gyr and a post-cutoff power of $x = -3$. Normalization was performed as discussed in the text.*

On the other hand, a catastrophic cutoff takes the functional form

$$sSNR = \begin{cases} C_1 \cdot t^x & , \; t < t_{cutoff} \\ 0 & , \; t > t_{cutoff} \end{cases} \tag{5.18}$$

at which the supernova rate goes to zero immediately after reaching the cutoff age.

5.5.5 Theoretical delay-time distributions

The delay-time distributions discussed thus far can be considered "observational" in nature: they have been estimated through empirical large-scale SN surveys. In addition to observational efforts, there have been many simulations performed using population synthesis codes to theoretically compute the DTD, dating back almost two decades (e.g. Tutukov & Yungelson, 1994; Nelemans et al., 2001; Mennekens et al., 2010). The advantage in modelling delay times theoretically lies in the ability to separately examine DTDs of the two main candidate progenitor models: single

and double degenerate. This is in stark contrast to observational programs, which simply observe supernovae that occur but have no way to distinguish between the various type Ia channels. As usual, theory and observation have an intricate and vital relationship; through separately modelling the DTD of each progenitor scenario and comparing to empirical data, we can gain a better understanding of the routes through which type Ia supernovae form.

In addition to the observational DTDs discussed above we consider the theoretical delay-time distributions derived by Mennekens et al. (2010) using a population number synthesis code. See figure 5.13 for a plot of their results.

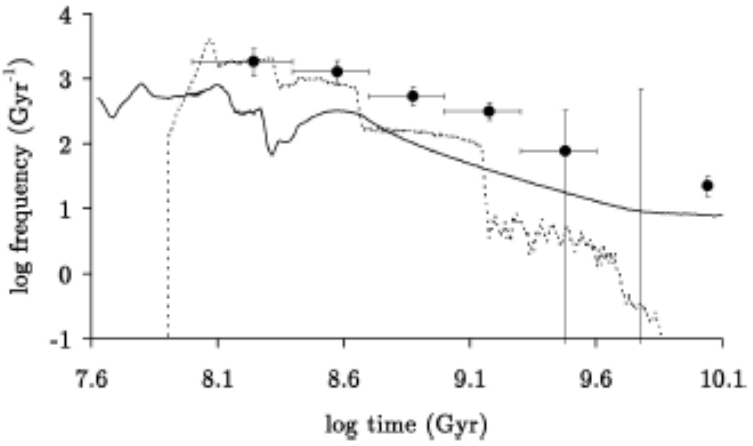

Figure 5.13: *DTDs from Mennekens et al. (2010) of a $10^6 M_\odot$ single-burst for the DD scenario (solid line) and SD scenario (dotted line) in comparison to observational data points.*

We approximate each theoretical curve as a series of power laws. For the double-degenerate scenario we use two different power laws,

$$DTD_{DD} = \begin{cases} C_1 \cdot t^{-0.65} & , \ t < 400 \ Myr \\ C_2 \cdot t^{-1} & , \ t > 400 \ Myr \end{cases} \tag{5.19}$$

where the minimum age as before is 55 Myr. As can be seen from figure 5.13, the single-degenerate scenario has quite a different behaviour; SNe begin abruptly and at a later age than in the DD case. As such there is a period with no SNe, followed by

two power laws:

$$DTD_{SD} = \begin{cases} 0 & , \ t < 115\ Myr \\ C_1 \cdot t^{-1.55} & , \ 115\ Myr < t < 1.4\ Gyr \\ C_2 \cdot t^{-2.55} & , \ t > 1.4\ Gyr \end{cases} \tag{5.20}$$

Note the SD DTD is quite similar to our observational DTD ($x = -1.5$ pre-cutoff and $x = -3$ post-cutoff), and features a cutoff at 1.4 Gyr (we test cutoffs at 1 Gyr and 2 Gyr).

In order to normalize the DTDs we use the topmost point in each curve as the initial normalization and then follow the constraint that the DTD must be a continuous function. It is clear from figure 5.13 that neither the SD nor DD channels are sufficient to reproduce the absolute number of observed events; even a combination of the two falls short of the mark. However, it is remarkable that these theoretical DTD's are within a factor of at least 3 of the correct rates. Theoretical simulations via population synthesis codes rely on a variety of unconstrained input parameters (e.g. distributions of primordial binary mass ratios and separations) and assumptions (e.g. prescriptions for mass exchange between the companions). That they come within a few factors of the observed rates is quite an achievement.

Given the theoretical underestimate, for the purposes of normalization we choose the largest rate value for each curve to reach as close as possible to observed rates. Frequency in Gyr^{-1} must be converted to sSNR in $\mathrm{SN/yr}/M_{\odot}$ prior to normalization. To account for the near vertical SD dropoff at 1.4 Gyr, we use the lower point of the drop to normalize the second power law to emulate the effect. The resulting DTDs are plotted in figure 5.14 alongside one of our observational DTDs for the purposes of comparison.

Until approximately 1.6 Gyr, the three curves are less than an order of magnitude apart in absolute number. Prior to 1.4 Gyr, the SD DTD dominates the DD DTD by up to an order of magnitude; after this point the SD rate drops off quite rapidly below the DD rate. After approximately 8 Gyr - a cutoff time determined by the main sequence lifetime of the least massive companion stars that can result in a SD type Ia SN - the SD rate completely disappears. In comparison to the DD DTD, our observational DTD has a much steeper decay ($x = -3$ compared to $x = -1$) at an earlier cutoff and drops below the DD rate after they intersect at roughly 2 Gyr.

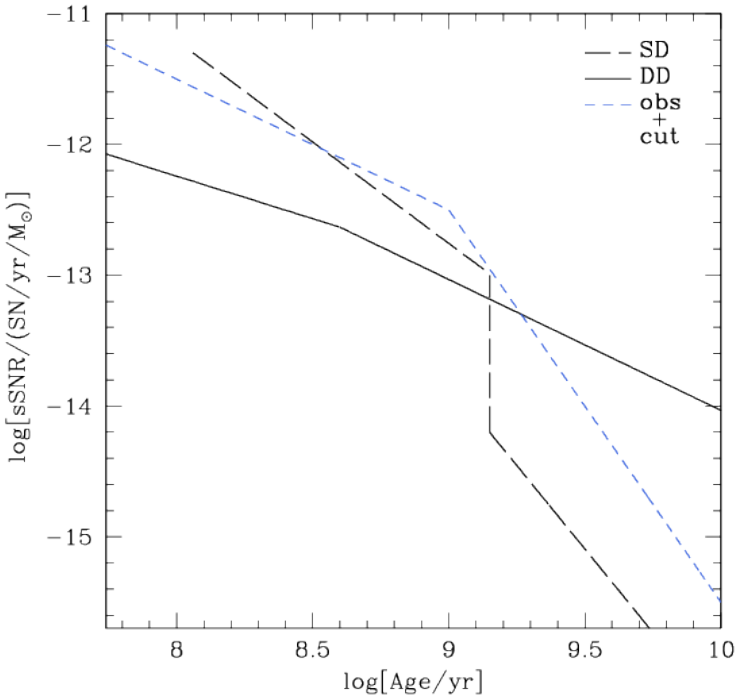

Figure 5.14: *Theoretical DTDs (black) modelled based on those of Mennekens et al. (2010) as described in the text (see figure 5.13). For comparison an observational DTD we use is shown (blue) featuring an $x = -1$ power to a 1 Gyr cutoff followed by a power $x = -3$. Note how the SD curve starts at a later age as seen in figure 5.13.*

5.5.6 Relative rates

While absolute supernova rates provide an important metric with which to compare model results to observational measurements, we may also be interested in relative rates from a more theoretical standpoint. More specifically, we can ask what kind of enhancement the young component has on the underlying population in terms of Ia rates. Since we are dealing with differential supernova rates, the normalization C in equation (5.9) will drop out and is not of significance. We are interested in the contribution of the younger population to the overall composite population supernova rate:

$$\frac{R_y}{R_T} = \frac{R_y}{R_y + R_o} \tag{5.21}$$

in which R_T denotes the total composite rate. Inserting (5.9) using the appropriate masses for each population yields

$$\frac{R_y}{R_T} = \frac{M_y t_y^x}{M_y t_y^x + M_o t_o^x}. \tag{5.22}$$

Since the mass fraction itself was varied, we can rewrite (5.22) by factoring M_o out of the denominator, resulting in

$$\frac{R_y}{R_T} = \frac{M_y}{M_o} \frac{t_y^x}{\frac{M_y}{M_o} t_y^x + t_o^x}. \tag{5.23}$$

Thus it is clear how the relative rate depends on the mass ratio and age of each population.

The relative rate was plotted as a function of young population age using the same three DTD powers discussed above; see figures 5.15, 5.16 and 5.17. Note these plots feature a single power-law with no cutoff. We see expected behaviour in that the rate contribution decreases as the younger population ages, in agreement with the form of the DTD (see equation (5.9)). For a less steep DTD power ($x = -0.7$) even a young population half the mass of the underlying component would not be able to produce 100% of all type Ia events. As the power-law steepens, the mass cutoff becomes more lenient; for $x = -1.5$, even young populations with $M_y/M_o > 0.01$ can come close to producing all SNe. Throughout all three DTD powers the smallest mass curve $M_y/M_o = 10^{-4}$ has almost no noticeable effect on the rates. As mentioned figures 5.15 to 5.17 are plotted assuming a single invariant power law DTD through all ages; if we were to impose a cutoff of the sort discussed previously and reproduce these plots, we would find $R_{young}/R_{total} \simeq 1$ for nearly all models in which $t_{young} < t_{cutoff}$. As such these plots represent lower limits on the relative rates.

With the analytical framework in place to examine both type Ia rates and elliptical model colours, we incorporate these two observables in the next section.

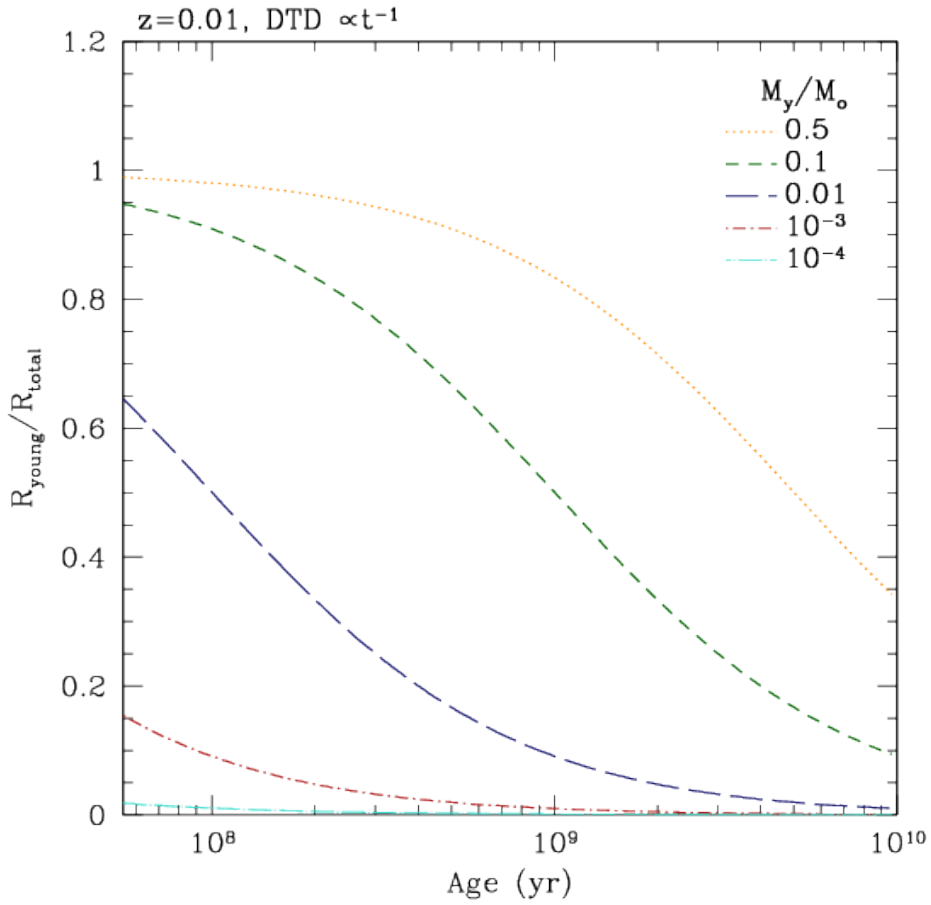

Figure 5.15: *Relative type Ia rate of young stellar population to composite population as a function of young population age at redshift 0.01 for DTD power $x = -1$. The five curves correspond to different mass ratios.*

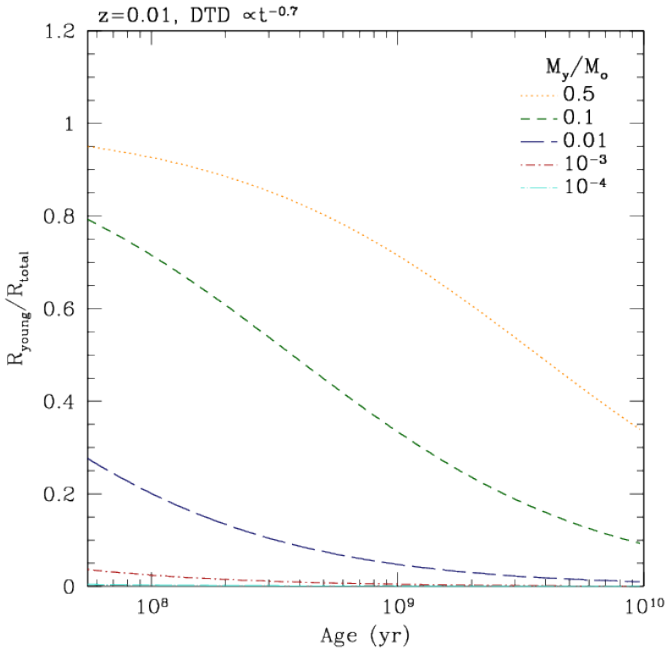

Figure 5.16: *Relative type Ia rate of young stellar population to composite population as a function of young population age at redshift 0.01 for DTD power* $x = -0.7$.

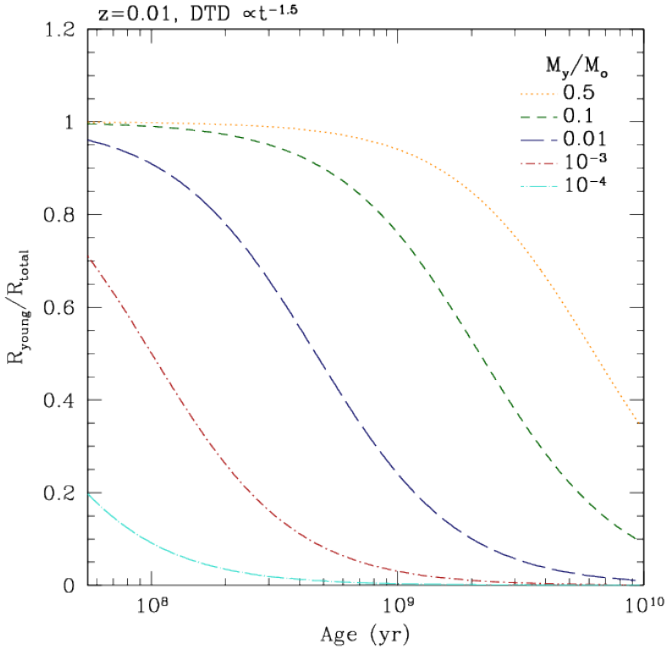

Figure 5.17: *Relative type Ia rate of young stellar population to composite population as a function of young population age at redshift 0.01 for DTD power* $x = -1.5$.

5.6 Results

To best display the data, we plot our two observables - the type Ia SN rate as a function of the colour shift - for a variety of different colours and model parameters. Unless stated otherwise we fix the redshift at $z = 0.01$. These plots outline how a given shift in colour results in a specified Ia rate, whether absolute or relative. Points on each curve correspond to different model parameters. To construct each curve, we set the mass ratio M_y/M_o constant and vary the age of the younger component. We also tried the opposite approach: fixing the young population age and varying the mass ratio. We stick to the former, somewhat more intuitive approach given the fact that population template ages are discrete and not continuous.

5.6.1 Relative rates

First we examine the relative rates and show a sample plot for a straight power-law in figure 5.18. This plot demonstrates how the shift in colour corresponds to an enhancement in supernova rate.

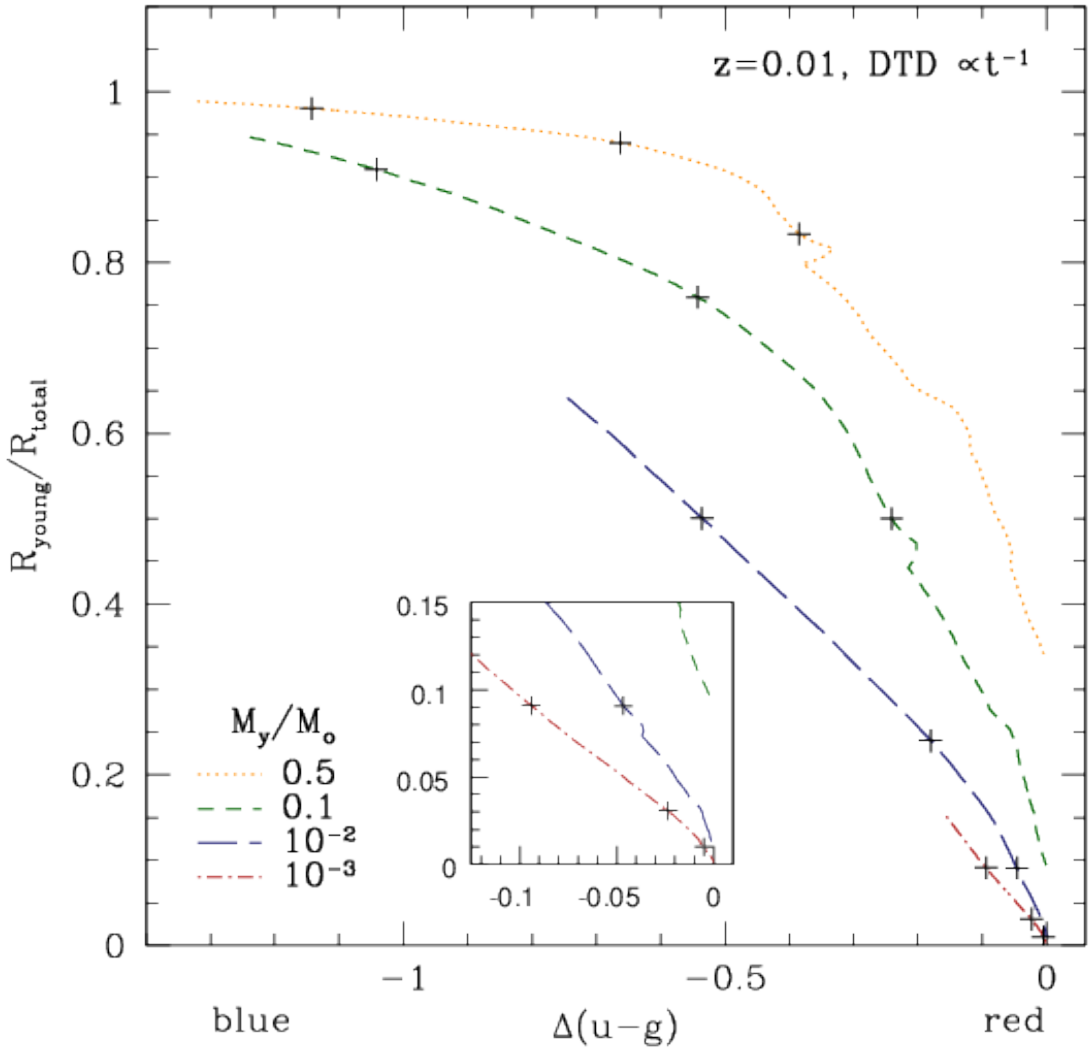

Figure 5.18: *Type Ia SNe relative rate as a function of colour difference* $(u-g)$ *utilizing a DTD power* $x = -1$*. Each curve represents a different mass ratio. Proceeding from right to left, the age of the added population decreases (i.e. a younger population contribution at a given mass ratio is more blue) and the crosses on each curve denote ages of* 10^8*,* $10^{8.5}$ *and* 10^9 *yr. The inset is a magnified version of the bottom right corner of the plot.*

5.6.2 Absolute rates

Observational

We produce similar plots but using absolute rates on the vertical axis; see figures 5.19, 5.20 and 5.21 for plots of a straight power law in three different colours. These plots show the amount of blueing required to explain a given, measured sSNR for various different models of mass fraction and age. The upper dotted line in each plot denotes the sSNR for the strongest starbursts (i.e. the most extreme point from GP) whereas the lower line is the typical "A" value (from the A+B model) taken from the same study. These two lines denote our region of measured Ia rates and represent an important constraint.

Note that as each curve converges to $\Delta(X - Y) = 0$ (the younger component age reaches that of the underlying component), the sSNR values nearly converge to the base elliptical rate as expected. Also in line with expectations, nearly all of each curve lies between these two values; adding some portion of a younger population enhances the Ia rate beyond the base "A" rate. Both the rate convergence to the expected value and the curves being well constrained in the observational region imply that our choice of normalization works quite well, at least for this specific observational DTD. Note that the curves are best separated in $u - g$, which looks to be an excellent diagnostic colour for separating out models. Furthermore $u - g$ becomes more sensitive to younger populations at higher redshift as ultraviolet light begins to shift into the u band. In contrast, the $g - r$ curves show a much tighter relation which may be advantageous for drawing general conclusions; this will prove useful for applying our models to observations in section 5.7.

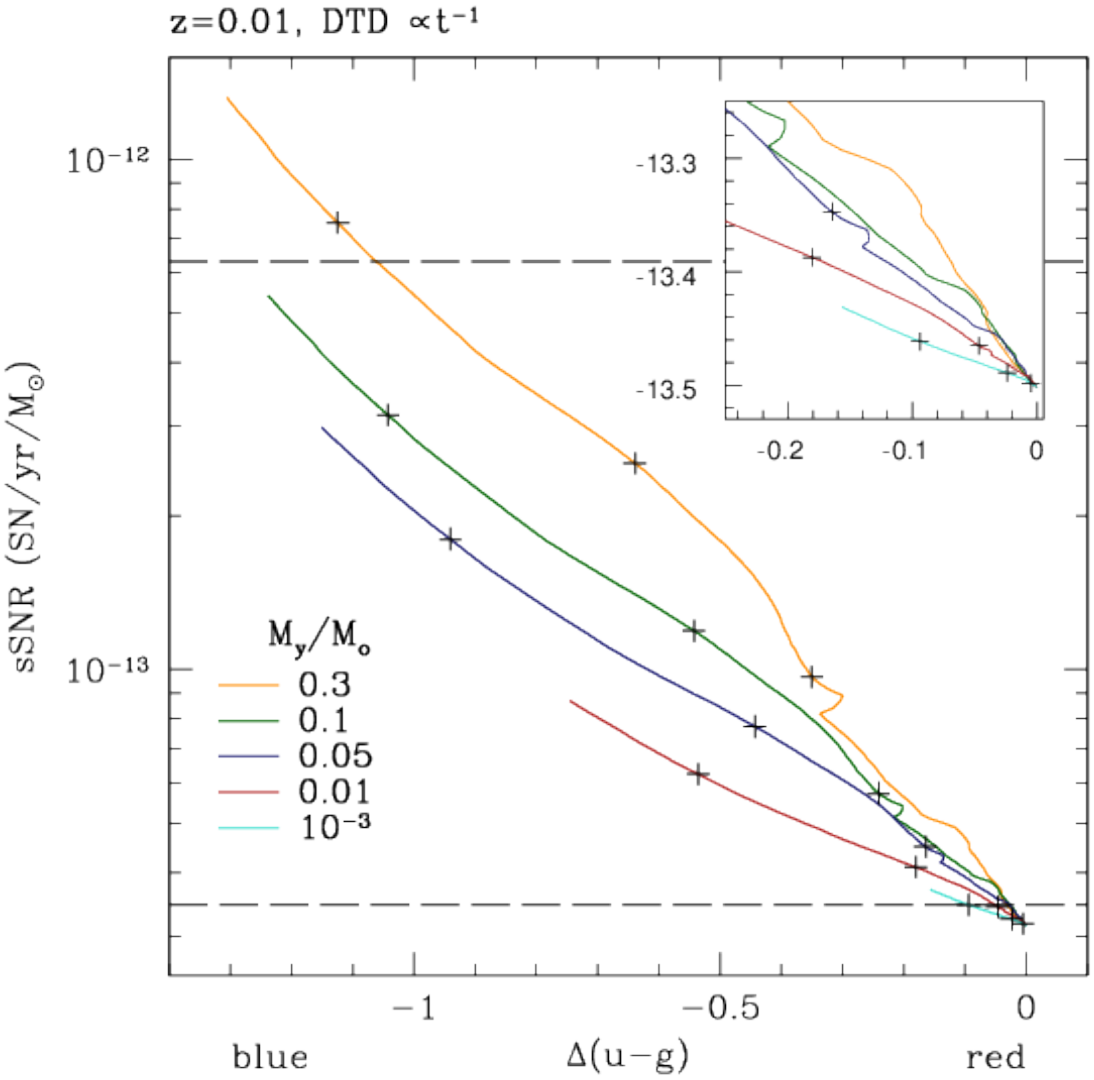

Figure 5.19: *Type Ia specific SNe rate as a function of colour difference* $(u-g)$ *for redshift of* $z = 0.01$ *and DTD power* $x = -1.0$ *with no rate cutoff. Each curve represents a different mass ratio used in the stellar population models. Proceeding from right to left, the age of the added population decreases (i.e. a younger population contribution is more blue) and the crosses on each curve denote ages of* 10^8, $10^{8.5}$ *and* 10^9 *yr. The inset is a magnified version of the bottom right corner of the plot. The upper dotted line represents the rate of the most extreme young starbursting galaxies whereas the lower line shows the typical rate in ellipticals (values utilized are described in the text).*

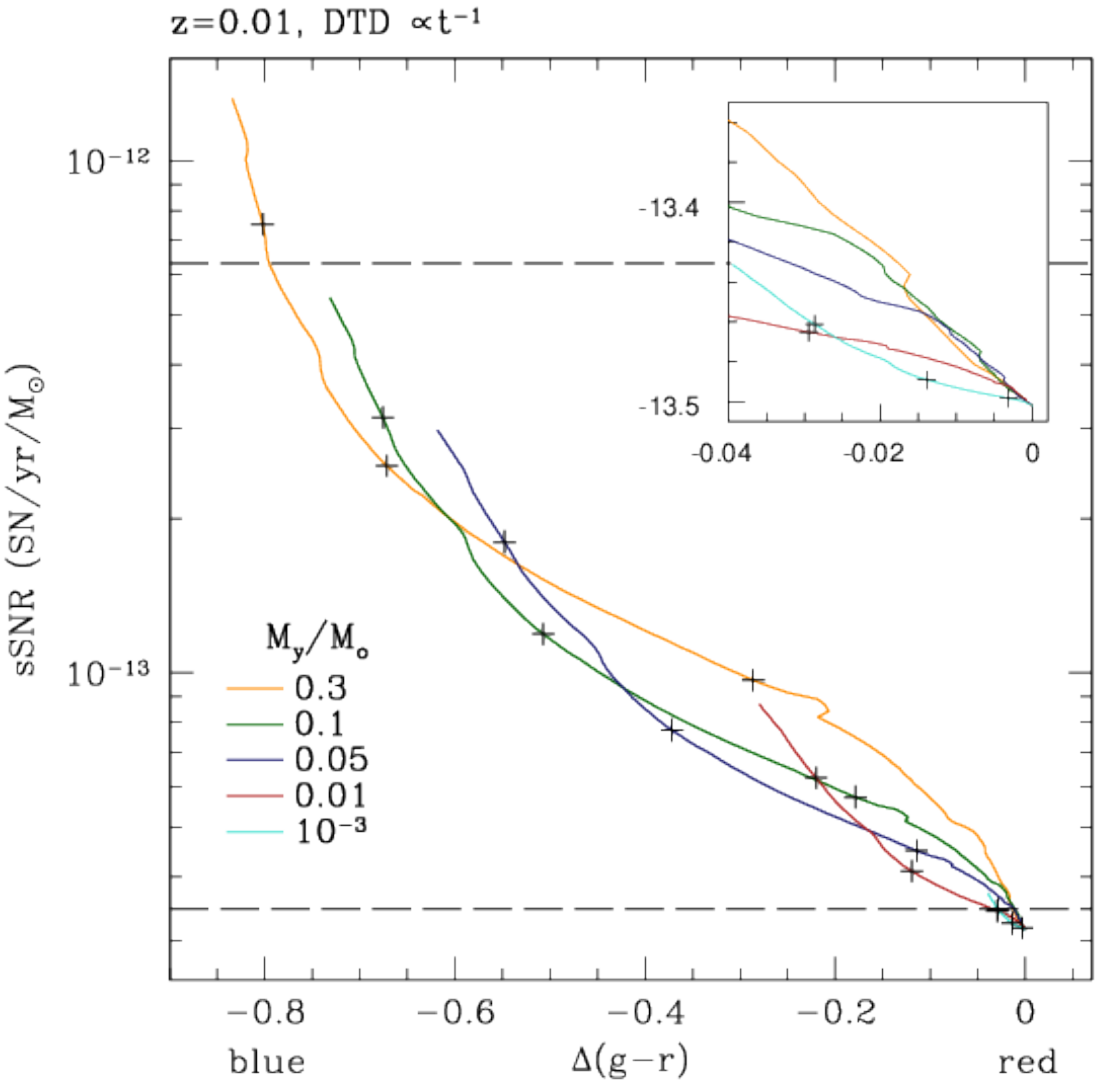

Figure 5.20: *Type Ia specific SNe rate as a function of colour difference* $(g-r)$ *for a redshift of* $z = 0.01$ *and DTD power* $x = -1.0$.

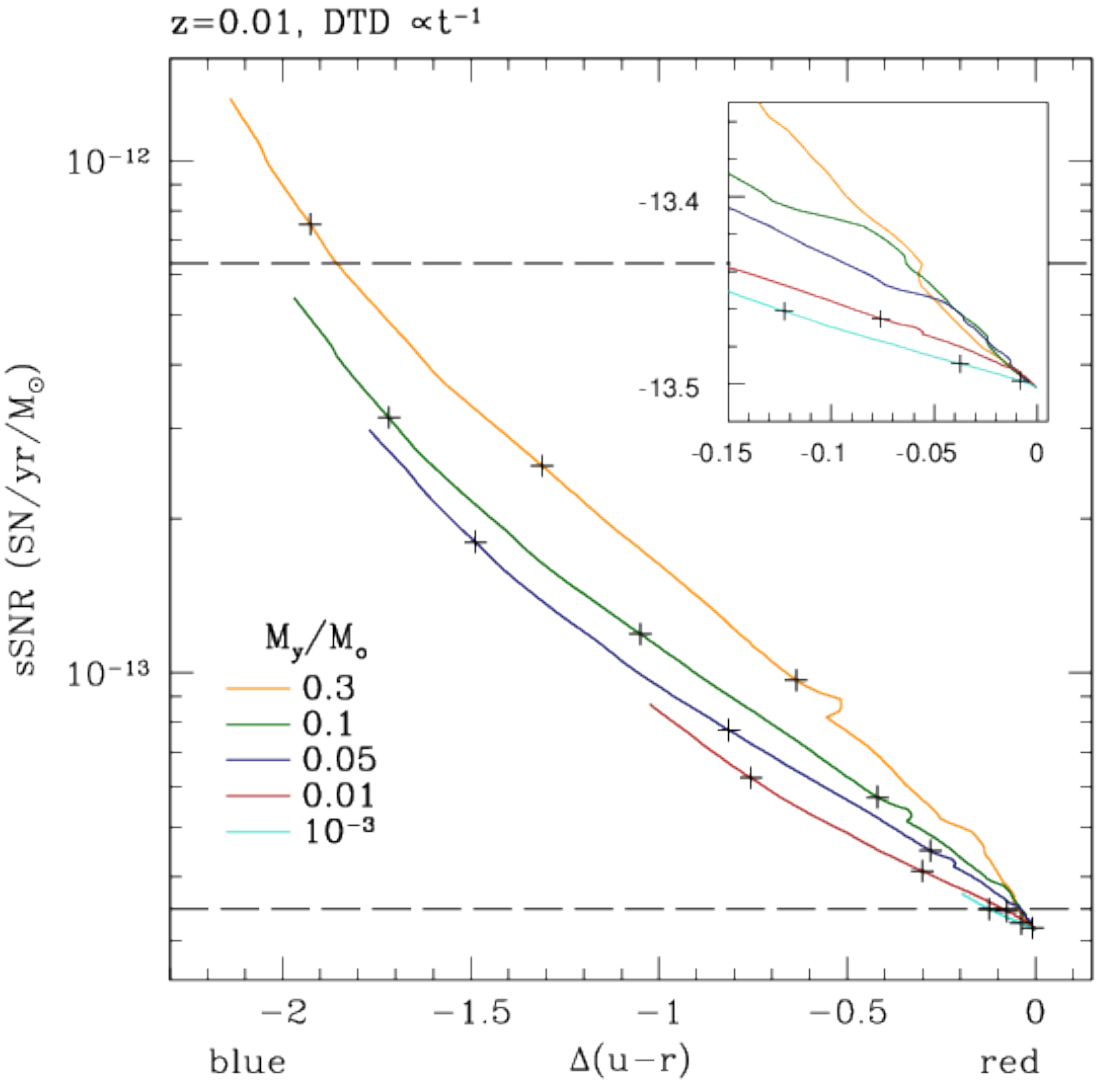

Figure 5.21: *Type Ia specific SNe rate as a function of colour difference* $(u-r)$ *for a redshift of* $z = 0.01$ *and DTD power* $x = -1.0$

Differing DTD power

What effect does differing the power-law have on these plots? We explore this in figures 5.22 and 5.23 for $u - g$. Comparing figure 5.22 to figure 5.19, a power of $x = -0.7$ boosts the apex of specific supernova rate above the base elliptical rate and flattens out the curves, making them less steep. The range in rates is also reduced, covering just less than an order of magnitude, though almost entirely lying within our observable region. Likewise, $x = -1.5$ (figure 5.23) drops the sSNR apex below the elliptical rate and steepens the curves while increasing the range in rates to cover over two orders of magnitude. A large section of the curves still lies within the observable region.

Why is there a mismatch between the vertices of the $x = -0.7$ and $x = -1.5$ plots and the "A" value? Recall that we normalized on the younger end of the DTD using the most extreme star-forming galaxies and not to the older end. As such we do not expect a convergence to the older end; since the range in rates changes with DTD power, the curves vertically stretch or compress accordingly.

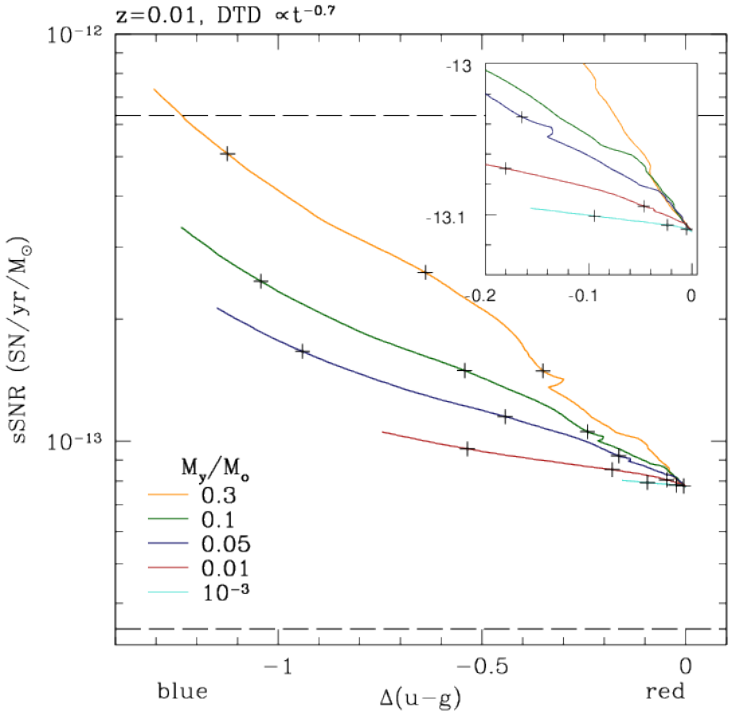

Figure 5.22: *Type Ia specific SNe rate as a function of colour difference* $(u-g)$ *for redshift* $z = 0.01$ *and DTD power* $x = -0.7$.

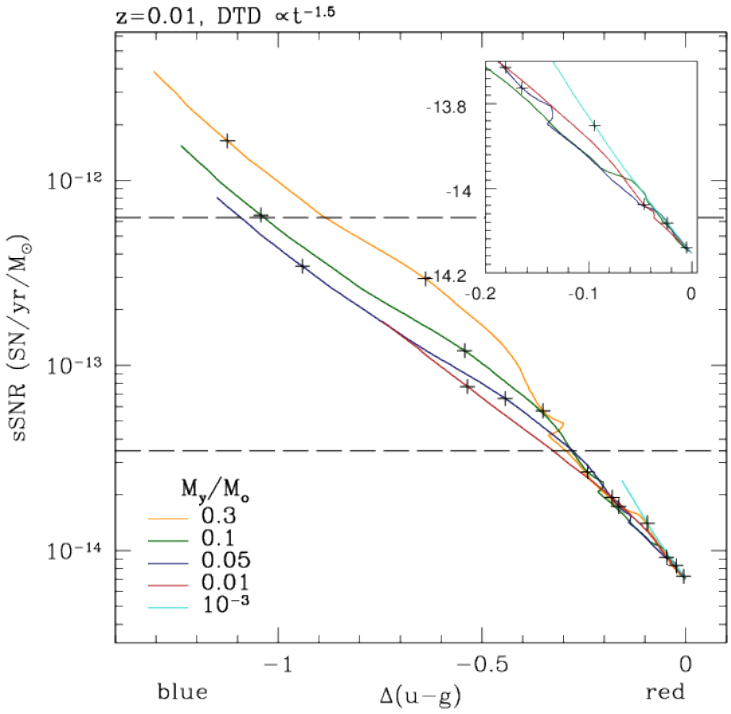

Figure 5.23: *Type Ia specific SNe rate as a function of colour difference* $(u-g)$ *for redshift* $z = 0.01$ *and DTD power* $x = -1.5$.

Cutoffs

We also explore observational DTDs with cutoffs as described in subsections 5.5.2 and 5.5.4. We show plots in $u - g$ for the canonical pre-cutoff power $x = -1$ to illustrate the effect. Figure 5.24 plots the specific rate versus colour difference $(u-g)$ for a pre-cutoff DTD power $x = -1$ with a non-catastrophic cutoff at $t_{cutoff} = 1$ Gyr, while figure 5.25 demonstrates a catastrophic cutoff.

Comparing figures 5.19 and 5.24, the behaviour of the curves is near-identical out until the young population reaches the cutoff age, at which point the specific rate plummets, converging about two dex lower than the straight power law. That this apex is two orders of magnitude lower than the "A" value is telling: to achieve a realistic SN rate with our models requires the young population to have an age less than the cutoff. It can be seen especially in the catastrophic cutoff plots (e.g. figure 5.25) that throughout the age interval $t < t_{cutoff}$, the sSNR is typically bounded in the observational region.

The difference between figures 5.24 and 5.25 is apparent: the catastrophic cutoff (the latter) truncates at a colour difference dependent on the mass ratio whereupon the rate immediately converges to zero. In a similar fashion to the non-catastrophic cutoff, the truncation occurs when the young component age reaches that of the cutoff, $t_y = t_{cutoff}$. Given the catastrophic cutoff scenario it is further apparent that any SNe observed in galaxies with a colour shift $\Delta(u - g) > -0.2$ can only be due to a very small contribution from a young population, $M_y/M_o < 0.01$, otherwise the rate would simply drop to virtually zero. Considering both cutoff scenarios, it is clear in order to reach the typical type Ia rate we require a colour shift of at least $\Delta(u - g) < -0.3$, otherwise the rate is too low.

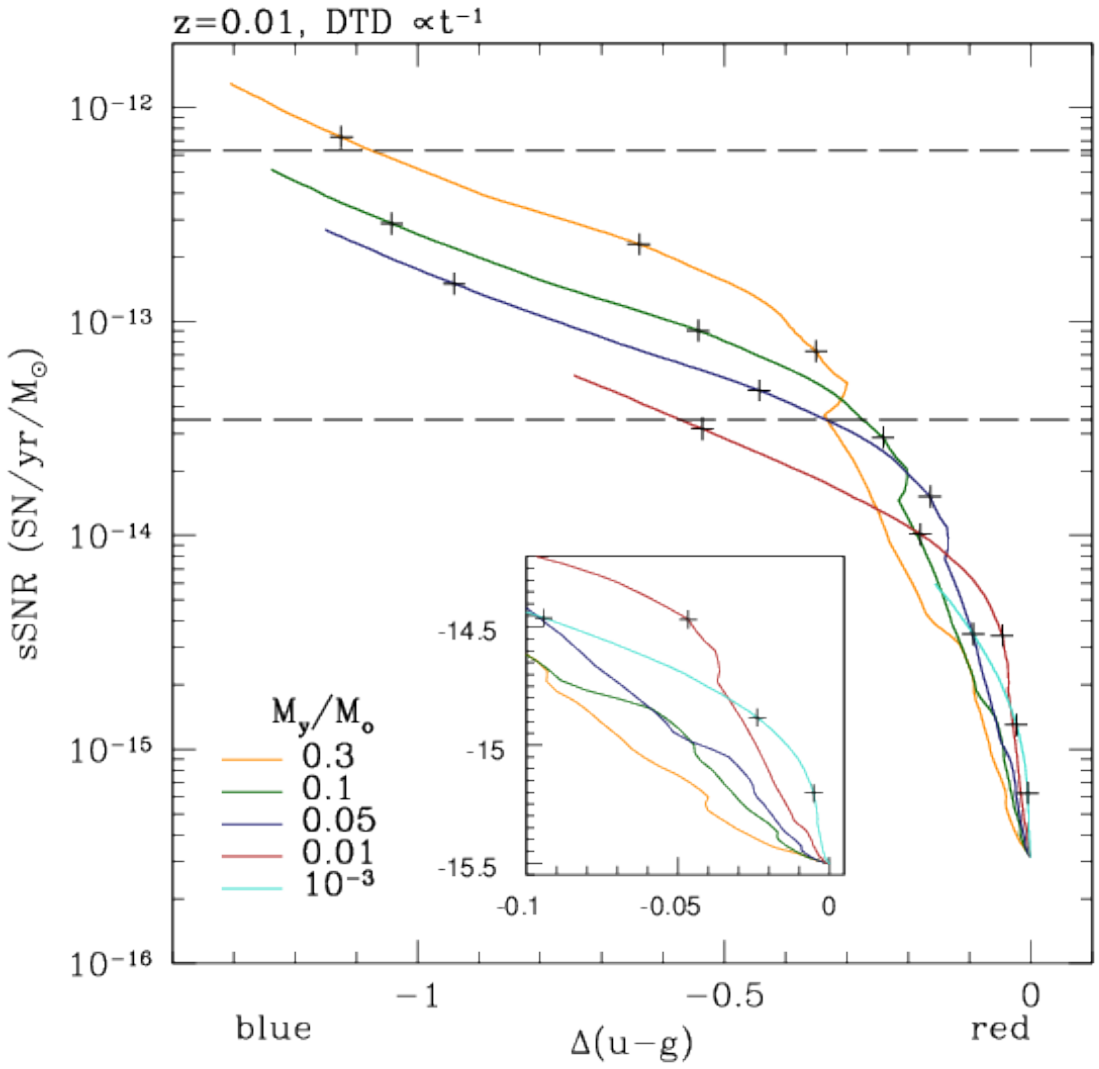

Figure 5.24: *Specific supernova rate as a function of* $(u-g)$ *colour shift for a pre-cutoff DTD power* $x = -1$*, a cutoff at 1 Gyr followed by a post-cutoff power* $x = -3$*.*

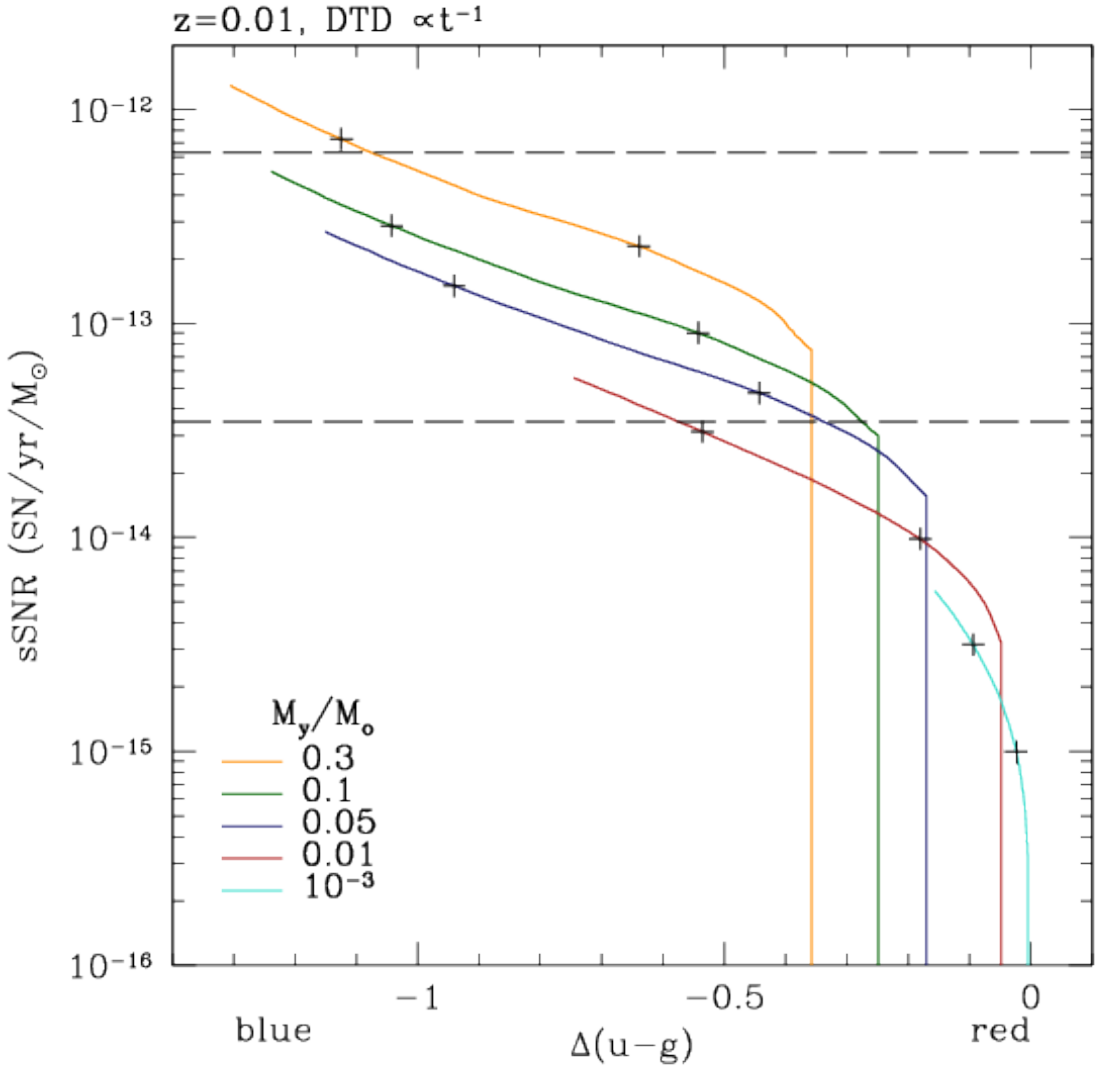

Figure 5.25: *Specific supernova rate as a function of $(u-g)$ colour shift for a pre-cutoff DTD power $x=-1$ and a catastrophic cutoff at 1 Gyr.*

Cutoff Age

We also explore the effect of varying the cutoff age since there is some uncertainty in this value. This is done for a pre-cutoff DTD power $x = -1$ to a cutoff age of 2 Gyr. Figure 5.26 plots this for a non-catastrophic cutoff and figure 5.27 for a catastrophic cutoff. Increasing the cutoff age merely serves to push the point at which the rate diverges downward farther to the right (i.e. to a lesser colour difference). This is expected since the young population can be older and still contribute a significant amount of SNe - in line with the cutoff age being greater - and an older contribution corresponds to a lesser colour shift. In the case of a $x = -3$ cutoff, the convergence is at a larger sSNR as well, due to the difference in normalization C_2; ultimately due to the change in t_{cutoff}.

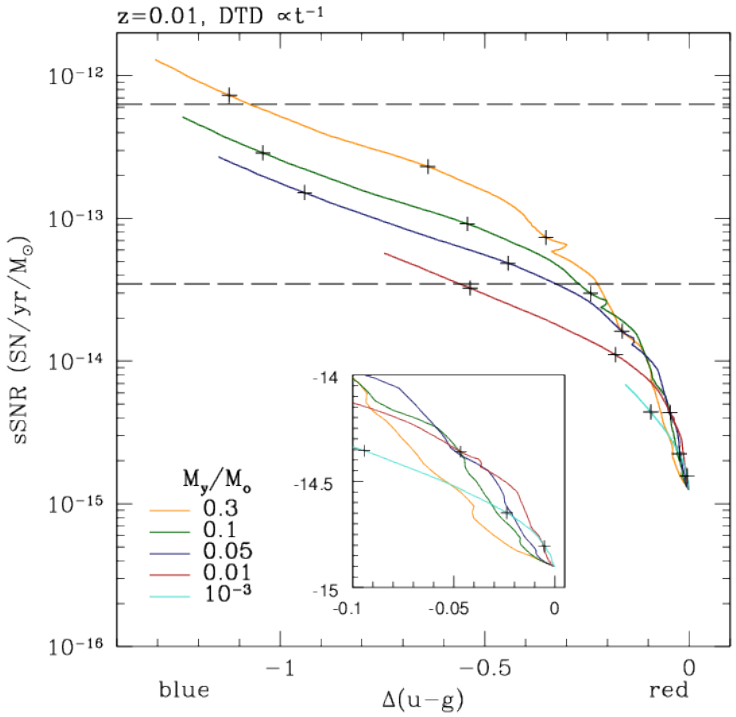

Figure 5.26: *Type Ia specific SNe rate as a function of colour difference* $(u-g)$ *for redshift* $z = 0.01$ *and DTD power* $x = -1$ *with a non-catastrophic cutoff at 2 Gyr.*

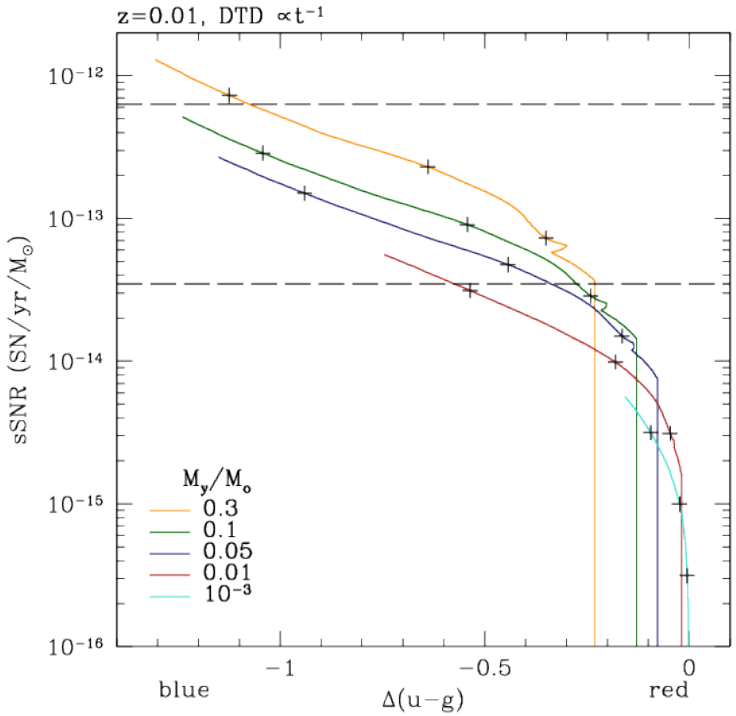

Figure 5.27: *Type Ia specific SNe rate as a function of colour difference* $(u-g)$ *for redshift* $z = 0.01$ *and DTD power* $x = -1$ *with a catastrophic cutoff at 2 Gyr.*

Theoretical

We repeat our analysis and calculate the specific SNR as a function of colour shift for various model parameters but with theoretical DTDs. Figure 5.28 shows the result using the theoretical DD DTD as discussed above, and figure 5.29 uses a SD DTD. In line with the DTD curve behaviour in figure 5.14, the DD DTD plot converges to a value over a magnitude greater than the observational DTD with a non-catastrophic cutoff (see e.g. figure 5.24), with the SD DTD convergence point two magnitudes lower. The rapid drop in the SD DTD at 1.4 Gyr is readily apparent as well; it occurs at different colour shifts depending on the mass ratio in consideration. Further, the SD plot starts at lesser colour shifts due to the period of zero SNe at early ages (see figures 5.13 and 5.14). At larger colour shifts, it is easier to distinguish between DD scenario models as they are further separated from one another. In terms of absolute rate values, the SD curves seem to lie more within the rate limits (horizontal lines) in part due to the SD DTD enhancement at early age. Note that the DD curves can be easily renormalized to better lie within the observational region, since the absolute theoretical rates are an underestimate.

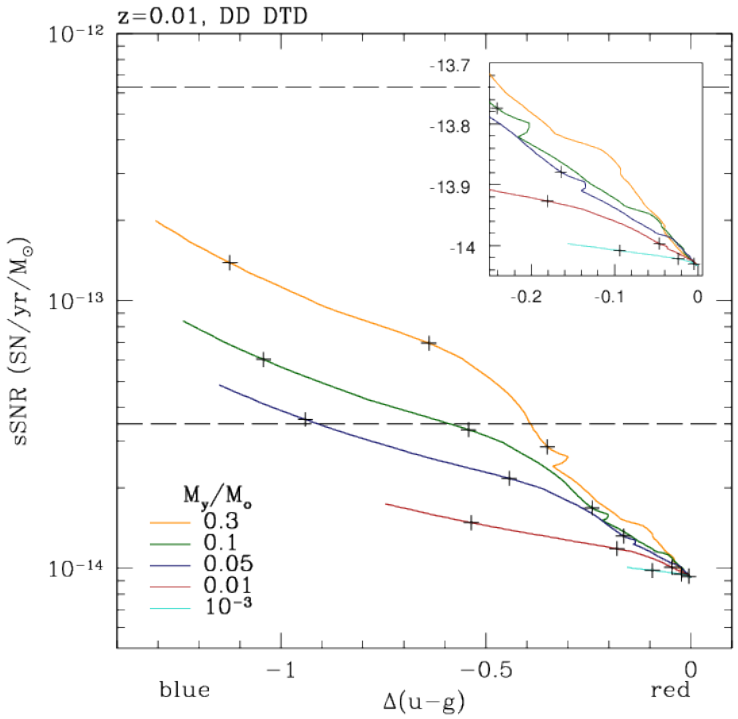

Figure 5.28: *Specific supernova rate as a function of $u-g$ colour shift for the theoretical DD DTD discussed in the text.*

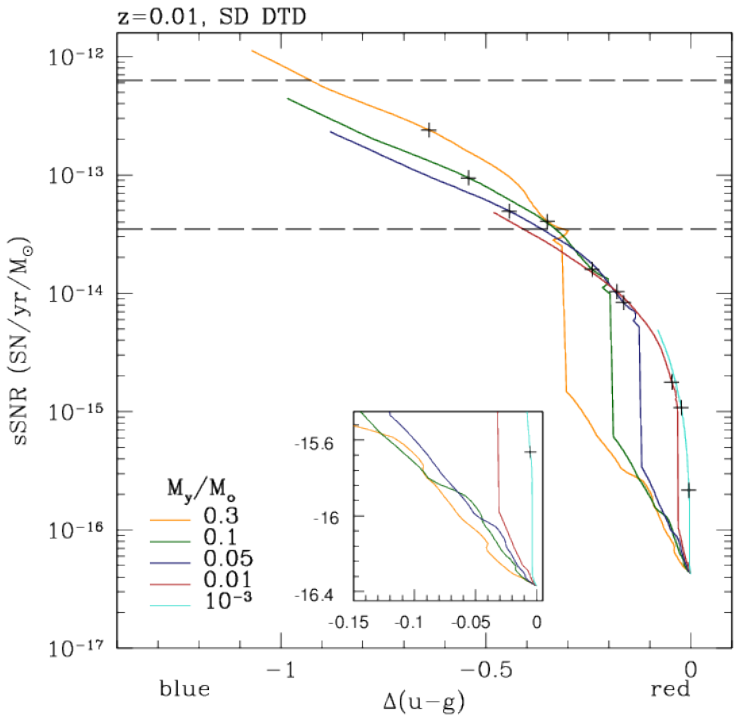

Figure 5.29: *Specific supernova rate as a function of $u-g$ colour shift for the theoretical SD DTD discussed in the text.*

Redshift

We also explore the effect of redshift on $u - g$ using a straight power-law DTD with $x = -1$ (see figures 5.30 to 5.33). At a redshift of 0.1 there is very little difference from a redshift of 0.01; in the former the curves are slightly more vertically separated for large colour shift, and more cluttered at small colour shift. As we increase the redshift to 0.3, the range in colour shift increases drastically and a steeper upward turn is apparent in the curves for the largest colour changes. At redshift 0.5, this steepening is even more pronounced and the plot spans a colour difference of nearly 3 (compared to 1.4 at $z = 0.01$). For lesser colour differences, as redshift rises the curves become more horizontal and less steep as they approach $u - g = 0$.

Further, the curves converge in a much neater fashion at redshifts of 0.3 and 0.5. The point of convergence itself changes with redshift as well, slowly increasing from the "A" value. This is likely due to the age of the underlying population which decreases with redshift; consequently the underlying rate is going to be higher as a result. For instance at $z = 0.5$ the underlying population has an age of 5 Gyr, half that at $z = 0.01$. For a DTD power $x = -1$, a 5 Gyr old population has twice the rate of a 10 Gyr old population, exactly the effect we are seeing.

We expect the observed stretching in colour range. As redshift increases, UV light from the young population shifts into the u band and thus the $u - g$ colour becomes even bluer. This is especially the case for the youngest of stellar populations as seen in the steepest part of the $z = 0.5$ plot.

Next we incorporate our models with data in attempt to draw some conclusions about the nature of type Ia SNe.

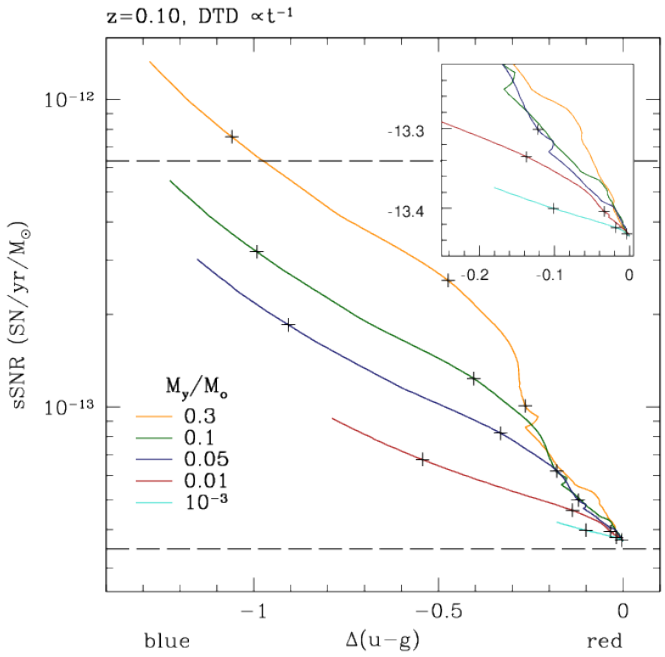

Figure 5.30: *Specific supernova rate as a function of $u-g$ colour shift for an observational straight power-law DTD at $z = 0.10$.*

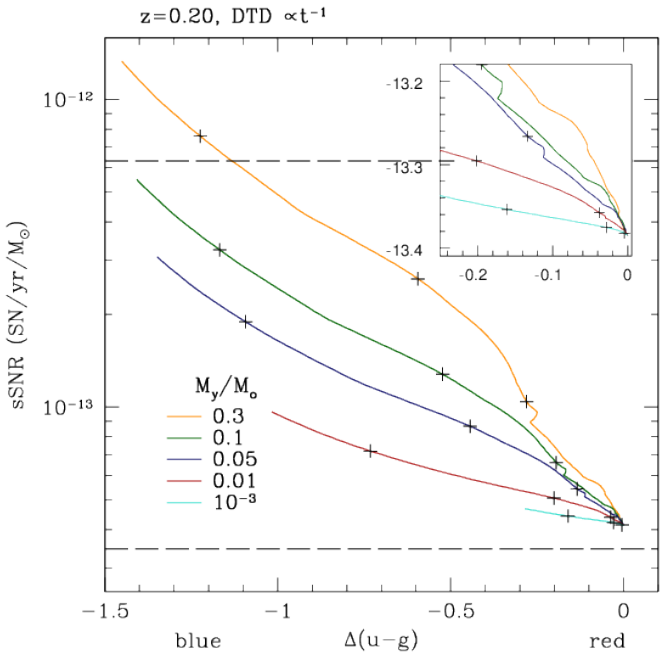

Figure 5.31: *Specific supernova rate as a function of $u-g$ colour shift for $z = 0.20$ with the same DTD as in the previous figure.*

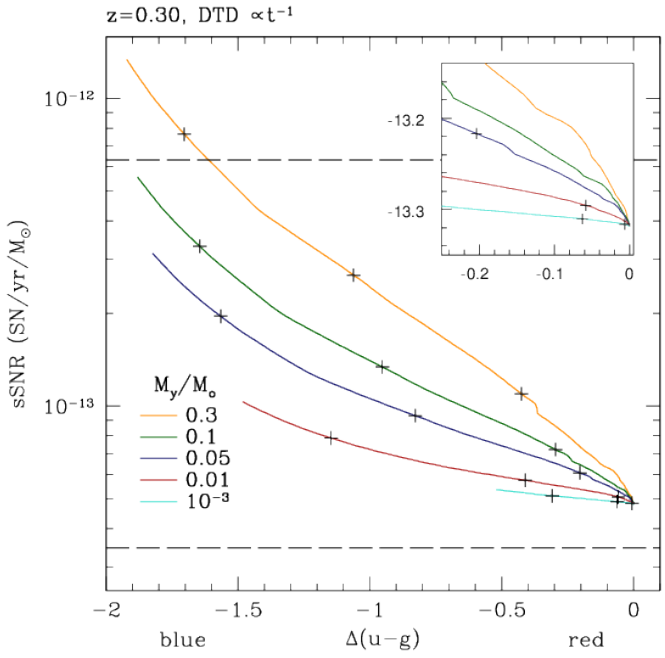

Figure 5.32: *Specific supernova rate as a function of $u-g$ colour shift for $z = 0.30$.*

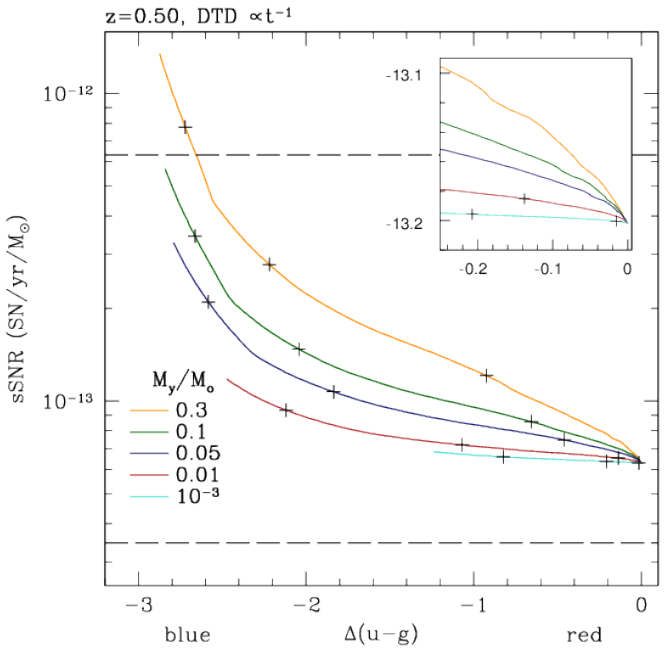

Figure 5.33: *Specific supernova rate as a function of $u-g$ colour shift for $z = 0.50$.*

5.7 Application to Observations

We now apply our models to the MENeaCS survey to determine the expected yield of supernova host colours based on the cluster sample that was observed.

5.7.1 MENeaCS Catalog

The MENeaCS catalog was used to examine all cluster members from each of 54 clusters included in the survey. Each cluster catalog includes a list of likely and possible cluster members; the former lie on or close to the red sequence (early-type galaxies) whereas the latter are bluer than the red sequence (late-type galaxies). The red sequence of each cluster is provided via a simple linear relation,

$$(g-r) = m \times r + (g-r)_o \tag{5.24}$$

in which $(g-r)$ is the colour of a galaxy on the red sequence, m the red sequence slope, r the apparent r-band magnitude and $(g-r)_o$ the zero-point of the relation. Relation (5.24) gives, for a specific cluster, the expected colour of a cluster member with a given r magnitude. As such, with knowledge of the r magnitude for an individual galaxy we can calculate its offset from the red sequence of the cluster it belongs to, specifically

$$\Delta(g-r) = (g-r)_{galaxy} - (g-r)_{cluster} \tag{5.25}$$

where $(g-r)_{cluster}$ is given by relation (5.24) and $(g-r)_{galaxy}$ is measured. Galaxies bluer than the red sequence will have $\Delta(g-r) < 0$, whereas on the red sequence $\Delta(g-r) \sim 0$. In this way we can construct a single diagram incorporating all cluster galaxies from the entire sample to display the red sequence offset number distribution. In order to avoid contamination from background/foreground galaxies, we impose a magnitude cut. Since the sample cluster redshifts varied from $0.05 \lesssim z \lesssim 0.15$ we account for redshift by selecting a constant r-band cutoff in absolute magnitude and varying in apparent magnitude in accordance with redshift. The constant cutoff was determined by calculating the absolute magnitude of an object with $m_r = 20$ at a redshift of $z = 0.1$, the median redshift of the sample. This yields an absolute magnitude cutoff of $M_r = -18.3$; we reject any fainter objects. We use the luminosity distance and correct the absolute magnitude cut using the distance modulus, finding the apparent magnitude for each cluster that corresponds to the absolute magnitude

cut. In this sense we select galaxies of the same intrinsic brightness regardless of redshift.

A plot of the colour offset versus the r-band magnitude for a small subset of MENeaCS cluster objects (figure 5.34) reveals the RS nicely; it is well defined as a band centered on zero colour shift. We can thus be confident in our assignment of cluster members to the RS.

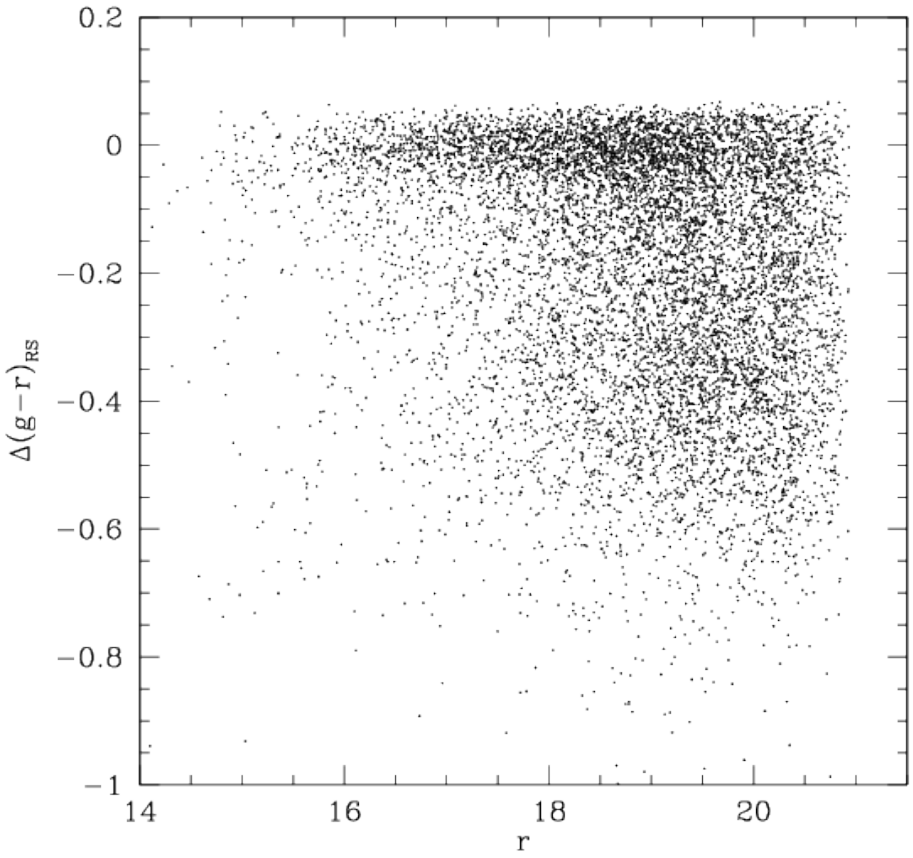

Figure 5.34: *Shift in $g-r$ colour from the red sequence vs. apparent r magnitude for a subset (9606) of MENeaCS galaxies selected at random. Note the prominent red sequence centered on $\Delta(g-r) \simeq 0$.*

The resulting RS colour offset distribution for all galaxies that make the cut is shown in figure 5.35. The red sequence is clearly apparent as the spread resembling a normal distribution with width of approximately $\Delta(g-r) \sim 0.15$ centered on zero. The number of galaxies then tapers off as bluer galaxies become more rare. There are no galaxies redder than the RS since these are rejected from cluster membership

consideration; no galaxies should be redder (i.e. older) than the red sequence.

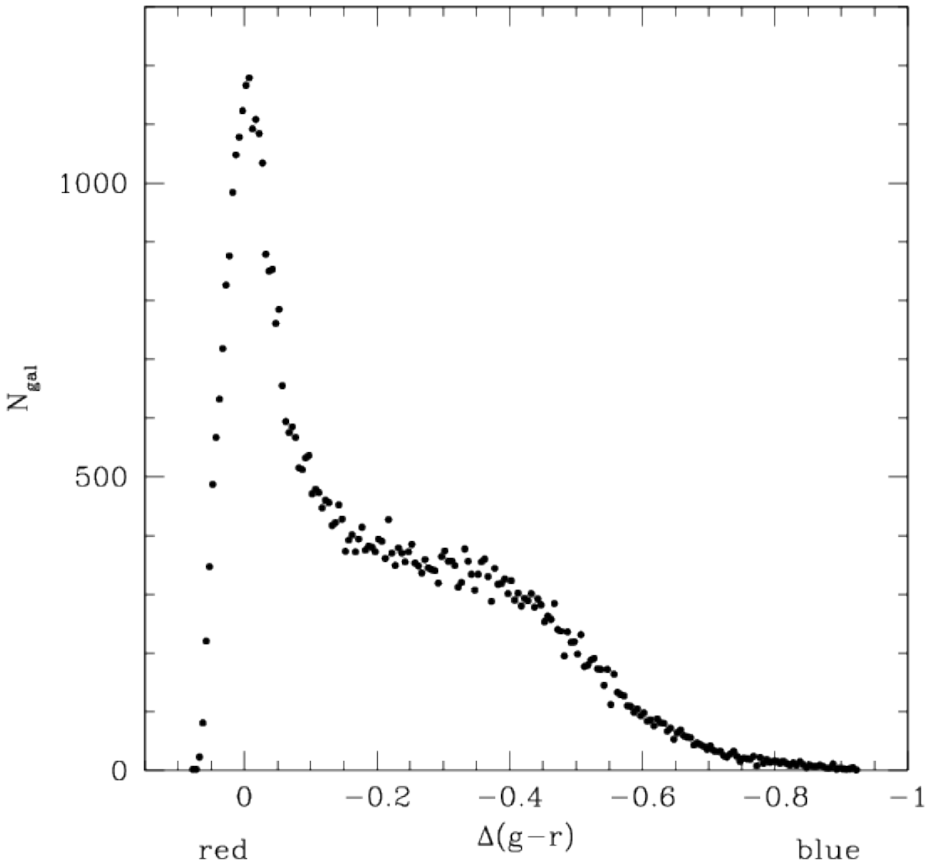

Figure 5.35: *Red sequence offset distribution for MENeaCS cluster members using a bin width of* $\Delta(g-r) = 0.005$*. In total 54 clusters are incorporated, and a magnitude cut of* $M_r < -18.3$ *was employed. The red sequence is centered on* $\Delta(g-r) = 0$*.*

5.7.2 Model Application

Now we apply our elliptical models to the MENeaCS data. In order to use our models some assumptions must be made. First we assume that galaxies which lie on the red sequence are composed of a single old population (the underlying population in our models). Any shift blueward of the red sequence is consequently due to the presence of a younger population in the galaxy. Therefore if we interpret the colour shift $\Delta(g-r)$ in our models as the shift away from the red sequence, we can use the colour shift as a proxy for the supernova rate. For the transformation from RS colour offset to

supernova rate we use figure 5.36 which features our models at the median redshift of the MENeaCS sample for a DTD with $x = -1$. Use of the $x = -1$ models is justified based on the convergence of each model to the appropriate base "A" rate.

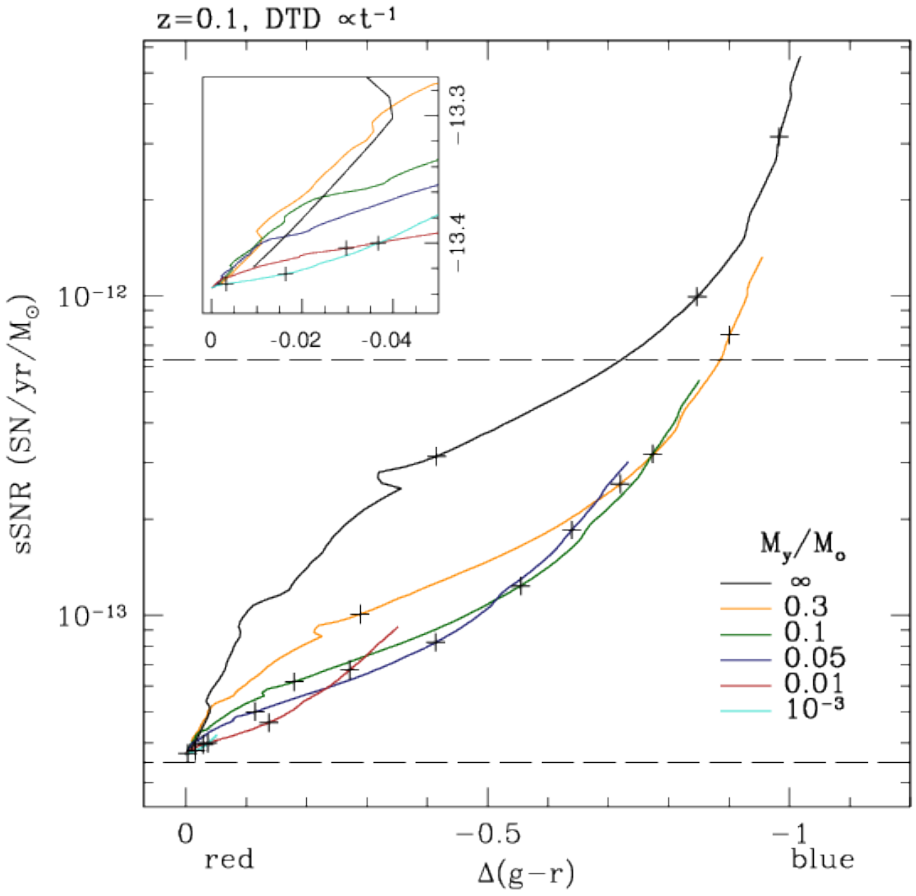

Figure 5.36: *Specific supernova rate as a function of colour shift for various models at redshift $z = 0.1$ with a straight power-law DTD. The black curve represents a pure burst (no underlying population) for comparison.*

First note that the full range in MENeaCS RS offsets in figure 5.35 ($0 < \Delta(g-r) \lesssim -1$) is nearly the same as the colour range spanned by the models in figure 5.36. Neglecting the black curve which is the extreme case of a pure starburst (no underlying population), the remaining models follow a fairly tight linear relation with slope $m \simeq -1$ and converge to nearly the same value at the RS end. We model this

correlation via the linear relation

$$\log(sSNR) = -\Delta(g-r) - 13.43. \tag{5.26}$$

Our goal is to make a plot analogous to figure 5.36 for the MENeaCS sample that describes the expected SN rate as a function of RS offset. Note we are interested in the *cumulative* supernova rate which represents the overall rate expected from the entire sample (and not the individual rate per galaxy as in our models). We employ the following method:

1. Convert colour bins to log(sSNR) bins using relation (5.26).

2. Account for the colour distribution by convolving the number of galaxies in each bin (from figure 5.35) with the bin sSNR to find the cumulative rate.

The result is shown in figure 5.37. The units of supernova rate are arbitrary (the values will be scaled by bin size) but we can still make relative comparisons between different colour shifts. Note how even though the red sequence sSNR is lower than that in bluer galaxies, the significant number of RS galaxies results in a cumulative rate that is at least 2 times greater than bluer galaxies. As the colour offset increases to $\Delta(g-r) < -0.5$, the RS rate dominates even more. Further we expect a near-symmetric distribution of supernovae in a small range about the RS, precisely what is observed in figure 5.2.

There is an additional correction to figure 5.37 that we must make, namely for the mass function of galaxies. The above calculation assumes all galaxies are the same mass but this is not the case; the MENeaCS galaxies span a range in luminosity (and therefore mass). More luminous galaxies are also more massive and will have a stronger contribution to the sSNR than less luminous galaxies. We correct for this by assuming mass is proportional to luminosity, $M \propto L$; equivalent to assuming a constant mass-to-light ratio.

We then adopt the following procedure:

1. Convert colour bins to log(sSNR) bins.

2. Calculate the r-band luminosity of each individual galaxy from its r magnitude using (2.2) and a reference absolute magnitude of $M_r = -18.3$ with a reference flux $f_o = 1$, again accounting for redshift in varying the apparent magnitude. The luminosity is a mass-weighting (w_{gal}) for each galaxy since $w_{gal} = f/f_o = M/M_o$ based on a constant M/L ratio.

3. Add up the weightings of all galaxies in each bin.

4. Multiply the total weighting in each bin by the bin SNR to determine the cumulative rate.

The outcome is shown in figure 5.38. There are several outliers on the blue end and some spread is introduced, but the general trend of figure 5.37 is maintained: we expect significantly more SNe from RS galaxies. How would implementation of a non-constant mass-to-light ratio affect figure 5.38? As we move in colour towards the blue cloud, M/L decreases since spiral galaxies have larger fractions of younger, more massive stars which exhibit significantly higher luminosities per unit mass (see relation (A.22)). By varying the mass-to-light ratio, the discrepancy between the expected rate of RS galaxies and blue cloud galaxies seen in figure 5.38 would become even more pronounced.

The near-Gaussian distribution about the RS is in agreement with the distribution of SN hosts in MENeaCS. For comparison we plot the smoothed, normalized colour distribution of MENeaCS hosts to emphasize the similarity in distribution shape (see figure 5.39). We also plot the host colour distribution alongside the expected distribution (figure 5.38) in figure 5.40. The latter was converted from a logarithmic to linear distribution and scaled such that the peak was $N = 4$. The host colour distribution has a very similar shape. Further, the RS is quite clearly defined, centered on $\Delta(g - r) = 0$. This is quite encouraging considering the small sample size (only 19 SN hosts).

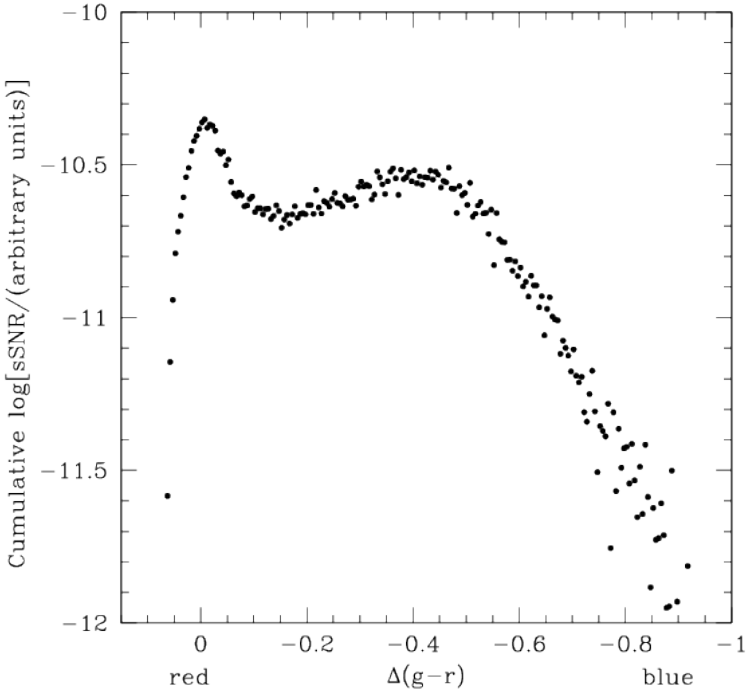

Figure 5.37: *Expected cumulative supernova rate as a function of RS* $(g-r)$ *offset for the MENeaCS sample. Note that the rate is merely relative and units on the vertical axis are arbitrary.*

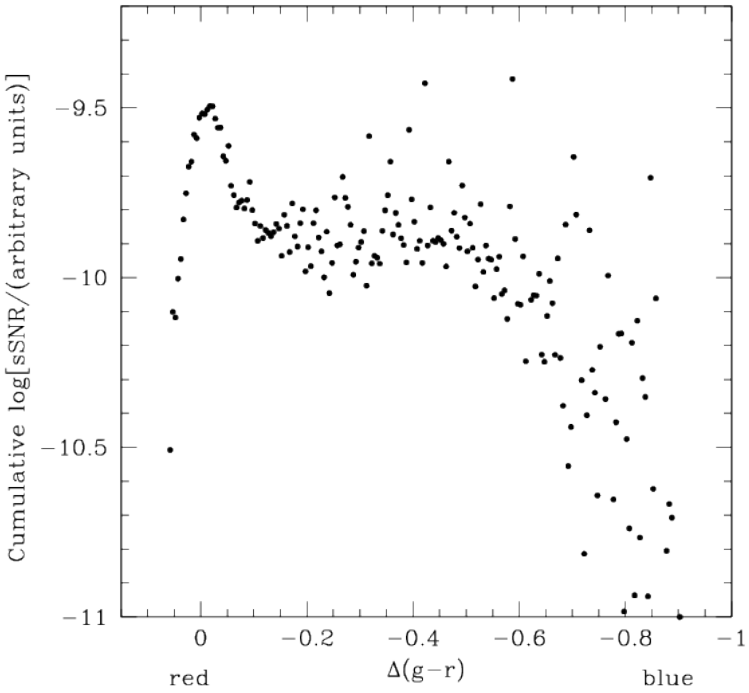

Figure 5.38: *Expected cumulative supernova rate as a function of RS* $(g-r)$ *offset for the MENeaCS sample corrected for galaxy mass.*

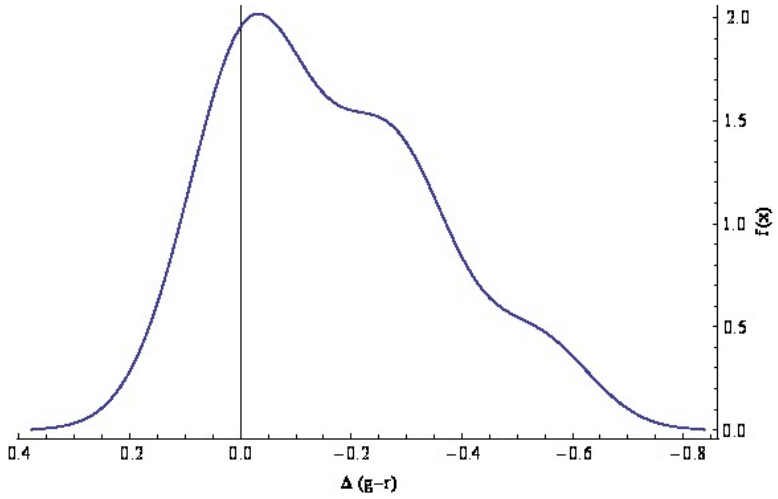

Figure 5.39: *Smoothed normalized colour distribution of MENeaCS host galaxies.*

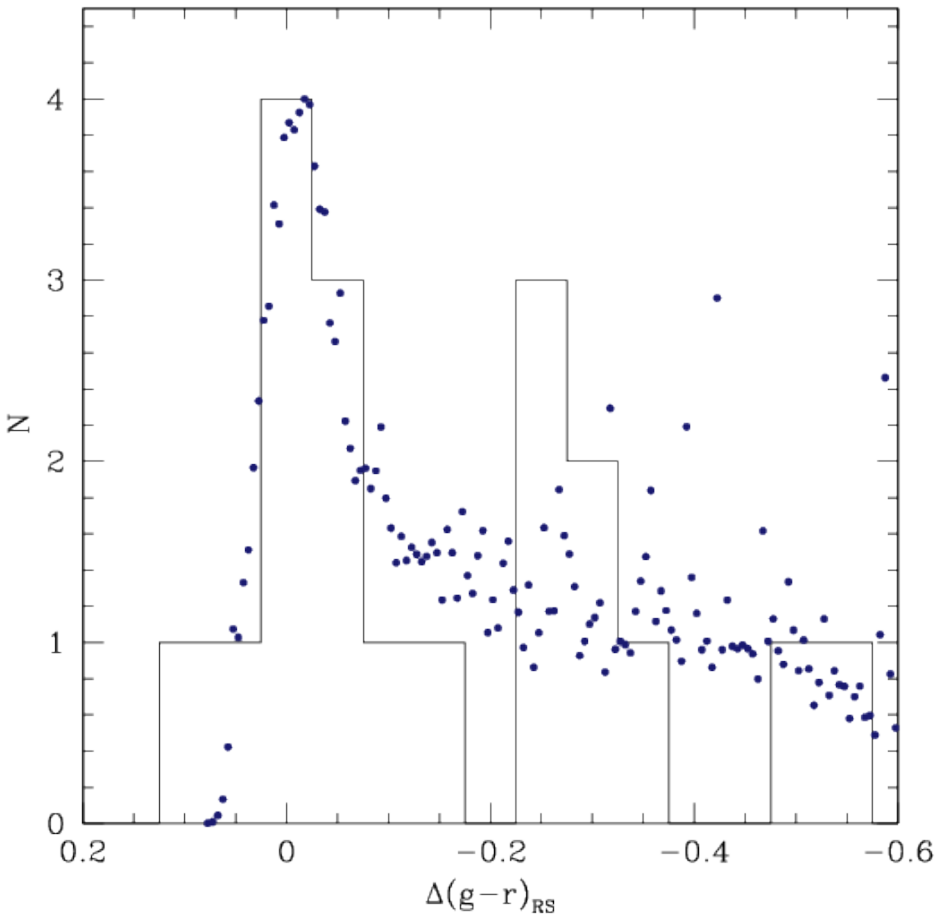

Figure 5.40: *Histogram colour distribution of MENeaCS host galaxies with bins of* $\Delta(g-r) = 0.05$ *plotted concurrently with the expected host distribution from models (blue points).*

We now consider the question of whether a cutoff exists in the DTD. It is plausible that a cutoff is present and that some small amount of frosting produces all type Ia SNe. Such a small amount of younger stars would have a negligible (i.e. non-detectable) effect on the colours of the host galaxy, therefore giving the illusion of a continuous DTD. Even though the SNe would be derived from the younger population, it would not appear so since the general assumption in such observations is that the age of the SN progenitors matches the mean age of the dominant stellar population. Our models rule out this possibility. Examining figure 5.24 reveals that galaxies with small colour shifts have significantly lessened SN rates by up to two orders of magnitude from the base "A" value. This cannot be adjusted by raising the normalization; any increase in normalization will shift the models so high that they will exceed the rate of the most powerful starbursting galaxies. Since we do not observe rates beyond this extreme level, it provides a constraint that must be satisfied. If there were a cutoff, tiny frostings would not be sufficient to produce the required number of SNe.

Since we observe the expected number of RS hosts relative to bluer hosts in MENeaCS data, the delay time distribution cannot have a cutoff starting at 1-2 Gyr; otherwise there would not be such an even clustering of SN hosts around the RS (neglecting the significantly bluer, clearly star-forming galaxies). We can rule out the hypothesis that type Ia SNe originate solely from a frosting of young stars; this would have manifest as a systematic shift of RS hosts to the blue end. These results argue for the double degenerate scenario as the dominant type Ia channel as opposed to the single degenerate model which should exhibit a cutoff.

In this chapter we explored the hypothesis that a large fraction of type Ia supernovae are derived from younger populations. We built models of elliptical galaxies by combining stellar population templates of different ages, and then determined the relation between supernova rate and colour shift for a variety of different model and observational parameters. We then applied our models to the MENeaCS dataset and found that the DTD is best represented by a continuous power-law with no cutoff, in favour of the double degenerate progenitor model.

Chapter 6

Conclusions

In this thesis we presented near-infrared CFHT observations of the ultraluminous infrared galaxy Arp 220. A monitoring program was carried out over the course of 13 months using the WIRCam instrument in attempt to detect supernovae and establish the supernova rate as well as the feasibility of a large-scale LIRG imaging survey. We were able to estimate the nuclear extinction in Arp 220 in agreement with prior estimates. We also presented models of elliptical galaxies consisting of a fixed underlying population and a tunable young component in order to expore the relation between galaxy red sequence colour offset and type Ia supernova rate. We then applied our models to the MENeaCS cluster supernova survey.

Our main results are summarized in the following:

- The WIRCam detector readout noise is $n_r = 7.28 \pm 0.15$ adu in agreement with the theoretical value of $n_r = 7.90 \pm 2.60$ adu. Its gain is found to be $g = 3.88 \pm 1.08$ e^-/adu, also in agreement with the expected value of $g = 3.80 \pm 0.20$ e^-/adu.

- No transients were apparent in Arp 220 from a visual search. PSF-matching and image subtraction revealed no supernovae in the galactic nuclear regions, though subtraction residuals prevent the detection of SNe in the innermost ~ 3 arcsec, in which we cannot rule out the presence of any SNe.

- Differential photometry using a system of reference stars revealed variations in nuclear flux over the course of the observing program. A strong peak was identified on the sixth epoch. Due to blending of the two nuclei in WIRCam data, we are unable to identify in which nucleus the peak is housed; from radio

observations the majority of SN and SN remnants are found in the western nucleus. This method is not sensitive to individual SNe in the nuclear regions of Arp 220.

- We used NICMOS data to subtract off the nuclear background and estimate the true magnitude of the brightening event. The peak resembles a point source with absolute K-magnitude $M_K = -22.19 \pm 0.16$, significantly more luminous than a typical core collapse SN.

- We estimated the nuclear extinction in Arp 220 using the extinction curves of Rieke & Lebofsky (1985) and Fitzpatrick & Massa (2009). We find a range of extinction (in magnitudes) at the 1-σ level of $2.01 \leq A_K \leq 3.40$ and $17.95 \leq A_V \leq 30.36$ in the optical, in agreement with several other estimates.

- We propose that the observed variations in nuclear brightness are due to AGN activity or the combination of light from multiple supernovae in the core of Arp 220, especially if the supernova rate is underestimated.

- When normalizing the delay-time distribution to the youngest starbursting galaxies, our elliptical models with a single DTD power $x = -1$ all lie within the range of observed type Ia rates and converge to the expected "A" rate. DTD power $x = -0.7$ overestimates the underlying rate while $x = -1.5$ is an underestimate.

- Young populations with mass fraction $M_y/M_o < 0.001$ have a negligible impact on both the supernova rate and colour of an old galaxy. In order to observe colour shifts from the red sequence the young population must comprise a more substantial portion of the total stellar galactic mass. This is in accordance with SED model fits using the frosting model which find typical mass fractions $M_y/M_o \sim 0.1$.

- The double degenerate theoretical DTD of Mennekens et al. (2010), while underestimating the SNR, closely resembles the shape of our straight $x = -1$ power-law DTD. In similar fashion the theoretical single degenerate DTD displays a sharp cutoff similar to our models with non-catastrophic cutoffs.

- With increasing redshift our models show a strong vertical steepening of the SNR with colour shift for the youngest of stellar populations, and a stretching

of the horizontal colour range as ultraviolet light begins to shift into the optical bands, enhancing colours toward the blue end.

- Analyzing cluster members from the MENeaCS survey, we estimate the cumulative supernova rate and find the expected RS host colour distribution to be nearly symmetric about the RS, in agreement with MENeaCS results. We conclude there is no cutoff in the delay time distribution, in favour of the double degenerate SN Ia scenario. Further we rule out the hypothesis that type Ia SNe in elliptical galaxies originate only from a small frosting of younger stars.

6.1 Where are the supernovae?

Is the non-detection of SNe in the circumnuclear regions of Arp 220 unexpected? The nearby extensively studied starburst galaxy M82 has a similarly concentrated starburst compared to that in Arp 220 (confined within several hundred parsecs in the core). In fact, Arp 220 is often envisaged as a "scaled up" version of the starburst activity in M82. To date however only a single supernova has been discovered in M82 at optical/near-IR wavelengths; all others have been first identified in the radio (Mattila et al., 2013). Thus it seems finding SNe in starburst galaxies, even those which are nearly next door, is no simple task.

Why has supernova detection been challenging in starburst galaxies, including LIRGs and ULIRGs? Both Mannucci et al. (2003) and Cresci et al. (2007) suggest a number of arguments to reconcile their SN underdetections. Perhaps the most obvious is that large extinctions, even in the near-IR, obscure most SNe. If the starburst is highly contained (e.g. in the central few hundred parsecs), image subtraction residuals - even from space-based or adaptive optics corrected observations - would prevent the detection of central SNe. Less likely candidates involve underluminous SNe or a differing IMF in starbursts relative to quiescent galaxies. Lastly, the far-IR luminosity may be dominated by AGN activity, in which case estimating the supernova rate from the FIR flux is no longer valid.

6.2 AGN in Arp 220

The flux variations discovered in Arp 220 from WIRCam measurements may owe their origins to an active galactic nucleus. If an AGN is present in Arp 220, its

observational signatures would be very difficult to detect in the optical/near-IR for the very same reasons that supernovae prove difficult to observe in this spectral region. Disentangling AGN from starburst activity at mid-far infrared wavelengths is also a challenge considering that both flux sources can yield a similar IR excess. However, methods exist using mid-IR emission line ratios and PAH line strengths (e.g. Genzel et al., 1998). If the AGN is emitting jets beamed towards Earth these may be revealed in both the radio and X-ray continua. Further, X-ray line emission may be expected such as the iron-alpha emission line (see Iwasawa et al., 2005). Thus a focus on radio and X-ray observations in Arp 220 should be emphasized in the future search for an AGN in this ULIRG.

6.3 Future of LIRG Observations

Our observations of Arp 220 have shed light into the practicality of a widespread LIRG/ULIRG study. In order to maximize the supernova yield a large number of galaxies should be observed with a long cadence, preferably galaxies which exhibit more widespread star formation than Arp 220. Due to the presence of nuclear image subtraction residuals, nearby LIRGs should take priority in order to reduce the physical region over which supernovae are undetectable. While ULIRGs may have greater supernova rates, they are generally more distant and their supernovae may avoid detection, thus there is no advantage to emphasizing ULIRGs over their less luminous LIRG cousins.

We have put together a catalog of 195 known LIRGs from the IRAS Revised Bright Galaxy Sample (Sanders et al., 2003) with redshifts extending out to $z = 0.07$. The sample itself contains 629 objects and is a full subset of the IRAS (Infrared Astronomical Satellite) sample, the first space-based observatory to survey the entire sky in the infrared. We select out LIRGs based on the criterion $L_{FIR} > 10^{11} M_{\odot}$. Our catalog contains 14 ULIRGs; the remaining galaxies are all classified as LIRGs. As suggested by Matilla & Meikle (2001), a sample of 45 galaxies surveyed on a 6 month cycle should yield a minimum of one SN per cycle. In order to better probe the central regions of LIRGs, lower redshift LIRGs are preferable to more distant galaxies. Furthermore, such an imaging survey seems better suited to a space-based telescope due to the resolution problems discussed in this thesis. For detecting nuclear SNe we recommend infrared spectroscopy for identifying telltale SN spectral features. We made spectroscopic observations of Arp 220 in July 2013 using the OH Suppressing

Infra-Red Imaging Spectrograph (OSIRIS) on Keck; results are still pending. The work done in this thesis sheds new light on how to approach the problem of the missing supernovae in luminous infrared galaxies in the future.

6.4 Future of type Ia SNe in RS Observations

While we have applied our models to a single survey, MENeaCS features only 19 hosted SN Ia. In order to further test our conclusions regarding the continuity of the DTD and progenitor models, it would be of benefit to apply the same analysis to other large scale SN surveys. While we have seen evidence for this behaviour at relatively low redshift ($z \simeq 0.1$), it would also be useful to look at higher redshift hosts. Further, the SN sample size in MENeaCS is subject to small number statistics; a larger sample would be very useful. We have thus far only considered optical filters in our models; the inclusion of UV filters would increase the wavelength range at which such an analysis can be applied. The ultraviolet is very sensitive to young populations and would be quite robust for determining the presence of frostings of younger stars. Our models provide an alternative way to test probable type Ia progenitor scenarios. Given the pertinence of such supernovae in the measurement of cosmological parameters, improving our understanding of such energetic events helps to better shape our conception of the beautiful Universe we live in.

Appendix A

Appendix Additional Information

A.1 Arp 220 Angular Scale

In order to discuss observations of Arp 220, it is important to establish the relation between the angular scale on the sky and the corresponding physical linear scale at the distance of Arp 220. A simple way to do this is to ask what angular size on the sky corresponds to 1 kpc of physical distance at Arp 220. Consider figure A.1 in which Earth is located at vertex P, Arp 220 at O and the length $O = 1$ kpc. Since

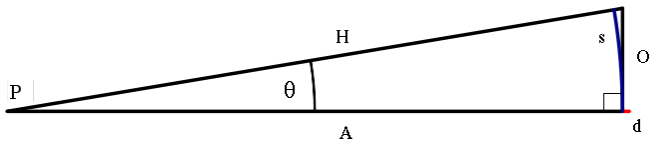

Figure A.1: *Geometry of observing a distant extended source in the sky such as a galaxy. The observer is located at point P and the galaxy at a distance $A \simeq H$. A segment of the galaxy is denoted by side O.*

the angle subtended by this region of the galaxy is so small ($\theta << 1°$), the lengths A and H are approximately equal, $A \simeq H = 77$ Mpc. Consequently the arc-length approximation to the right triangle can be used, specifically

$$s = r\theta \tag{A.1}$$

where $r = A = H$. Solving for the angle yields $\theta = 2.68''$/kpc or 373 pc/$''$. Thus one second of arc subtends 373 parsecs of Arp 220.

A.2 Point Spread Functions

A point spread function (PSF) describes how the light of a point source is distributed two-dimensionally in the focal plane of a telescope. A star observed on the sky is essentially located, optically speaking, at infinity. As such it is a perfect point source, and its light would ideally impinge on only a single detector pixel. In reality however, two effects serve to spread out the light from a point source: telescope optics and Earth's atmosphere. The former results from the use of a circular aperture (mirror or lens) and the presence of imperfect optics; the corresponding effect on the PSF is constant in time but varies with position in the focal plane. The effect of the atmosphere on the PSF changes in both space and time as discussed previously. A perfect optical system built with circular elements would exhibit what is referred to as an Airy Disk PSF (see figure A.2).

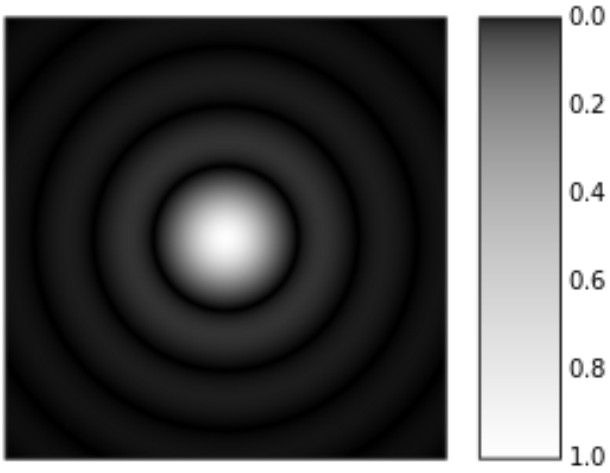

Figure A.2: *Airy disk profile weighted by intensity in grayscale.*

When the atmosphere is taken into account the PSF is altered and takes on a different intensity distribution. A commonly used fitting profile is the Moffat profile (Moffat, 1969). It describes intensity (I) as a function of radius (r) on the focal plane via

$$I(r) = I_o \left[1 + \left(\frac{r}{\alpha}\right)^2\right]^{-\beta} \tag{A.2}$$

in which I_o is the central intensity, α a scale factor and β an exponent which determines the overall PSF shape.

A.2.1 PSF Matching

Before performing image subtraction, it helps to match the PSFs between subsequent imaging epochs. Why is this necessary? While the telescope instrumentation does not change between observing nights, atmospheric conditions do; the atmosphere is highly unstable and will alter the PSF. If the PSFs are not matched when two images are subtracted, residuals may be seen that originate due to differences in the point spread profile. These may be mistaken for brightening events; to minimize the chance of false events we need to remove such residuals from consideration. An example of how mismatched PSFs can lead to residuals is given in figure A.3.

Figure A.3: *When a point source with different PSFs on subsequent epochs is subtracted, an instrumental residual is formed due to the difference in point spread profile alone.*

How are point-spread functions matched? It is possible to improve a poor PSF by sacrificing signal-to-noise (increasing the amount of noise relative to signal). In contrast we can also degrade a good quality PSF to match one of lesser quality, which is the approach we take here. We characterize PSFs typically using the full-width at half maximum (FWHM) which specifies the length of the intensity profile between the points at which it reaches half the central intensity (see figure A.4 for clarification). Mathematically speaking, if the PSF intensity is represented by $I = f(r)$, the central intensity is I_o and it reaches half this value at $I_o/2 = f(r_2)$ and $I_o/2 = f(r_1)$ then the full-width half maximum is:

$$FWHM = r_2 - r_1. \tag{A.3}$$

The smaller the FWHM, the better the seeing in the image as a star will appear more point-like in nature.

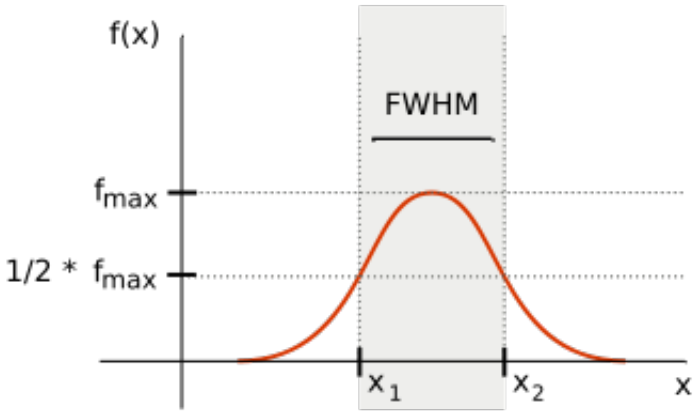

Figure A.4: *The full-width at half maximum is the distance between the two points of a function at which it reaches half the central maximum.*

A.3 Convolution Theory

Definition 1. *The convolution of two functions $f(t)$ and $g(t)$ is given by the integral transform:*

$$(f * g)(t) \equiv \int_{-\infty}^{\infty} f(\tau)g(t-\tau)d\tau. \tag{A.4}$$

A convolution expresses the amount of overlap of one function ($g(t)$ in this instance) as it is shifted over another $f(t)$. Both functions are represented by a dummy variable τ, $g(t)$ is reflected and then translated along the τ axis, and the integral of the product of the two functions is calculated at each point of intersection. Convolutions have a variety of applications ranging from probability to electrical engineering, and prove quite useful in astronomical image processing.

Let A represent an observed image and I a reference image with poorer seeing than A. There will exist some convolution kernel K such that its convolution with the reference approximates the observed image: $\tilde{A} = K * I$ where $\tilde{A}$ is the estimate of A but with the point-spread function of I. If we can find the kernel K, we can then transform A into $\tilde{A}$, essentially matching the PSF of our image of interest to the reference.

A.4 Chi-square theory

The chi-square statistic has many uses in and beyond astronomy. For a thorough derivation see Bevington (1969).

Definition 2. *The value of chi-square is equal to the square of the difference between data* (y) *and theory* $(y(x))$ *divided by the standard deviation in the measurements* (σ)*, summed over all data points* (i)*:*

$$\chi^2 \equiv \sum_i \left[\frac{y_i - y(x_i)}{\sigma_i} \right]^2 . \tag{A.5}$$

The chi-square statistic is most frequently used as a measure of the goodness of fit of a model to a set of data. We can also define the reduced chi-square:

$$\chi^2_\nu = \frac{\chi^2}{\nu} \tag{A.6}$$

in which ν is the number of degrees of freedom, equal to the number of data points minus the number of distribution parameters determined from the data. The reduced chi-square statistic is useful in that it allows a common basis of comparison for data sets of differing sizes. If the model is a good approximation to the data, the difference between the two should be roughly the same as the standard deviation, thus for each data point

$$\begin{aligned} \chi^2_i &\simeq 1 \\ \chi^2 &= \nu\chi^2_i = \nu \\ \chi^2_\nu &= 1. \end{aligned} \tag{A.7}$$

Consequently $\chi^2_\nu \approx 1$ implies a good fit between the model and data. A poor fit will have $\chi^2_\nu > 1$. Note that $\chi^2_\nu < 1$ does not necessarily imply an improvement of fit, but may arise due to experimental fluctuations.

How do we quantify the goodness of a fit based on values of χ^2? We require the chi-square probability distribution function.

Definition 3. *The chi-square probability density function, also known as the chi-*

square distribution, for ν degrees of freedom is given by:

$$P_x(\chi^2, \nu) = \frac{(\chi^2)^{\frac{1}{2}(\nu-2)} e^{\chi^2/2}}{2^{\nu/2}\Gamma(\nu/2)}. \tag{A.8}$$

Note that (A.8) features the gamma function, defined as

$$\Gamma(n) = \begin{cases} (n-1)! & n = 1, 2, 3, ... \\ (n-1)(n-2)\cdots(3/2)(\sqrt{\pi}/2) & n = 1/2, 3/2, 5/2, ... \end{cases} \tag{A.9}$$

The chi-square probability function gives the distribution of the values of chi-square that would be obtained from a number of random samples approaching infinity. What we are ultimately interested in is the probability that a random set of N data points will yield a value of chi-square greater than or equal to the measured value. This is done by integrating the chi-square distribution:

$$P_\chi(\chi^2, \nu) = \int_{\chi^2}^{\infty} P_x(x^2) dx. \tag{A.10}$$

If the model is a good approximation to the data, then $P_\chi \simeq 0.5$ and there is a roughly 50% probability of finding a value of chi-square higher than that determined; if the match is poor, the probability decreases and $P_\chi << 0.5$. Thus a lower probability corresponds to a lower likelihood of exceeding the measured value of chi-square by chance alone, establishing a greater significance to the result. Next we quantify the statistical significance of the light curves using a chi-square approach.

A.5 DTD Power Law Derivation

It is a generic feature that delay time distributions are described in terms of power laws. Here we derive the expected form of the DTD for two cases, the double degenerate scenario (e.g. Maoz et al., 2010) and one which is dominated by the formation rate of white dwarfs (Pritchet et al., 2008).

A.5.1 Double Degenerate

In the double degenerate model the dynamics of the progenitor binary system are governed primarily by gravitational wave radiation resulting in the loss of energy and

angular momentum from the system. In this situation the time until a merger occurs (t) is dependent on the binary separation (a),

$$t \propto a^4. \tag{A.11}$$

The distribution of binary separations, based on observations, is best represented by a power law as well:

$$\frac{dN}{da} \propto a^{\epsilon}. \tag{A.12}$$

We can then determine the rate of WD merger events, specifically

$$\frac{dN}{dt} = \frac{dN}{da}\frac{da}{dt} \tag{A.13}$$

resulting in

$$\propto t^{\frac{\epsilon-3}{4}}. \tag{A.14}$$

The observed distribution of non-interacting binaries is well described by a power $\epsilon \approx -1$; inserting into equation (A.14) yields $dN/dt \propto -1$.

A.5.2 WD Formation Rate

If the duration between WD formation and type Ia explosion is short relative to the WD formation time, the latter is the rate determining step governing type Ia events. We can derive the expected rate under this presumption by starting with the main sequence stellar lifetime as a function of mass,

$$t \propto M^{\alpha}. \tag{A.15}$$

Further consider the initial mass function which is also well-described by a power law,

$$\frac{dN}{dM} \propto M^{\lambda}. \tag{A.16}$$

The rate of WD formation (and correspondingly the type Ia SNR) is then given by

$$\frac{dN}{dt} = \frac{dN}{dM}\frac{dM}{dt} \tag{A.17}$$

resulting in

$$\frac{dN}{dt} \propto t^{\frac{1+\lambda-\alpha}{\alpha}}. \tag{A.18}$$

With $\alpha = -2.5$ (see A.6) and a Salpeter IMF ($\lambda = -2.35$) we find $dN/dt \propto t^{-0.46}$, very close to a power index of $-1/2$.

A.6 Stellar Lifetimes

Here we derive the relation between the main sequence lifetime of a star and its mass. To determine the time required for a star to burn through its supply of hydrogen, we start by rearranging the definition of luminosity (L):

$$t = \frac{E}{L} \tag{A.19}$$

in order to estimate the main-sequence lifetime (t) in terms of the total energy (E). Since the energy production of a star is dominated by nuclear reactions, the total energy budget available to a star is given by

$$E = fMc^2 \tag{A.20}$$

in which M is the mass of the star, c the speed of light and f the efficiency with which the star converts mass to energy. Inserting this into (A.19) yields

$$t \propto \frac{M}{L}, \tag{A.21}$$

the result that the lifetime of a star is proportional to its mass-to-light ratio. For stars between roughly $0.1M_\odot$ and $50M_\odot$, the following mass-luminosity relationship is found empirically:

$$L \propto M^{3.5}. \tag{A.22}$$

Applying this relationship to (A.21) gives the proportionality between lifetime and mass, specifically

$$t \propto M^{-2.5}. \tag{A.23}$$

Bibliography

Anderson, J. P., Habergham, S. M., & James, P. A. 2011, MNRAS, 416, 567

Arzoumanian, Z., Holmberg, J. & Norman, B. 2005, Journal of Applied Ecology, 42, 999

Barrientos, L.F., Schade, D. & Lopez-Cruz, O. 1996, ApJ, 460, 89

Batejat, F., Conway, J.E., Hurley, R., Parra, R., Diamond, P.J., Lonsdale, C.J. & Lonsdale, C.J. 2011, ApJ, 740, 95B

Batejat, F., Conway, J. E., Rushton, A., et al. 2012, A&A, 542, L24

Bevington, P.R. 1969, Data Reduction and Error Analysis for the Physical Sciences (New York: McGraw-Hill)

Bregman, J.D., Temi, P. & Rank, D. 2000, A&A, 355, 525

Buzzoni, A. 2002, A.J., 123, 1188

Cappellaro, E., Evans, R., & Turatto, M. 1999, A&A, 351, 459

Chevalier, R.A. 1982, ApJ, 259, 302

Chornock, R., Berger, E., Rest, A., et al. 2013, ApJ, 767, 162

Clements, D. L., McDowell, J. C., Shaked, S., et al. 2002, ApJ, 581, 974

Conley, A., Sullivan, M., Hsiao, E. Y., et al. 2008, ApJ, 681, 482

Cresci, G., Mannucci, F., Della Valle, M. & Maiolino, R. 2007 A&A 462, 927

Dabringhausen, J., Kroupa, P., Pflamm-Altenburg, J., & Mieske, S. 2012, ApJ, 747, 72

Della Valle, M., & Livio, M. 1994, A&A, 287, 403

Deupree, R. G., & Wallace, R. K. 1987, ApJ, 317, 724

Devereux, N.A., & Young, J.S. 1990, ApJ, 350, L25

Diehl, R., Halloin, H., Kretschmer, K., et al. 2006, Nature, 439, 45

Downes, D., & Eckart, A. 2007, A&A, 468, L57

Doyon, R., Wells, M., Wright, G. S., et al. 1994, ApJL, 437, L23

Engel, H., Davies, R. I., Genzel, R., et al. 2011, ApJ, 729, 58

Farrah, D., Serjeant, S., Efstathiou, A., Rowan-Robinson, M., & Verma, A. 2002, MNRAS, 335, 1163

Fioc, M., & Rocca-Volmerange, B. 1997, A&A, 326, 950

Fitzpatrick, E.L. & Massa, D. 2009, ApJ, 699, 1209

Fraser, W. C., Kavelaars, J. J., Holman, M. J., et al. 2008, Icarus, 195, 827

Gao, Y., & Pritchet, C. 2013, A.J., 145, 83

Gebhardt, K., Faber, S. M., Koo, D. C., et al. 2003, ApJ, 597, 239

Genzel, R. et al. 1998, ApJ, 498, 579

Genzel, R., Tacconi, L. J., Rigopoulou, D., Lutz, D., & Tecza, M. 2001, ApJ, 563, 527

Glass, I.S. 1999, Handbook of Infrared Astronomy (Cambridge: Cambridge University Press)

Graham, M. L., Sand, D. J., Bildfell, C. J., et al. 2012, ApJ, 753, 68

Greggio, L. 2005, A&A, 441, 1055

Grossan, B., Spillar, E., Tripp, R., et al. 1999, A.J., 118, 705

Groth, E.J. 1986, A.J., 91, 1244

Hachisu, I., Kato, M., & Nomoto, K. 2008, ApJL, 683, L127

Heger, A., Fryer, C. L., Woosley, S. E., Langer, N., & Hartmann, D. H. 2003, ApJ, 591, 288

Hillebrandt, W., & Niemeyer, J. C. 2000, ARA&A, 38, 191

Hillebrandt, W., Kromer, M., Röpke, F. K., & Ruiter, A. J. 2013, Frontiers of Physics, 8, 116

Hubble, E.P. 1936, The Realm of the Nebulae (New Haven: Yale Univ. Press)

Iben, Jr., I., & Tutukov, A.V. 1984, ApJS, 54, 335

Irwin, J.A. 2008, Astrophysics: Decoding the Cosmos (West Sussex: Wiley)

Iwasawa, K., Sanders, D. B., Evans, A. S., et al. 2005, MNRAS, 357, 565

Jack, D., Hauschildt, P. H., & Baron, E. 2012, A&A, 538, A132

Kelson, D.D., Illingworth, G.D., Franx, M. & van Dokkum, P.G. 2001, ApJ, 552, L17

Kodama, T., Yamada, T., Akiyama, M., Aoki, K., Doi, M. et al 2004, MNRAS, 350, 1005

Kormendy, J. & Sanders, D.B. 1992, ApJ, 390, L93

Le Borgne, D., & Rocca-Volmerange, B. 2002, A&A, 386, 446

Li, W., Leaman, J., Chornock, R., et al. 2011, MNRAS, 412, 1441

Liebert, J., Bergeron, P., Eisenstein, D., et al. 2004, ApJL, 606, L147

Loewenstein, M. 2006, ApJ, 648, 230

Lonsdale, C.J., Diamond, P.J., Thrall, H., Smith, H.E. & Lonsdale, C.J. 2006, ApJ, 647, 185

Lonsdale, C. J., Farrah, D., & Smith, H. E. 2006, Astrophysics Update 2, 285

Madau, P., Della Valle, M. & Panagia, N. 1998, MNRAS, 297, L17

Mannucci, F., Maiolino, R., Cresci, G., Della Valle, M., Vanzi, L., Ghinassi, F., Ivanov, V.D., Nagar, N.M. & Alonso-Herrero, A. 2002 A&A, 401, 519

Maiolino, R., Della Valle, M., Vanzi, L., & Mannucci, F. 2001, IAUC, 7661, 2

Maiolino, R., Vanzi, L., Mannucci, F., et al. 2002, A&A, 389, 84

Maoz, D., Sharon, K., & Gal-Yam, A. 2010, ApJ, 722, 1879

Matilla, S. & Meikle, W.P.S. 2001, MNRAS, 327, 350

Mattila, S., Meikle, W. P. S., & Greimel, R. 2004, NAR, 48, 595

Mattila, S., Väisänen, P., Farrah, D., et al. 2007, ApJl, 659, L9

Mattila, S., Fraser, M., Smartt, S. J., et al. 2013, MNRAS, 431, 2050

Mennekens, N., Vanbeveren, D., De Greve, J. P., & De Donder, E. 2010, A&A, 515, A89

Moffat, A. F. J. 1969, A&A, 3, 455

Nelemans, G., Yungelson, L.R., Portegies-Zwart, S.F., & Verbunt, F. 2001, A&A, 365, 491

Nomoto, K. 1982, ApJ, 253, 798

Norris, R.P. 1988, MNRAS, 230, 345

Parra, R., Conway, J. E., Diamond, P. J., et al. 2007, ApJ, 659, 314

Perlmutter, S., Aldering, G., Goldhaber, G., et al. 1999, ApJ, 517, 565

Pritchet, C. J., Howell, D. A., & Sullivan, M. 2008, ApJL, 683, L25

Ptak, A., Heckman, T., Levenson, N. A., Weaver, K., & Strickland, D. 2003, ApJ, 592, 782

Puget, P., Stadler, E., Doyon, R., et al. 2004, SPIE, 5492, 978

Rakos, K.D. & Schombert, J.M. 1995, ApJ, 439, 47

Rana, N.C. & Basu, S. 1992, A&A, 265, 499

Renzini, A. 2006, ARA&A, 44, 141

Richmond, M. W., Filippenko, A. V., & Galisky, J. 1998, PASP, 110, 553

Rieke, G.H. & Lebofsky, M.J. 1985, ApJ, 288, 618

Riess, A. G., Filippenko, A. V., Challis, P., et al. 1998, A.J., 116, 1009

Robitaille, T. P., & Whitney, B. A. 2010, ApJL, 710, L11

Röpke, F. K., & Hillebrandt, W. 2004, A&A, 420, L1

Rovilos, E., Diamond, P. J., Lonsdale, C. J., Lonsdale, C. J., & Smith, H. E. 2003, MNRAS, 342, 373

Salim, S., & Rich, R.M. 2010, ApJL, 714, L290

Salvaterra, R., Ferrara, A., & Schneider, R. 2004, NewA, 10, 113

Sand, D.J., Graham, M.L., Bildfell, C., et al. 2012, ApJ, 746, 163

Sanders, D. B., Mazzarella, J. M., Kim, D.-C., Surace, J. A., & Soifer, B. T. 2003, A.J., 126, 1607

Sanders, D.B. & Mirabel, I.F. 1996, ARA&A, 34, 749

Scannapieco, E., & Bildsten, L. 2005, ApJL, 629, L85

Schiavon, R. P. 2007, ApJS, 171, 146

Scoville, N.Z., Evans, A.S., Dinshaw, N., Thomson, R., Rieke, M., Schneider, G., Low, F.J., Hines, D., Stobie, B., Becklin, E. & Epps, H. 1998, ApjL, 492, L107

Smith, H.E., Lonsdale, C.J., Lonsdale, C.J. & Diamond, P.J. 1998, ApJ, 493, L17

Soifer, B.T., Neugebauer, G., Matthews, K., Becklin, E.E., Ressler, M., Werner, M.W., Weinberger, A.J. & Egami, E. 1999, ApJ, 513, 207

Soto, K. T., & Martin, C. L. 2010, ApJ, 716, 332

Stanford, S.A., Eisenhardt, P.R. & Dickinson, M. 1998, ApJ 492, 461

Sullivan, M., Conley, A., Howell, D. A., et al. 2010, MNRAS, 406, 782

Sullivan, M., Le Borgne, D., Pritchet, C. J., et al. 2006, ApJ, 648, 868

Svensmark, H. 2012, MNRAS, 423, 1234

Thomas, D., Maraston, C., Bender, R., & Mendez de Oliveira, C. 200, ApJ, 621, 673

Thompson, R. I. 1994, SPIE, 2198, 1202

Tokunaga, A.T. 2000, Allen's Astrophysical Quantities (Springer-Verlag: New York)

Totani, T., Morokuma, T., Oda, T., Doi, M., & Yasuda, N. 2008, PASJ, 60, 1327

Trager, S. C., Faber, S. M., Worthey, G., & González, J. J. 2000, A.J., 120, 165

Tsujimoto, T., Yoshii, Y., Nomoto, K., Matteucci, F., Thieleman, F. & Hashimoto, M. 1997, ApJ, 483, 228

Tutukov, A.V., & Yungelson, L.R. 1994, MNRAS, 268, 871

van Buren, D., Jarrett, T., Tereby, S., et al. 1994, IAUC, 5960, 2

van Buren, D., & Norman, C. A. 1989, ApJl, 336, L67

van Dokkum, P. G. 2008, ApJ, 674, 29

Webbink, R.F. 1984, ApJ, 277, 355

Whelan, J., & Iben, Jr., I. 1973, ApJ, 186, 1007

Wilson, C. D., Harris, W. E., Longden, R., & Scoville, N. Z. 2006, ApJ, 641, 763

Wood-Vasey, W. M., Friedman, A. S., Bloom, J. S., et al. 2008, ApJ, 689, 37

Woosley, S., & Janka, T. 2005, Nature Physics, 1, 147

Worthey, G. 1994, ApJS, 95, 107

Yi, S.K., Yoon, S.J., Kaviraj, S., et al. 2005, ApJLl, 619, L111

Yoon, J., Peterson, D. M., Kurucz, R. L., & Zagarello, R. J. 2010, ApJ, 708, 71

Young, L. M., Bendo, G. J., & Lucero, D. M. 2009, A.J., 137, 3053

Zhu, G., Blanton, M. R., & Moustakas, J. 2010, ApJ, 722, 491